

PREFACE

This report constitutes the final report on Air Force Contract F08635-74-C-0123. The research was performed by personnel of the Department of Aerospace Engineering, The University of Michigan, Ann Arbor, Michigan, under the direction of Professor J.A. Nicholls. The contract was with the Air Force Armament Laboratory, Armament Development and Test Center, Eglin Air Force Base, Florida. Dr. J.C. Foster, Jr., (DLJI) and, later, Lt. R.S. Fry, served as Program Manager for the Armament Laboratory. This effort was conducted during the period from January 1976 to May 1976.

This technical report has been reviewed and is approved for publication.

FOR THE COMMANDER

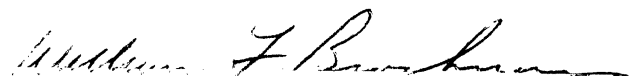

WILLIAM F. BROCKMAN, Colonel, USAF
Chief, Munitions Division

TABLE OF CONTENTS

Section	Title	Page
I	INTRODUCTION	1
II	RESEARCH RESULTS	5
	A. Derivation of the Approximate Governing Equations Describing the Induction Zone Structure Behind a Nonsteady Shock Wave in a Reacting Medium.	5
	Introduction	5
	Basic Equations	6
	Transformation to Inner Variables	15
	Results and Discussion	27
	B. Performance Characteristics of the Chamber	29
	C. Wave Front Shape	35
	Experimental Results and Discussion	38
	D. Propagation of Detonation Through a Non-Uniform Heterogeneous Mixture	65
	REFERENCES	83
Appendix		
A	COORDINATE TRANSFORMATION	85
B	CALCULATION OF $\frac{\dot{L}_c}{R_s}$	88
C	CALCULATION OF $\partial \epsilon / \partial \tau$ AND $\partial \epsilon / \partial \eta$	90

LIST OF FIGURES

Figure	Title	Page
1	Air Flow Patterns in the Chamber. (a) Attached Flow, (b) Detached Flow.	31
2	Needle Assembly - Final Design.	33
3	Damage of the Needle Tip.	33
4	New Arrangement of the Pressure Switches.	37
5	Schlieren System.	37
6a	Experimental Blast Wave Data, r' Versus t' , Regions A and C	40
6b	Experimental Blast Wave Data, r' Versus t' , Region B	41
6c	Averaged Blast Wave Data, r' Versus t'	42
7a	Experimental Blast Wave Data, r' Versus t' , Regions A and C	43
7b	Experimental Blast Wave Data, r' Versus t' , Region B	44
7c	Averaged Blast Wave Data, r' Versus t'	45
8a	Experimental Heterogeneous Data, r' Versus t' , Regions A and C	46
8b	Experimental Heterogeneous Data, r' Versus t' , Region B	47
8c	Averaged Heterogeneous Data, r' Versus t'	48
9a	Experimental Heterogeneous Data, r' Versus t' , Regions A and C	49
9b	Experimental Heterogeneous Data, r' Versus t' , Region B	50
9c	Averaged Heterogeneous Data, r' Versus t'	51
10	Photographs of Blast Wave Front at the Chamber Exit, E-106 + 1.75 grams	55
11	Photographs of Blast Wave Front at the Chamber Exit, E-106 + 3.0 grams	56

LIST OF FIGURES (concluded)

Figure	Title	Page
12	Photographs of Heterogeneous Wave Front at the Chamber Exit, E-106 + 1.75 grams	58
13	Photographs of Heterogeneous Wave Front at the Chamber Exit, E-106 + 3.0 grams	59
14	Phenomena Developed at the Wave Front. a. Blast Wave Front, E-106 + 1.75 grams b. Heterogeneous Wave Front, E-106 + 1.75 grams c. Heterogeneous Wave Front, E-106 + 3.00 grams d. Blast Wave Front, E-106 + 1.75 grams e. Heterogeneous Wave Front, E-106 + 1.75 grams	61
15	Experimental Heterogeneous Data, r' Versus t' .	64
16	Cases of Non-Uniform Fuel-Air Distribution. . .	67
17	Experimental Heterogeneous Data, r' Versus t' , Row Nos. 1, 2, 3, and 4 Removed.	70
18	Experimental Heterogeneous Data, r' Versus t' .	72
19	Experimental Heterogeneous Data, r' Versus t' .	73
20	Experimental Heterogeneous Data, r' Versus t' .	74
21	Experimental Heterogeneous Data, r' Versus t' .	75
22	Qualitative Trends of Experimental Non-Uniform Data, r' Versus t' . (a) E-106 + 3.0 grams (b) E-106 + 2.5 grams; (c) E-106 + 2.0 grams; (d) E-106 + 1.75 grams	75
23	Qualitative Trends of Experimental Non-Uniform Data, r' Versus t' . (a) Row 9 Removed; (b) Rows 9 and 10 Removed; (c) Rows 9, 10, and 11 Removed; (d) Rows 9, 10, 11, and 12 Removed	79

LIST OF TABLES

Table	Title	Page
1	Non-Homogeneous Results	81

LIST OF ABBREVIATIONS, ACRONYMS, AND SYMBOLS

A, B, C	species
a, b, c	stoichiometric coefficients of species A, B, C , respectively
B	Arrhenius pre-exponential factor
C	velocity of sound
C	species concentration
C_p	specific heat at constant pressure
E_A	activation energy
h	enthalpy
j	geometrical coefficient
k_f	Arrhenius pre-exponential constant
ℓ_c	induction distance
M	molecular weight
M_s	shock Mach number
p	pressure
Q	heat release per unit mass of the mixture
q_a	effective heat release per unit mass of species A
R_s	shock radius
\dot{R}_s	shock velocity
R	gas constant
r	radial distance
T	temperature
T_A	activation temperature, E_A/R
t	time
u	velocity
W	reaction rate, mass/volume/time
w	$(\dot{R}_s - u)/R_s$

x	$R_s - r$
y	mass fraction
y_i	y_i/y_{i_0}
β	T_s/T_A
Γ	ratio of specific heats
ϵ	ℓ_c/R_s
η	$(R_s - r)/\ell_c$
θ	$[(T - T_s)/T] (1/\beta)$
θ	$R_s \dot{R}_s / \dot{R}_s^2$
ν	bM_b/aM_a
ρ	density
τ	t/τ_B
τ_B	R_s/\dot{R}_s

Subscripts

i	corresponding to species i
o	initial state
s	shock

Superscripts

$(\bar{\quad})$	dimensional variables
r	reference conditions for enthalpy
o	first approximation

SECTION I

INTRODUCTION

Five years ago the contractor embarked on a research investigation for the Air Force Armament Laboratory, Eglin AFB, Florida, entitled "Fundamental Aspects of Unconfined Explosions." This work was initiated under Air Force Contract F08635-71-C-0083. In 1974, this contract terminated, but the research was continued under Contract F08635-74-C-0123.

The motivation behind this study was to identify and evaluate some of the more major and basic factors involved in unconfined explosions. The significance of the word "unconfined" is that the combustible mixture is not confined within a solid structure (such as the cylinder of an engine, a building, etc.) but, rather, exists as a cloud with only a gaseous surrounding. The Air Force interest involves fuel-air explosions, but the phenomena are the same as that experienced with liquified natural gas spills, fuel pipeline bursts, etc. In the fuel-air explosion case, blast wave initiation of detonation is employed. In other cases, detonation might occur as the result of acceleration of a deflagration wave or, again, by a blast wave. In the earlier studies, detailed attention was given to, and progress made on, the following aspects of the problem:

1. Theoretical analysis of planar, cylindrical, and spherical blast waves and detonation waves through clouds.
2. Evaluation of ground impulse and dynamic impulse obtained from such waves.

3. Development of an experimental facility to study the propagation of cylindrical blast waves and blast wave-initiated detonation waves through homogeneous or heterogeneous mixtures.
4. Analytical evaluation of the difference in impulse between a homogeneous and heterogeneous detonation, each having the same heat release.
5. Controlled experimental studies of cylindrical blast waves and blast wave-initiated homogeneous and heterogeneous detonation waves.
6. Development of a regression technique for fitting the experimental data to a blast wave decay portion followed by constant velocity detonation.
7. Analytical evaluation of the influence of side relief on detonation and impulse characteristics.
8. Determination of threshold energy for the blast wave initiation of detonation.

The foregoing aspects are described in detail in the annual reports issued on the project⁽¹⁻³⁾ and in other publications⁽⁴⁻⁷⁾.

As for the present contracted work, one project report has been published⁽⁸⁾ and a professional thesis⁽⁹⁾ has been completed which includes work from both contract efforts. The project report⁽⁸⁾ includes:

1. A completed analysis of the ground impulse generated by a fuel-air explosion with side relief.

2. A complete simplified analysis of the blast wave initiation of detonation, which will appear in the open literature⁽¹⁶⁾.
3. The extent of our analysis of the blast propagation beyond the fuel cloud.
4. A description of the major modifications to the experimental facility which resulted in almost doubling the radius of the sectored shock tube.
5. A rather complete study of the generation of strong cylindrical blast waves.
6. Extensive experiments on all gaseous (MAPP-air) detonations in the extended chamber.
7. A complete description of the mathematical regression technique for modeling blast-initiated detonations in fuel-air mixtures.

The material presented in this report represents the research conducted during the last eight months of the project. The recent work on extension of the analysis of blast wave-initiated detonation is presented. Some operating characteristics of the experimental facility that have a noticeable effect on the development of detonation are discussed. Also, a section on the photographic study of the wave shape of blast waves and heterogeneous detonation waves is included. Finally, some experiments on the propagation of heterogeneous detonation through a non-uniform cloud are presented and discussed. The non-uniformity is obtained by

removing the fuel needles (which produce the drops) from the desired zone of the cloud. Two fuel devoid zones have been studied: one in the vicinity of the blast wave-detonation wave transition region and the other at a region further downstream after detonation was established.

SECTION II

RESEARCH RESULTS

A. DERIVATION OF THE APPROXIMATE GOVERNING EQUATIONS DESCRIBING THE INDUCTION ZONE STRUCTURE BEHIND A NONSTEADY SHOCK WAVE IN A REACTING MEDIUM

INTRODUCTION

In the analysis of the blast initiation of a combustible mixture, the importance of ignition delay has been recognized in the literature for several years now. It has been shown⁽¹⁰⁾ that if the detonation is treated as a single discontinuous front, then the wave velocity always reaches its C-J value. However, if the effect of induction distance behind the leading shock is taken into account, one can see even intuitively that the total chemical energy released in this case would be less than in the case of a single front detonation wave. Consequently at the same radius, the strength of shock will be weaker (for the same explosion energy) when the ignition delay is taken into account. This idea is the backbone of the analysis of Bach and Lee⁽¹⁰⁾ for including a phenomenological model to account for induction delay variation in the analysis.

In the present analysis, an attempt has been made to derive the governing differential equations to describe the variation of the induction distance as a function of shock radius under certain realistic restrictions. Although the fluid dynamics and the chemical processes occurring in a blast initiation problem are coupled and interactive, they occur on different scales of length and time. The chemical processes occur on a

characteristic length scale of the order of the blast wave radius, ℓ_c , provided certain conditions (to be discussed later) are met. The concept of induction distance is valid for a large activation energy ($E_A \gg RT_s$). This is the first restriction. The second restriction is that $\ell_c \ll R_s$, so that the hydrodynamic gradients due to the expansion fan trailing the leading shock will be negligible over the length scale ℓ_c . This assumption also implies that the characteristic chemical time scale is much smaller than the hydrodynamic time scale associated with the blast decay. In short as shown in the analysis, under these restrictions, in the first approximation the problem is reduced to finding the structure of a quasisteady detonation wave.

BASIC EQUATIONS

One dimensional, nonsteady equations for asymmetric flow are listed below. Bars are used to denote the dimensional quantities.

Continuity

$$\frac{\partial \bar{\rho}}{\partial \bar{t}} + \bar{u} \frac{\partial \bar{\rho}}{\partial \bar{r}} + \bar{\rho} \frac{\partial \bar{u}}{\partial \bar{r}} + \frac{(j-1)}{\bar{r}} \bar{u} = 0 \quad (1)$$

where $j = 1, 2, 3$ for plane, cylindrical and spherical flow, respectively.

Momentum

For an inviscid flow without any body forces,

$$\frac{\partial \bar{u}}{\partial \bar{t}} + \bar{u} \frac{\partial \bar{u}}{\partial \bar{r}} + \frac{1}{\bar{\rho}} \frac{\partial \bar{p}}{\partial \bar{r}} = 0 \quad (2)$$

Energy

Neglecting external heat transfer and work done by the body forces,

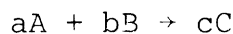
$$\frac{D}{Dt} \left(\bar{h} + \frac{\bar{u}^2}{2} \right) = \frac{1}{\bar{\rho}} \frac{\partial \bar{p}}{\partial t} \quad (3)$$

Species

Let Y_i be the mass fraction of species i and \bar{W}_i be the mass rate of production of species i per unit volume of the mixture, then ignoring diffusion,

$$\bar{\rho} \frac{DY_i}{Dt} = \bar{W}_i$$

In the present analysis a single step irreversible reaction will be considered in which two reactants (oxidizer and fuel) react to produce a single product, i.e.



Such an overall description of the reaction has been used by a number of investigators⁽¹¹⁻¹³⁾ as a simple model of combustion kinetics. A number of useful expressions for chemical production rate⁽¹¹⁾ and ignition delay time^(12,13) have been derived by using such an overall combustion kinetics model.

Let M_i denote the molecular weight of species i . Thus,

$$\frac{(\bar{W}_a/M_a)}{(\bar{W}_b/M_b)} = \frac{a}{b}$$

or
$$\bar{W}_a = \frac{a}{b} \frac{M_a}{M_b} \bar{W}_b$$

$$= \bar{W}_b / \nu \quad (4)$$

where
$$v = \frac{bM_b}{aM_a} \quad (5)$$

Now

$$\begin{aligned} \bar{W}_c &= - (\bar{W}_a + \bar{W}_b) \\ &= - (1 + v) \bar{W}_a \end{aligned} \quad (6)$$

The species equations become

$$\bar{\rho} \frac{DY_a}{Dt} = \bar{W}_a \quad (7)$$

$$\begin{aligned} \bar{\rho} \frac{DY_b}{Dt} &= \bar{W}_b = v \bar{W}_a \\ &= \bar{\rho} v \frac{DY_a}{Dt} \end{aligned} \quad (8)$$

Similarly

$$\begin{aligned} \bar{\rho} \frac{DY_c}{Dt} &= + \bar{W}_c = - (1 + v) \bar{W}_a \\ &= - (1 + v) \frac{DY_a}{Dt} \end{aligned} \quad (9)$$

Equations (8) and (9) can be easily integrated:

$$v(Y_a - Y_{a_0}) = Y_b - Y_{b_0} \quad (10)$$

and
$$- (1 + v) (Y_a - Y_{a_0}) = Y_c - Y_{c_0} \quad (11)$$

where Y_{a_0} , Y_{b_0} and Y_{c_0} are initial mass fractions of species A, B, and C, respectively.

Using the law of mass action and the Arrhenius kinetics, the following well known equation may be written

$$\frac{DC_a}{Dt} = -k_f C_a^a C_b^b e^{-E_A/RT}$$

where C_i is the species concentration for i^{th} species and E_A is the activation energy.

In the literature⁽¹¹⁾, the above expression has been adopted with the following modification

$$\bar{W}_a = -k_f \rho^n C_a^m C_b^k \exp(-E_A/RT)$$

in which k_f , E_A , n , m , and k are determined experimentally⁽¹¹⁾. In the present analysis, the following model will be adopted.

$$\bar{W}_a = -B \bar{\rho} Y_a^a Y_b^b e^{-\bar{T}_A/\bar{T}} \quad (12)$$

where

$$\bar{T}_A = E_A/R$$

Enthalpy

For a chemically reacting flow, the specific enthalpy \bar{h} will be

$$\bar{h} = \sum_i \bar{h}_i Y_i$$

where

$$\bar{h}_i = \bar{h}_i^r + \int_{\bar{T}^r}^{\bar{T}} \bar{C}_{p_i} d\bar{T}$$

Assume \bar{C}_{p_i} to be independent of temperature.

$$\bar{h}_i = \bar{h}_i^r + \bar{C}_{p_i} (\bar{T} - \bar{T}^r)$$

$$\bar{h} = (\bar{T} - \bar{T}^r) \sum_i \bar{C}_{p_i} Y_i + \sum_i \bar{h}_i^r Y_i$$

Define
$$\bar{C}_p = \sum_i \bar{C}_{p_i} Y_i \quad (13)$$

$$\bar{h} = \bar{C}_p (\bar{T} - \bar{T}^r) + \sum_i \bar{h}_i^r Y_i$$

let
$$q_a = \bar{h}_a^r + v \bar{h}_b^r - (1 + v) \bar{h}_c^r \quad (14)$$

or
$$\sum_i \bar{h}_i^r Y_i = q_a (Y_a - Y_{a_o}) + \sum_i \bar{h}_i^r Y_{i_o} \quad (15)$$

Thus the expression for enthalpy h becomes,

$$\bar{h} = \bar{C}_p (\bar{T} - \bar{T}^r) + q_a (Y_a - Y_{a_o}) + \sum_i \bar{h}_i^r Y_{i_o} \quad (16)$$

Equation of State

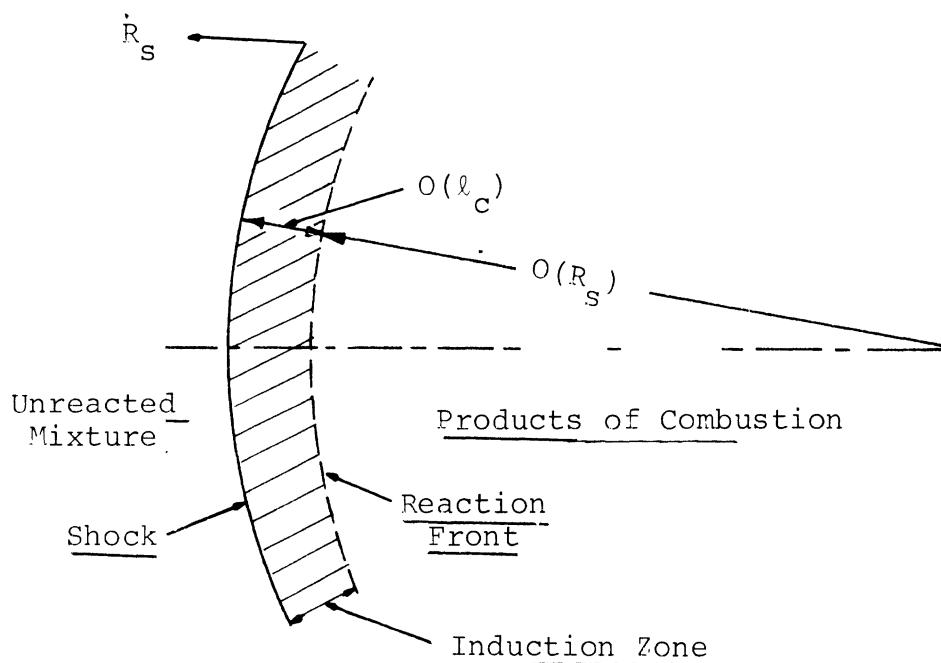
$$\bar{p} = \bar{p}_R \bar{T} / M \quad (17)$$

where

$$1/M = \sum_i (Y_i / M_i)$$

Determination of Time and Distance Scales

The flow processes in a blast wave moving in a reacting medium may be looked at on two different time and distance scales, namely the chemical and the hydrodynamic scales. If a fluid element enters the shock and moves away relative to the shock, appreciable chemical reaction starts when it is at a distance of the order of induction distance from the shock. The time scale associated with this distance scale is induction time. Thus, in studying the change in chemical properties of the flow immediately behind the shock, the proper length and time scales associated with the flow are those for the induction process. On the other hand, the flow properties associated with the blast wave change on the length and time scale associated with the blast wave motion, namely the blast wave radius R_s and R_s/\dot{R}_s (\dot{R}_s being the blast velocity). These characteristic lengths are shown in the sketch below.



The concept of induction process has been evolved to represent the abrupt and explosive onset of the chemical reaction in combustion process. The fluid element remains dormant up to the induction time (or induction length, whichever is convenient to consider) after which the so-called thermal runaway occurs. As noted in the literature, this behavior is attributed primarily to the presence of the exponential term in the Arrhenius rate expression which changes very rapidly when the activation energy $E_A \gg RT_S$. The translation of this qualitative concept into a mathematical one follows below. Consider a fluid element immediately after crossing the shock at the postshock temperature \bar{T}_S and the corresponding reaction rate $(\bar{W}_a)_{\bar{T}_S}$ which is assumed to be small. Now, the question is, at what temperature \bar{T} does the relative change in the reaction rate become of order unity? That is,

$$\Delta \bar{W} = \frac{(\bar{W}_a)_{\bar{T}} - (\bar{W}_a)_{\bar{T}_S}}{(\bar{W}_a)_{\bar{T}_S}} \sim O(1)$$

where $(\bar{W}_a)_{\bar{T}}$ is the reaction rate at temperature \bar{T} . If it is assumed that the change in the reactant concentration in this period is small, then

$$\Delta \bar{W} = O\left(\frac{e^{-\bar{T}_A/\bar{T}} - e^{-\bar{T}_A/\bar{T}_S}}{e^{-\bar{T}_A/\bar{T}_S}}\right) = O\left(e^{\frac{\bar{T}-\bar{T}_S}{\bar{T}_S^2} \bar{T}_A} - 1\right)$$

provided $\bar{T} = O(\bar{T}_S)$.

When \bar{T} is such that $[(\bar{T} - \bar{T}_S)/\bar{T}_S] \sim O(\bar{T}_S/\bar{T}_A)$, then $\Delta \bar{W} \sim O(1)$ or $[(\bar{T} - \bar{T}_S)/\bar{T}_S] \sim O(\beta)$ where $\beta = \bar{T}_S/\bar{T}_A$.

In order to estimate the corresponding change in the reactant mass fraction, the expression for enthalpy given by Equation (16) is examined. The change in enthalpy is given by

$$\Delta \bar{h} = \bar{C}_p \Delta \bar{T} + q_a \Delta Y_a$$

where Δ represents a change in the value of a particular quantity.

When the change in the chemical composition of a fluid element becomes significant, both the terms on the right-hand side of the above expression are of the same order.

$$(\bar{C}_p \Delta \bar{T}) \sim O(q_a \Delta Y_a)$$

$$\Delta Y_a \sim O\left(\frac{q_a}{\bar{C}_p \bar{T}_s}\right) \beta$$

Assuming that $[q_a / (\bar{C}_p \bar{T}_s)] \sim O(1)$, then

$$\Delta Y_a \sim O(\beta)$$

The above equation also validates the earlier assumption that $Y_a \approx Y_{a_0}$ in the induction zone if β is small (i.e., reactant assumption is negligible). All the relevant information needed to estimate the scale of the induction zone is now at hand.

Now from the species Equation (7) and the rate Equation (12), it follows that

$$\frac{\partial Y_a}{\partial \bar{t}} + \bar{u} \frac{\partial Y_a}{\partial \bar{r}} = -B Y_a^a Y_b^b e^{-\bar{T}_A / \bar{T}}$$

In the above equation, as discussed earlier, the proper time scale is the characteristic blast time $\tau_B = R_S/\dot{R}_S$. Again, as discussed earlier, the proper length scale for studying the induction process is the induction length. This scale may be found by equating the order of magnitude of the spatial derivative term and the chemical production rate term in the Equation (7).

The order of the chemical production rate and $\bar{u}(\partial Y_a/\partial \bar{r})$ can be estimated in the induction zone by noting that $\bar{u} \sim \dot{R}_S$, $\Delta \bar{r} \sim \ell_c$, $\Delta Y_a/Y_{a_0} \sim O(\beta)$, $Y_a \sim Y_{a_0}$, $Y_b \sim Y_{b_0}$ and $\bar{T} \sim \bar{T}_s$ or

$$\bar{u} \frac{\partial Y_a}{\partial \bar{r}} = O\left(\frac{\dot{R}_S \beta Y_{a_0}}{\ell_c}\right)$$

and

$$B Y_{a_0}^a Y_{b_0}^b e^{-\bar{T}_A/\bar{T}} \sim O(B Y_{a_0}^a Y_{b_0}^b e^{-\bar{T}_A/\bar{T}_s})$$

Equating both orders of magnitude,

$$\ell_c = \frac{\beta \dot{R}_S e^{\bar{T}_A/\bar{T}_s}}{B Y_{a_0}^{a-1} Y_{b_0}^b} \quad (18)$$

The important ideas discussed previously can now be summarized as follows. The unsteady nature of the problem is attributed to the blast wave decay, and the proper time scale for such a decay process is R_S/\dot{R}_S . The chemical change begins at a distance $O(\ell_c)$ from the leading shock, and thus the proper

length scale for spatial stretching in the induction zone is ℓ_c . The operators appearing in the differential equations (1), (2), (3), and (7) are worked out in terms of properly stretched inner variables in Appendix A.

TRANSFORMATION TO INNER VARIABLES

Equations will be formulated using the dimensionless (unbarred) inner variables listed below:

$$\begin{aligned} \tau_B &= R_s / \dot{R}_s & \bar{W} &= (\dot{R}_s - \bar{u}) / \dot{R}_s & \tau &= \bar{t} / \tau_B \\ \rho &= \bar{\rho} / \rho_0 & p &= \bar{p} / p_0 & \eta &= (R_s - \bar{r}) / \ell_c \\ u &= \bar{u} / \dot{R}_s & h &= \bar{h} / \bar{C} p_0 T_0 & Y_i &= Y_i / Y_{i_0} \end{aligned}$$

The subscript zero refers to conditions in the undisturbed medium ahead of the wave.

Continuity

In terms of the above dimensionless variables Equation (1) becomes

$$\begin{aligned} \frac{\dot{R}_s}{\ell_c} \left(W - \frac{\ell_c}{R_s} \eta \right) \frac{\partial \rho}{\partial \eta} + \frac{1}{\tau_B} [1 - \tau(1 - \theta)] \frac{\partial \rho}{\partial \tau} \\ + \rho \left\{ \frac{\dot{R}_s}{\ell_c} \frac{\partial W}{\partial \eta} + \frac{(j - 1)}{\left(1 - \frac{\ell_c}{R_s} \eta \right)} \frac{\dot{R}_s}{R_s} (1 - W) \right\} = 0 \end{aligned}$$

where

$$\theta = \frac{R_s \ddot{R}_s}{\dot{R}_s^2}$$

This equation may be easily simplified to

$$\left(W - \frac{\ell c}{R_s} \eta \right) \frac{\partial \rho}{\partial \eta} + \frac{\ell c}{R_s} [1 - \tau(1 - \theta)] \frac{\partial \rho}{\partial \tau} + \rho \frac{\partial W}{\partial \eta} + \frac{\rho(j-1)}{1 - \frac{\ell c}{R_s} \eta} \frac{\ell c}{R_s} (1 - W) = 0 \quad (19)$$

Momentum Equation

In the transformed coordinates, the momentum Equation (2) becomes

$$\frac{\ell c}{R_s} \theta (1 - W) - \left(W - \frac{\ell c}{R_s} \eta \right) \frac{\partial W}{\partial \eta} - \frac{\ell c}{R_s} [1 - \tau(1 - \theta)] \frac{\partial W}{\partial \tau} - \frac{1}{\Gamma M_s^2 \rho} \frac{\partial p}{\partial \eta} = 0 \quad (20)$$

Energy Equation

In dimensionless variables the energy Equation (3) becomes

$$\frac{D}{Dt} h + \frac{(\Gamma_o - 1)}{2} M_s^2 (1 - W)^2 = \frac{\Gamma_o - 1}{\Gamma_o} \frac{1}{\rho} \frac{\partial \bar{p}}{\partial \bar{t}}$$

For convenience introduce

$$G_1 = h + \frac{\Gamma_o - 1}{2} M_s^2 (1 - W)^2$$

Then the energy equation becomes

$$\rho W \frac{\partial G_1}{\partial \eta} - \frac{\Gamma_o - 1}{\Gamma_o} \frac{\partial p}{\partial \eta} + \frac{\ell c}{R_s} \rho [1 - \tau(1 - \theta)] \frac{\partial G_1}{\partial \tau} - \rho \theta F \eta \frac{\partial G_1}{\partial \eta} + \frac{\Gamma_o - 1}{\Gamma_o} \theta F \eta \frac{\partial p}{\partial \eta} - [1 - \tau(1 - \theta)] \frac{\partial p}{\partial \tau} = 0 \quad (21)$$

Now

$$G_1 = h + \frac{\Gamma_O - 1}{2} M_S^2 [W^2 + (1 - 2W)] = G + \frac{\Gamma_O - 1}{2} M_S^2 (1 - 2W)$$

$$\text{where} \quad G = h + \frac{\Gamma_O - 1}{2} M_S^2 W^2 \quad (22)$$

$$\text{Then:} \quad \rho W \frac{\partial G_1}{\partial \eta} = \rho W \frac{\partial G}{\partial \eta} - (\Gamma_O - 1) M_S^2 \rho W \frac{\partial W}{\partial \eta} \quad (23)$$

$$\frac{\partial G_1}{\partial \tau} = \frac{\partial G}{\partial \tau} + (\Gamma_O - 1) M_S^2 \frac{\theta(1 - 2W)}{[1 - \tau(1 - \theta)]} - \frac{\partial W}{\partial \tau} \quad (24)$$

Also, from the momentum Equation (20)

$$\begin{aligned} \rho W \frac{\partial W}{\partial \eta} &= \rho \frac{c}{R_S} \theta(1 - W) + F \theta \eta \frac{\partial W}{\partial \eta} \\ &- [1 - \tau(1 - \theta)] \frac{\partial W}{\partial \tau} - \frac{1}{\Gamma_O M_S^2} \frac{\partial p}{\partial \eta} \end{aligned} \quad (25)$$

Combining Equations (21),(22),(23),(24),(25), and (A-5), and rearranging the energy equation finally can be written

$$\begin{aligned} W \frac{\partial G}{\partial \eta} + \frac{c}{R_S} [1 - \tau(1 - \theta)] \rho \frac{\partial G}{\partial \tau} - \frac{\Gamma_O - 1}{\Gamma_O} \frac{\partial p}{\partial \tau} \\ - \rho (\Gamma_O - 1) \theta M_S^2 W \\ + \theta F \eta \frac{\Gamma_O - 1}{\Gamma_O} \frac{\partial p}{\partial \eta} - \rho \frac{\partial G}{\partial \eta} = 0 \end{aligned} \quad (26)$$

Species Equation

$$\frac{\partial y_a}{\partial \bar{t}} + \dot{R}_S \bar{u} \frac{\partial y_a}{\partial \bar{r}} = - B y_{aO}^{a-1} y_{bO}^b e^{-T_A/T_S} (y_a^a y_b^b e^\theta)$$

where

$$\theta = \frac{T - T_s}{T} \frac{E_A}{R} = \frac{T - T_s}{T} \frac{1}{\beta} \quad (27)$$

$$\beta = RT_s/E_A \quad (28)$$

In dimensionless variables the species Equation (7) can be easily reduced to

$$\begin{aligned} W \frac{\partial y_a}{\partial \eta} + \frac{\ell_c}{R_s} [1 - \tau(1 - \theta)] \frac{\partial y_a}{\partial \tau} - F \theta \eta \frac{\partial y_a}{\partial \eta} \\ = - \beta Y_a^a Y_b^b e^\theta \end{aligned} \quad (29)$$

There are two small parameters appearing in the above equations, namely $\epsilon = \ell_c/R_s$ and $\beta = RT_s/E_A$. This suggests the possibility of a double expansion as discussed below.

A function f may be expanded first in a series in the powers of a small parameter ϵ

$$f = f^0 + \epsilon f^1 + \epsilon^2 f^2 + \dots$$

where each of the f^i , $i = 0, 1, 2, \dots$ can be individually expanded in the powers of a small parameter β , i.e.

$$f^i = f^{i0} + \beta f^{i1} + \beta^2 f^{i2} + \dots$$

The purpose of the present analysis is to compute the first-order approximation of the rate of growth of the induction zone width. Therefore, it is unnecessary to develop an elaborate double expansion scheme which is both tedious and lengthy. Instead, it will be assumed that $\beta \gg \ell_c/R_s$, for then the desired first approximation can be obtained with great simplicity. This simplification becomes obvious when the term βe^θ in the species Equation (29) is expanded as shown below.

Note that

$$\theta = \frac{T - T_s}{T} \frac{1}{\beta}$$

Now define

$$\theta_s = \frac{T - T_s}{T_s} \frac{1}{\beta} \quad (30)$$

so that

$$T = T_s (1 + \beta \theta_s) \quad (31)$$

or

$$\theta = \theta_s \frac{T_s}{T} = \frac{\theta_s}{(1 + \beta \theta_s)}$$

$$= \theta_s \left(1 - \beta \theta_s + \frac{\beta^2}{2} \theta_s^2 - \frac{\beta^3}{3} \theta_s^3 + \dots \right)$$

and

$$e^\theta = e^{\theta_s} e^{(-\beta \theta_s^2 + \frac{\beta^2}{2} \theta_s^3 - \frac{\beta^3}{3} \theta_s^4 + \dots)}$$

$$= \left(1 - \beta \theta_s^2 + \frac{\beta^2}{2} \theta_s^4 + \frac{\theta_s^3}{2} + \dots \right) e^{\theta_s}$$

(32)

Then, combining Equations (29) and (32)

$$\begin{aligned} W \frac{\partial y_a}{\partial \eta} + \frac{\ell_c}{R_s} [1 - \tau(1 - \theta)] \frac{\partial y_a}{\partial \tau} - F \theta \eta \frac{\partial y_a}{\partial \eta} \\ = - y_a^a y_b^b e^{\theta_s} \left(\beta - \beta^2 + \beta^3 \theta_s^4 + \frac{\theta_s^3}{2} + \dots \right) \end{aligned}$$

Now expanding W , y_a and y_b , etc., in powers of $\varepsilon = \ell_c/R_s$ yields

$$W = W^0 + \varepsilon W^1 + \varepsilon^2 W^2 + \dots$$

$$y_a = y_a^0 + \varepsilon y_a^1 + \varepsilon^2 y_a^2 + \dots$$

$$F = F^0 + \varepsilon F^1 + \dots$$

$$\theta = \theta^0 + \varepsilon \theta^1 + \dots$$

$$\begin{aligned}
\theta_s &= \theta_s^0 + \epsilon \theta_s^1 + \epsilon^2 \theta_s^2 + \dots \\
\rho &= \rho^0 + \epsilon \rho^1 + \epsilon^2 \rho^2 \\
p &= p^0 + \epsilon p^1 + \epsilon^2 p^2 + \dots \\
G &= G^0 + \epsilon G^1 + \epsilon^2 G^2 + \dots \\
M^2 &= M^0 + \epsilon M^1 + \epsilon^2 M^2 + \dots \\
T &= T^0 + \epsilon T^1 + \epsilon^2 T^2 + \dots
\end{aligned} \tag{33}$$

θ_s and T are related to each other by Equation (31) as follows

$$\begin{aligned}
T^0 + \epsilon T^1 + \epsilon^2 T^2 + \dots &= T_s [1 + \beta (\theta_s^0 + \epsilon \theta_s^1 + \dots)] \\
&= T_s (1 + \beta \theta_s^0) + \epsilon (\beta T_s \theta_s^1) + \epsilon^2 \dots
\end{aligned}$$

or

$$T^0 = T_s (1 + \beta \theta_s^0) \tag{34}$$

$$T^1 = \beta T_s \theta_s^1 \tag{35}$$

Similarly, it is possible to establish the way the decay parameter θ and the wave radius R_s vary as a function of Mach number. However, as shown later, since θ does not occur in the first approximation, there is no need to consider the expansion for θ in detail.

Thus in the species equation

$$\begin{aligned}
e^{\theta_s} &= e^{\theta_s^0} + \epsilon \theta_s^1 + \epsilon^2 \theta_s^2 + \dots \\
&= e^{\theta_s^0} \left(1 + \epsilon \theta_s^1 + \epsilon^2 \theta_s^2 + \frac{\theta_s^1{}^2}{2} + \dots \right)
\end{aligned}$$

Substituting all the expansion, the species equation now yields:

$$\begin{aligned}
& (W^0 + \epsilon W^1 + \epsilon^2 W^2 + \dots) \frac{\partial Y_a^0}{\partial \eta} + \epsilon \frac{\partial Y_a^1}{\partial \eta} + \epsilon^2 \frac{\partial Y_a^2}{\partial \eta} + \dots \\
& + \epsilon \{ [1 - \tau(1 - \theta^0)] + \epsilon \theta^1 + \dots \} \frac{\partial Y_a^0}{\partial \tau} + Y_a^0 \frac{\partial \epsilon}{\partial \tau} + \dots \\
& - (F^0 + \epsilon F^1 + \epsilon^2 F^2 + \dots) (\theta^0 + \epsilon \theta^1 + \epsilon^2 \theta^2 + \dots) \\
& \quad \times \left[\frac{\partial Y_a^0}{\partial \eta} + \epsilon \frac{\partial Y_a^1}{\partial \eta} + \dots \right] \eta \\
& = - (Y_a^0 + \epsilon Y_a^1 + \dots)^a (Y_b^0 + \epsilon Y_b^1 + \dots)^b \\
& \quad [\beta - \beta^2 \theta (\theta_s^0)^2 + 2\epsilon \theta_s^0 \theta_s^1 + \dots] + \dots \\
& \quad [1 + \epsilon \theta_s^1 + \dots] e^{\theta_s^0}
\end{aligned}$$

Equating the coefficients of ϵ^0 yields the first order equation

$$W^0 \frac{\partial Y_a^0}{\partial \eta} = - Y_a^0{}^a Y_b^0{}^b \beta e^{\theta_s^0} \quad (36)$$

where

$$\theta_s^0 = \frac{T^0 - T_s}{T_s} \frac{1}{\beta} \quad (34)$$

The derivation of the other first-order equations is straightforward, and these equations are listed below

Continuity:
$$W^0 \frac{\partial \rho^0}{\partial \eta} + \rho^0 \frac{\partial W^0}{\partial \eta} = 0 \quad (37)$$

Momentum:
$$\rho^0 W^0 \frac{\partial W^0}{\partial \eta} + \frac{1}{\Gamma_0 M_s} \frac{\partial p^0}{\partial \eta} = 0 \quad (38)$$

Energy:
$$\rho^0 W^0 \frac{\partial G^0}{\partial \eta} = 0 \quad (39)$$

Note that G is a function of T , y_a , and W ; thus, G^0 may be expressed as a function of T^0 , y_a^0 , and W^0 using Equation (22)

$$G = h + \frac{\Gamma_0 - 1}{2} M_s^2 W^2 \quad (22)$$

where

$$h = C_{p_o}^h T_o = C_p (T - T^r) + Q(y_a - 1) + \frac{\sum h_i^r y_{a_o}}{C_{p_o} T_o}$$

with

$$Q = q_a y_{a_o}$$

Expanding both sides of Equation (22) now yields

$$\begin{aligned} G^0 + \epsilon G^1 + \dots &= C_p (T^0 - T^r) + Q(y_a^0 - 1) + \frac{\sum h_i^r y_{i_o}}{C_{p_o} T_o} \\ &+ \epsilon [-C_p T^2 + Q y_a^1] + \epsilon^2 [\quad] \dots \\ &+ \frac{\Gamma_0 - 1}{2} (M_s^0{}^2 + \epsilon M_s^1{}^2 + \epsilon^2 M_s^2{}^2 + \dots) \\ &\times (W^0{}^2 + 2\epsilon W^0 W^1 + \dots) \end{aligned}$$

and it follows that

$$G^0 = C_p (T^0 - T^r) + Q(y_a^0 - 1) + \frac{h_i^r Y_{i_0}}{C_{p_0} T_0} + \frac{\Gamma_0 - 1}{2} M_s^0{}^2 W^0{}^2 \quad (40)$$

$$G^1 = -C_p T^1 + Q y_a^1 + \frac{\Gamma_0 - 1}{2} (M_s^1{}^2 W^0{}^2 + 2W^0 W^1 M_s^0{}^2) \quad (41)$$

In a similar way, it is possible to derive the boundary conditions at the shock (moving boundary). The appropriate flow properties immediately behind the shock will be denoted by a subscript s. Mass conservation across the shock yields

$$\overline{\rho_s} (R_s - \overline{u_s}) = \rho_0 R_s$$

or in terms of dimensionless inner variables

$$\rho_s W_s = 1$$

Using the expansion (33) then yields

$$\rho_s^0 W_s^0 = 1 \quad (42)$$

for the zeroth order boundary condition at the shock.

Across the shock conservation of momentum yields

$$\bar{p}_s + \bar{\rho}_s (\dot{R}_s - \bar{u}_s)^2 = p_o + \rho_o \dot{R}_s^2$$

or in terms of dimensionless inner variables

$$p_s + \rho_s W_s^2 \Gamma_o M_s^2 = \Gamma_o M_s^2 + 1$$

Substituting the expansion (33), it can be easily shown, that to zeroth order

$$\frac{p_s^0}{\Gamma_o M_s^2} + Q_s^0 W_s^2 = 1 + \frac{1}{\Gamma_o M_s^2} \quad (43)$$

Conservation of energy across the shock expressed in dimensionless inner variables yields

$$h_s + \frac{W_s^2}{2} = h_o + \frac{\dot{R}_s^2}{2}$$

or

$$h_s + \frac{W_s^2}{2} = h_o + R_s^2 / 2C_{p_o} T_o$$

Note that

$$h_o = \frac{\sum_i h_i^{r^0} Y_{i_o}^0}{C_{p_o} T_o} + \frac{C_p}{C_{p_o}} (1 - T^r)$$

and to zeroth order

$$h_s^0 + \frac{r_o - 1}{2} M_s^0 W_s^0 = h_o + \frac{r_o - 1}{2} M_s^0 W_s^0 \quad (44)$$

where

$$h_s^0 = C_p (T_s^0 - T^r) + \frac{\sum_i h_i^{r^1} Y_{i_o}^1}{C_{p_o} T_o} + \Omega (Y_{a_s}^0 - 1)$$

It will be assumed that no reaction has occurred immediately behind the shock front, so that $Y_{i_s} = Y_{i_o} = 1$.

Thus

$$h_s^0 = C_p (T_s^0 - T^r) + \frac{\sum_i h_i^{r^1} Y_{i_o}^1}{C_{p_o} T_o} \quad (45)$$

Equation of State

Equation (17) may be rewritten in dimensionless form as follows

$$p \sum_i \frac{Y_{i_o}}{M_i} = \rho T \sum_i \frac{Y_i}{M_i}$$

Again, using expansions for p , ρ , T and Y_i , it can be easily shown that the coefficient of ϵ^0 will yield,

$$P_s^0 = \rho_s^0 T_s^0 \quad (46)$$

Note that Equations (36), (37), (38), and (39) form a set of differential equations which must be solved to find the first approximation of the induction zone structure. Equations (37), (38), and (39) are readily integrated. The constant of integration is determined by using the boundary conditions at the shock front.

Continuity

$$\begin{aligned} \rho^0 W^0 &= \text{constant} \\ &= \rho_s^0 v_s^0 \text{ at the shock boundary.} \end{aligned} \quad (47)$$

Momentum

$$\rho^0 W^0 + \frac{P^0}{\Gamma_s M_s^0} = \rho_s^0 W_s^0 + \frac{P_s^0}{\Gamma_o M_s^0} \quad (48)$$

Energy

$$h^0 + \frac{\Gamma_o - 1}{2} M_s^0 W^0 = h_s^0 + \frac{\Gamma_o - 1}{2} M_s^0 W_s^0 \quad (49)$$

Equations (47) through (49) and the species Equation (36) (which cannot be integrated), together with the boundary conditions (42), (43), (44) and the Equation of State (46), form a complete set of equations. The form of these equations suggest that, in the first approximation, the wave may be considered quasi-steady provided $\epsilon \ll 1$.

RESULTS AND DISCUSSION

The first approximation of the governing equations and the boundary conditions for the description of the reaction zone structure have been formulated. These equations are valid strictly when $\epsilon \ll 1$. The significance of $\epsilon \ll 1$ is that the chemical characteristic length must be much smaller than the blast wave radius. It can be seen, intuitively, that this condition will be amply satisfied at high shock Mach numbers with high post-shock temperature, and a corresponding narrow reaction zone width. Subject to this condition, the system of nonlinear partial differential equations simplify considerably. In the set of approximate governing equations, continuity, momentum, and energy equations are algebraic while the species equation is an ordinary differential equation. It is easily seen that the final form of these equations is identical to the equations describing the structure of a quasi-steady overdriven planar detonation wave. In other words, the effect of geometry has been eliminated. However, if the higher order approximations are worked out, then it can be shown that the effect of geometry appears in them only.

The mathematical form of the first order approximation of the governing equations derived here is similar to those for the thermal explosion problem with high activation energy, and recently several studies have been made^(14,15) to find their approximate solution using perturbation methods. It is felt

that fruitful results for reaction zone structure (induction distance in particular) may be obtained by following a similar approach. Once the induction zone is found as a function of radius, the computation of effective energy can be made in a way similar to Bach and Lee⁽¹⁰⁾ to predict the initiation of a reacting mixture.

B. PERFORMANCE CHARACTERISTICS OF THE CHAMBER

In the past, attention has been given to improving the performance characteristics of the chamber. Many of these improvements were presented in previous annual technical reports^(1-3,8). Two more modifications have been made which will be briefly discussed.

The first modification arose from the fact that circulation patterns were set up in the chamber prior to an experimental run. Under these conditions run to run reproducibility was adversely affected. The realization of this effect came about as follows. In an attempt to establish the operating conditions (pressure and frequency in the fuel system), the 147 needles of the drop generator were mounted in a special test rig outside the chamber. It was found that the fuel jets, and hence drops, were very sensitive to the external disturbances. The external disturbances usually produced a low frequency oscillatory motion of the fuel columns. Upon placing the rows of needles back in the chamber, a similar motion of the fuel jets was observed even though the fuel jets were relatively well protected from disturbances outside the chamber. When the chamber was ducted to the outside by means of a metal enclosure, the disturbances became even more intense. It was decided that the most likely explanation for this motion was the difference in temperature (and hence density) between the outside and inside.

In order to investigate this suspected motion, cigarette smoke was gently blown into the chamber through existing holes that were originally made for the pressure switches or transducers. The breech mounting was sealed with a transparent paper so the observations were possible. Using one hole at a time (a total of five different holes were used), the observations showed that the flow in the chamber, in general, followed two distinct patterns, as shown in Figure 1. When the temperature difference (about 5°) and, hence, the density gradient, was small, the flow in the chamber was laminar and always attached to the chamber sides. With the higher density gradient, a different flow pattern was observed, particularly in the chamber exit region. In this region the backflow existed on the top as well as the bottom of the chamber. The flow in this region was slightly turbulent. In both cases it was observed that at the beginning of the chamber the stagnation region existed and contained one or more vortices (always an odd number).

To avoid the air motion within the chamber, later experiments were conducted with a paper diaphragm placed across the exit of the chamber as well as at the opening in the outside wall. This effectively stopped the motion and, as surprising as it seems, did lead to more reproducible experimental results.

A second modification arose from the fact that the preparation of the chamber (cleaning, loading, etc.) and other procedures for a run required an average of 30 to 45 minutes. In the cases where some of the needles were clogged or damaged, this time was increased two- or three-fold. In order to shorten

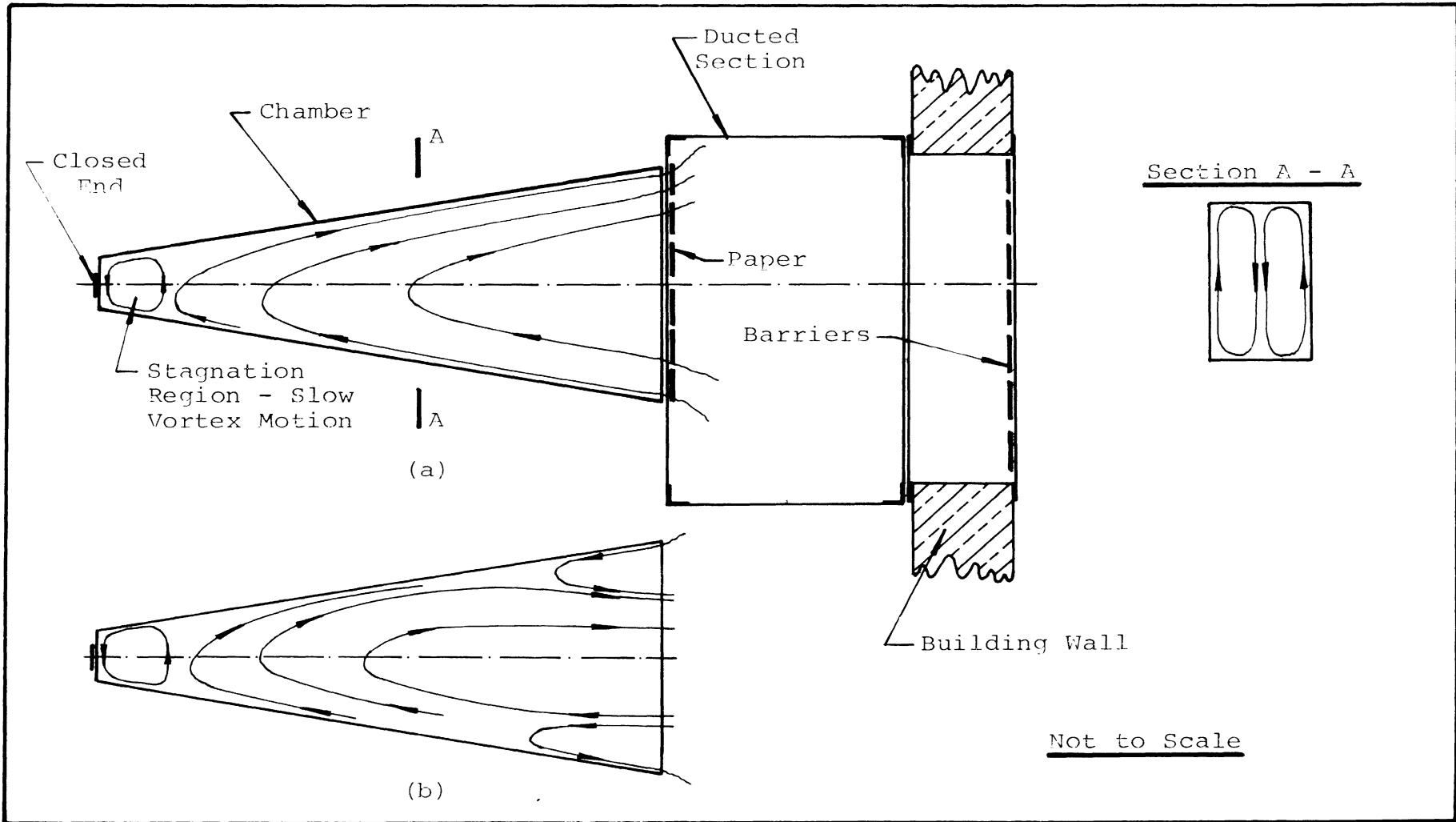


Figure 1. Air Flow Patterns in the Chamber
(a) Attached Flow, (b) Detached Flow

that time, the needle assembly design was changed as shown in Figure 2. The new design allowed a clogged needle to be cleaned with a thin stainless steel wire without having to remove it from the chamber. In those cases where damage of a needle occurred, the replacement of the damaged tube (always the smallest one) was now easy and fast.

The most frequently occurring damage to the needle tip is shown in Figure 3. Figure 3a shows a good needle assembly, while in cases (b) and (c) the needle tip was bent by flying debris from the initiator charge. Case (d) shows the damage which appeared during negligent cleaning. The type of damage of cases (b), (c), and (d) usually caused the fuel jet to exit at an angle, thus causing wetting of the side walls or interference with other fuel jets. In case (e) the debris chopped off the needle tip and completely stopped the fuel flow. The last example, (f), shows debris attached to the needle tip. This caused a slight bending of the tip and created the possibility of wall wetting. These damage patterns, except case (d), usually occurred at small radius in the chamber.

There are still some operational problems which, if solved, could probably improve the experimental results. The following problems are considered to be the most important.

1. A fuel spray was observed in the lower half of the extended part of the chamber. The main cause of this spray was the breaking up of the monodisperse drops. This was attributed to the greater height of the extended part of the chamber and the initial inclination (10° , with respect to vertical axis)

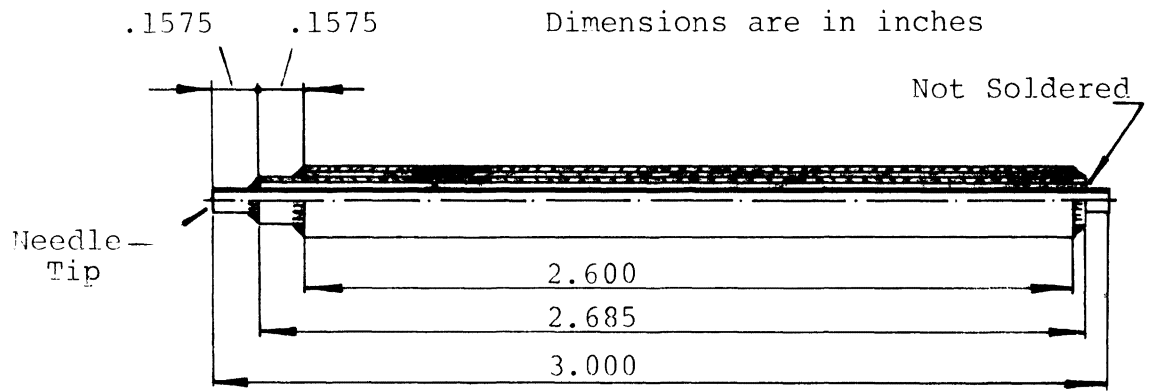


Figure 2. Needle Assembly - Final Design

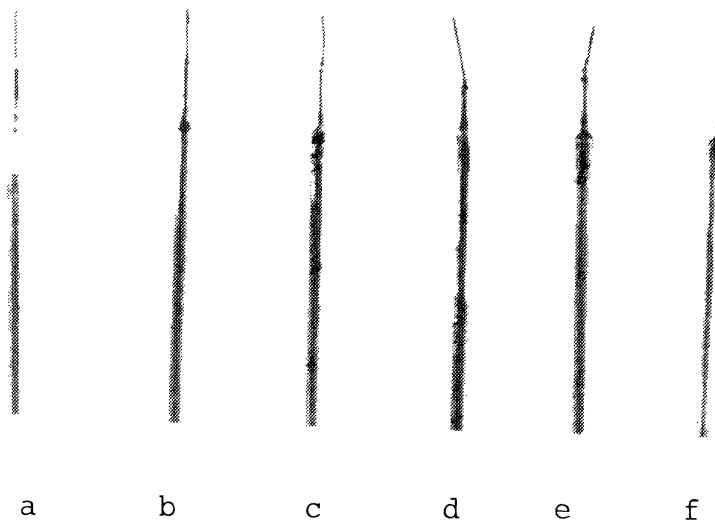


Figure 3. Damage of the Needle Tip

of the protruding fuel jets from the needles. The spread of this spray measured as much as 1 1/2 inches at the bottom of the chamber. At the same time the spreading in the original part was generally below one-half inch. These measurements were verified outside the chamber as well as inside.

2. Due to the thickness of the fuel pad (approximately 1 1/2 inches) during retraction, the fuel jets were disturbed. The motion of the fuel pad caused the displacement of the fuel jets or spray, leaving a region of air only. Since the time between fuel pad retraction and occurrence of the explosion was only 0.35 second, a minimal amount of fuel, if any, had a chance to fill that region. Thus, non-uniform fuel distribution occurred. This problem was more acute in the extended part of the chamber due to the greater height.
3. Wetting of the bottom of the chamber occurred in the interim between fuel pad retraction and wave front arrival time. This is considered to be a serious problem and should be investigated in future experiments.

C. WAVE FRONT SHAPE

The experimental results presented in the previous annual report⁽⁸⁾ indicated an unusual behavior in the trend of some radius versus time data. It has been found that this experimental data could be approximated, after the initial blast wave decay, by two straight lines, thus indicating two different detonation velocities. Also, it was found that the transition between these two detonation velocities usually occurred at a radial distance of around 40 inches. Many subsequent experiments have revealed this same effect when the initial blast energy levels were equal or greater than that derived from the blasting cap plus 2.0 grams of Detasheet. In considering this problem it was found that many known and unknown factors affect the experimental results. The most important factors follow:

1. Unequal conditions on the boundaries were considered to exist. For example, the bottom wall was completely wet due to the fuel build-up; along the top wall the tips of the needles were protruding into the chamber. The two side walls were presumably dry.
2. The breech conditions⁽⁸⁾ were considered to be an important factor. Also, there was an unsteady development of the starting process within the first portion of the chamber.

3. There was a non-uniform distribution of the fuel mass flow rate. It was found (see Figure 21 of Reference 8) that decrease in the fuel mass flow rates existed between rows 5-6, 8-10, 14-16, and 18-21.
4. Non-ideal cylindrical blast waves were formed^(8,9).

The effects of the above factors were not investigated individually. Rather, an investigation was undertaken of the wave front shape under these two detonation velocity conditions. The investigation was performed employing two different experimental techniques. First, a new arrangement of the pressure switches was employed. The new arrangement covered the three regions shown in Figure 4 (before, all pressure switches were located on the centerline on the side of the chamber). This arrangement allowed for experimental measurements on the bottom inclined wall of the chamber but, of course, it was not possible to mount pressure switches on the upper wall due to the needles. The total number of pressure switches was the same as before. The experimental results obtained are given in Figures 6 through 9, and they are discussed in more detail in the following section. Second, a schlieren system was set up and instantaneous photographs taken of the wave front at the chamber exit (before three-dimensional effects became large). Due to vibration problems, the schlieren system was converted to a shadowgraph system. Since the size of the chamber exit was larger (19 inches) than the diameter of the mirrors (12 inches), separate photographs of the lower and upper half of the exit were taken. The schematic

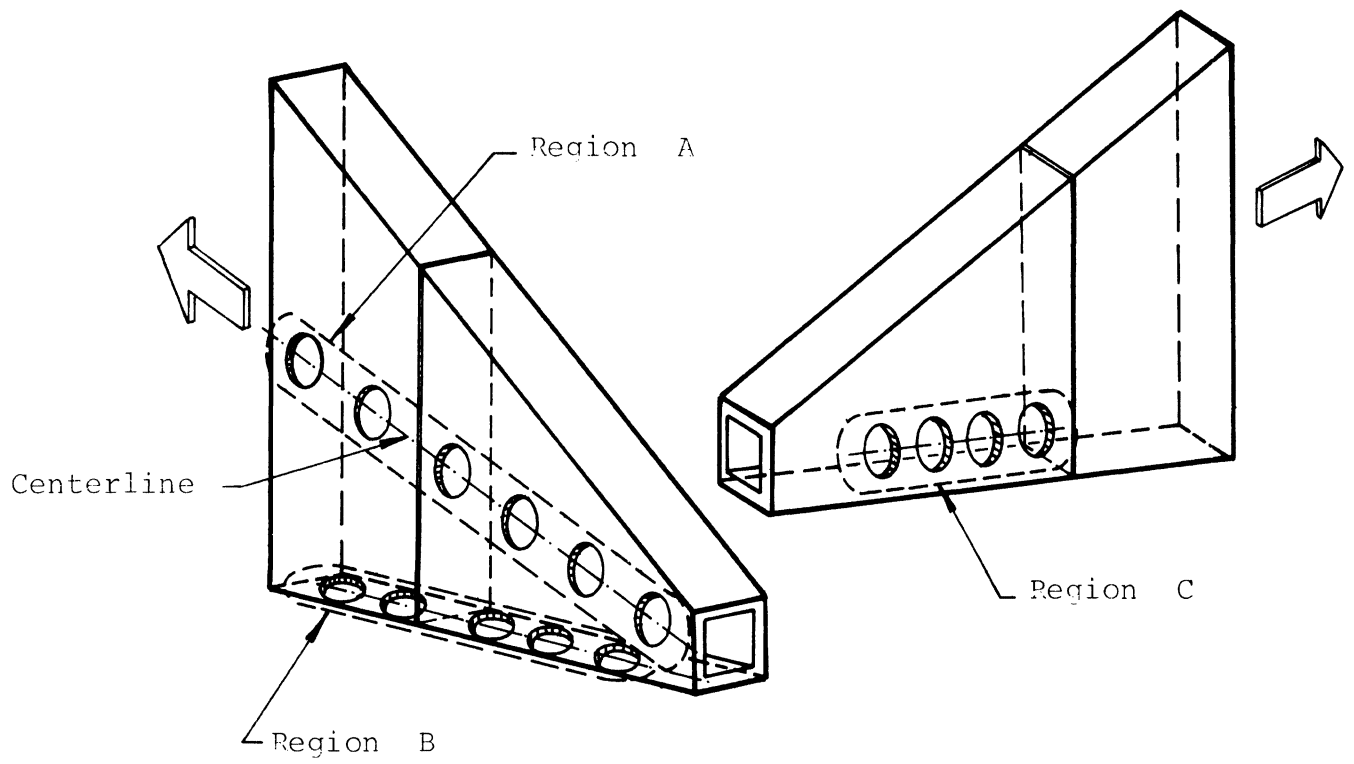


Figure 4. New Arrangement of the Pressure Switches

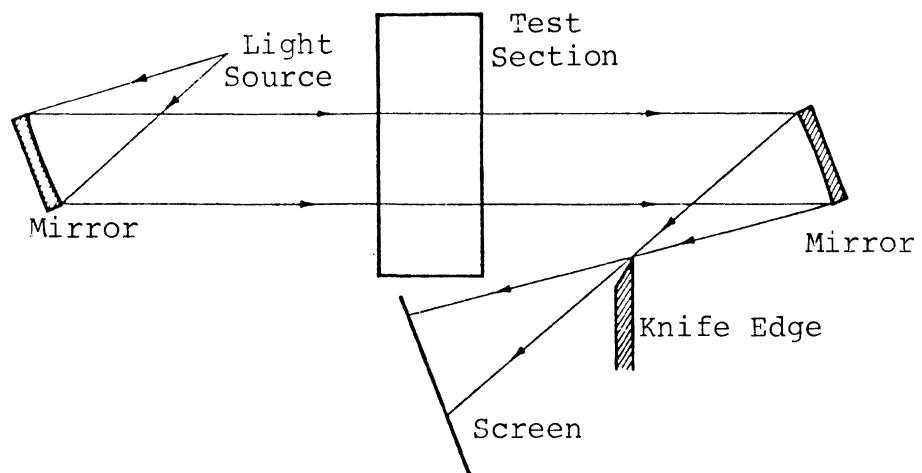


Figure 5. Schlieren System

arrangement of the schlieren system is shown in Figure 5. A spark light source with a duration of 80 to 100 nanoseconds was used. The schlieren and shadowgraph pictures obtained are given in Figures 10 to 14 and are discussed in more detail in the following section.

EXPERIMENTAL RESULTS AND DISCUSSION

Pressure Switch Data

The experimental data were collected from the three different regions, A, B, and C as sketched in Figure 4. In region A the pressure switches were placed on the center-line along the side of the chamber. In region B the switches were on the bottom of the chamber. Region C is within the original part of the chamber only. Here the pressure switches were placed along the side at a height of one inch above the bottom of the chamber.

The blast energy levels that were used were E-106 plus 1.75 and 3.0 grams of Detasheet. These energy levels were chosen so that it would be possible to observe the effect of low as well as high initial energies on the wave front development. In particular, the low energy was selected to see whether it was above or below the threshold energy. Earlier experiments performed in the extended chamber with 1.5 grams did not result in detonation. On the other hand, experiments done in the original chamber with 1.5 grams did produce detonation. With this new arrangement of the pressure switches, experiments with blast waves and heterogeneous detonation waves were performed.

For the blast wave case (air only in the chamber), the experimental results in the different regions are shown in Figures 6 and 7 with the initial energy levels of E-106 plus 1.75 and 3.0 grams, respectively. The averaged results, calculated from four runs for the 1.75 gram case and six runs for the 3.0 gram case, are shown in Figures 6c and 7c, respectively. The results in regions A, B, and C show that significant differences were not observed in the radius versus time data. The scatter of the results was small (below 5 percent) for all regions. For the most part, it appears that the wave front velocity in the middle of the chamber was slightly higher than the velocities at either the bottom of the chamber or one inch above the bottom. However, in the further development of the wave front (larger radius), the velocity at the bottom of the chamber exceeded that in the middle. This is shown in Figures 6c and 7c. This phenomena was observed during most of the runs and could not be explained. It is of interest to note that this change in velocity appeared around the radial position of 40 inches for both of the initial energies used.

The heterogeneous, kerosene and air, experimental results for regions A, B, and C are shown in Figures 8 and 9. Using the experimental data from nine runs (for 1.75 grams) and eight runs (for 3.0 grams), the averaged heterogeneous results were obtained and are shown in Figures 8c and 9c. These experimental results showed that the development of a wave front in the regions A, B, and C was different. Also, it was found that the pattern of development of a wave

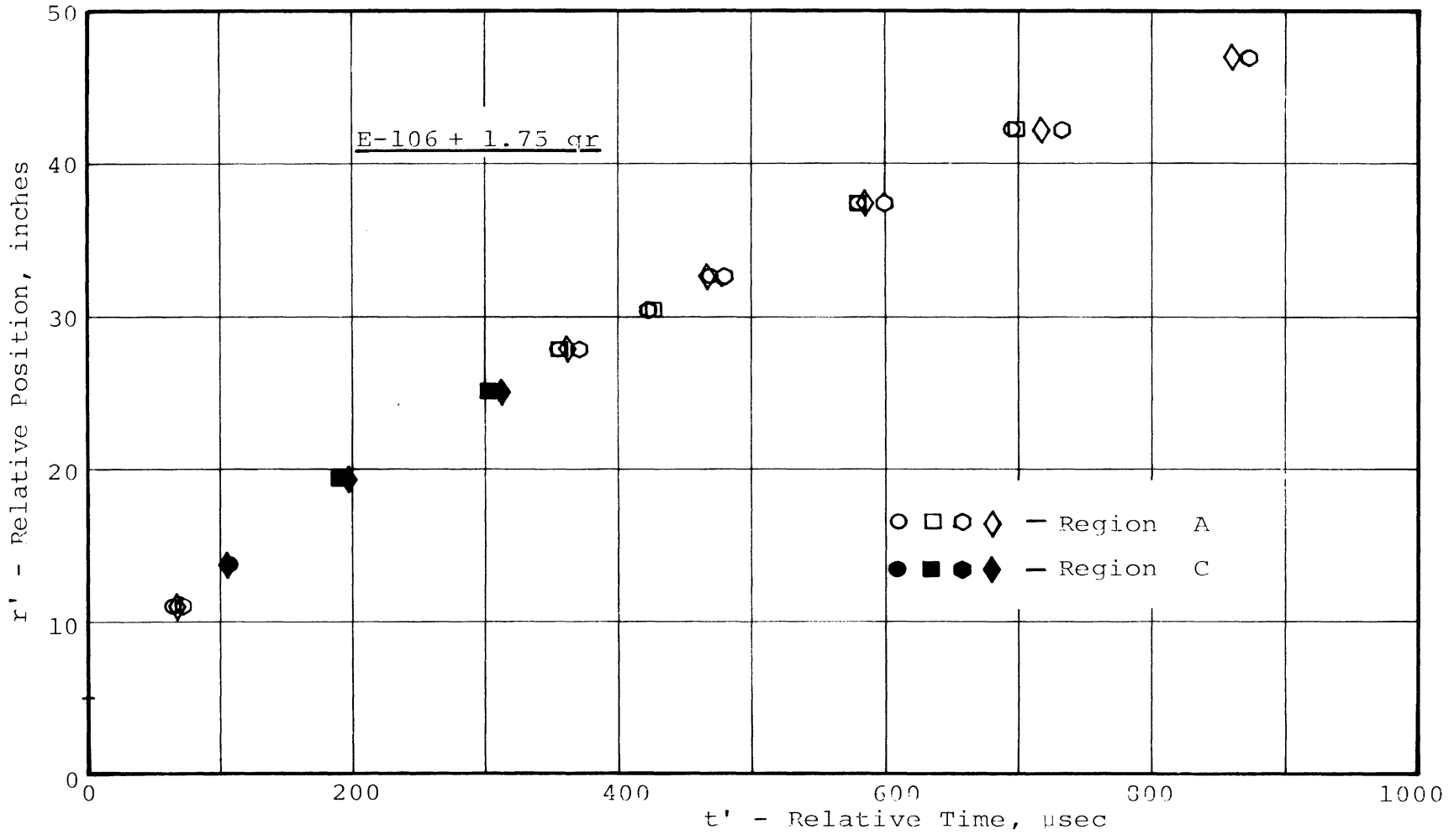


Figure 6a. Experimental Blast Wave Data, r' Versus t',
Regions A and C

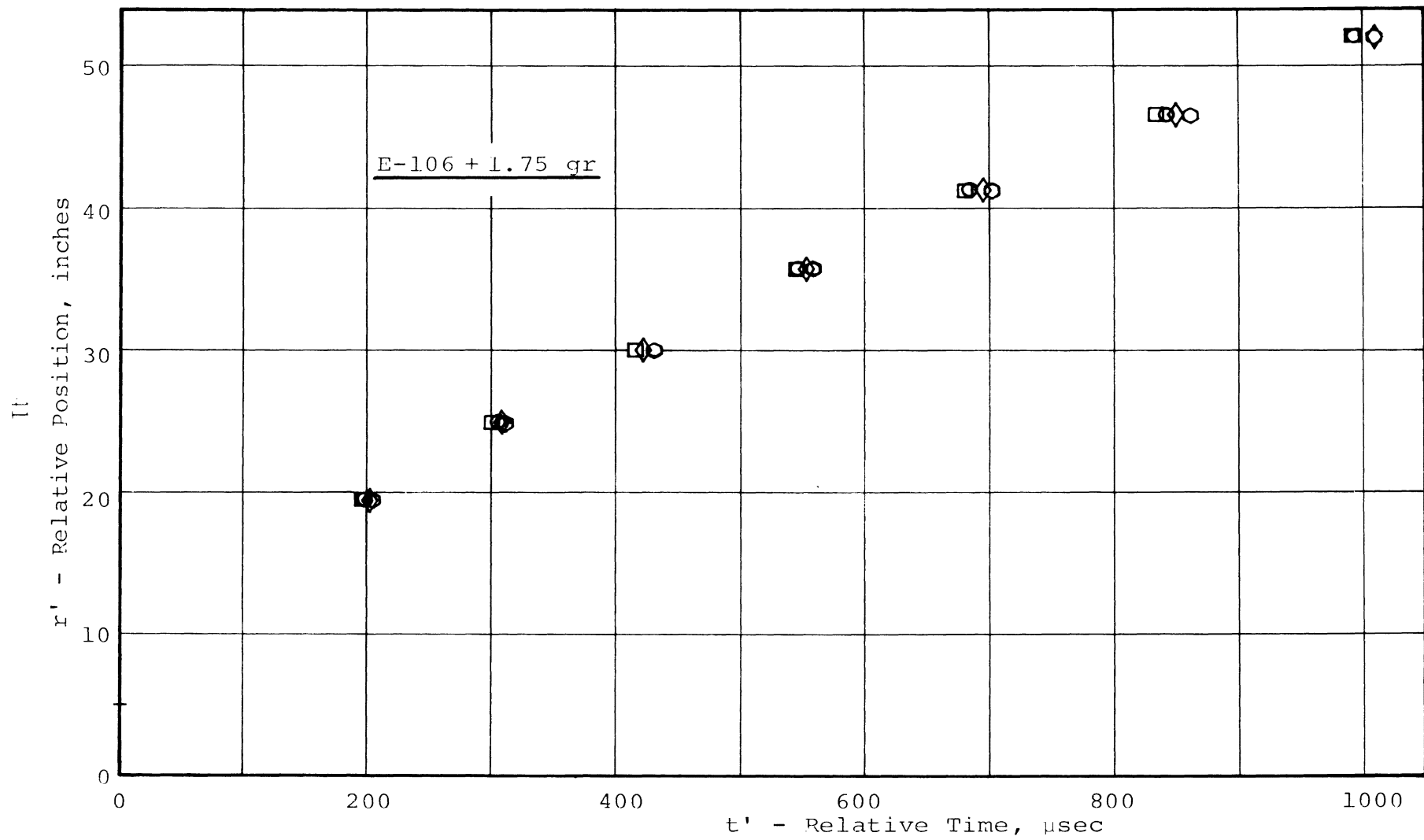


Figure 6b. Experimental Blast Wave Data, r' Versus t' ,
Region B

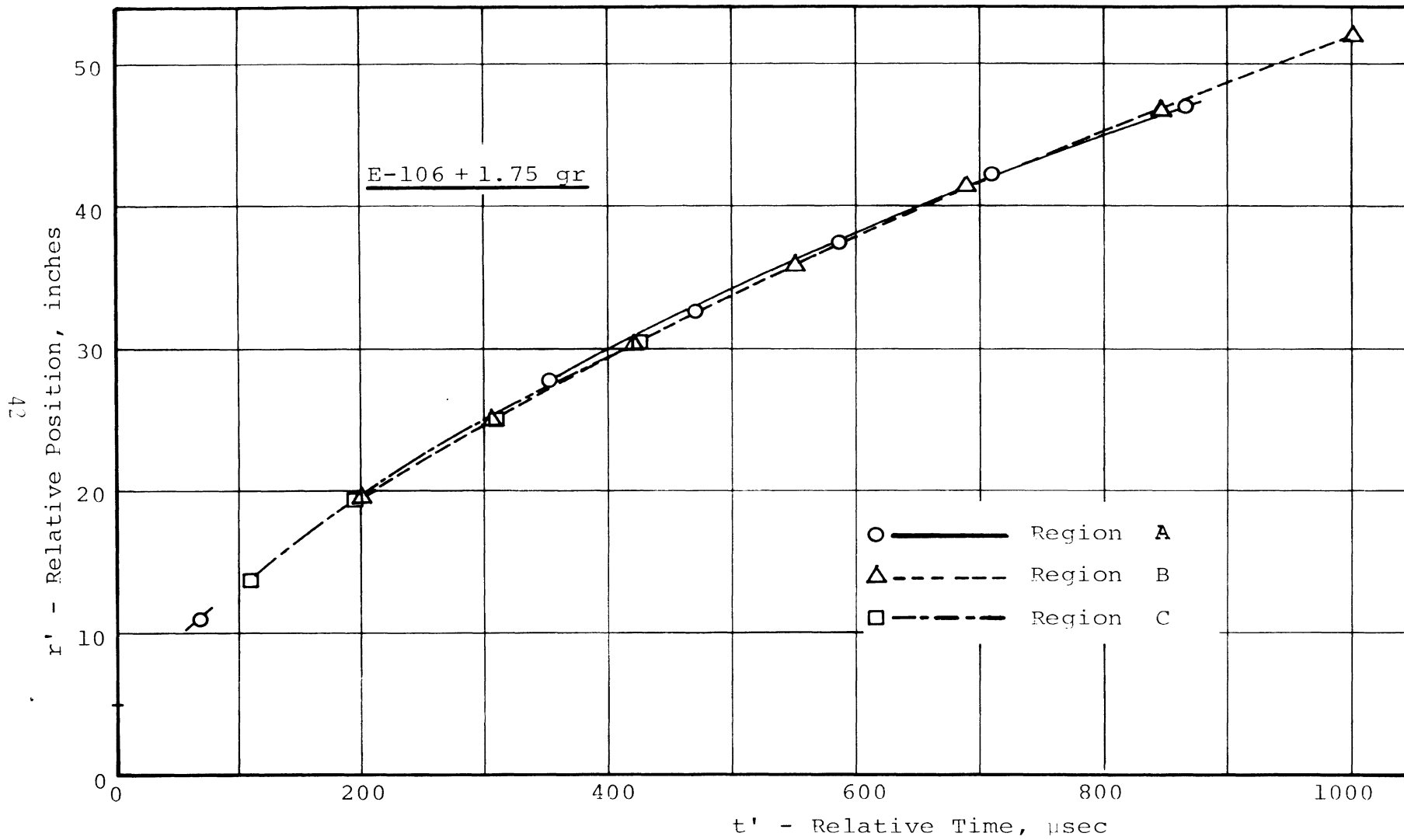


Figure 6c. Averaged Blast Wave Data, r' versus t'

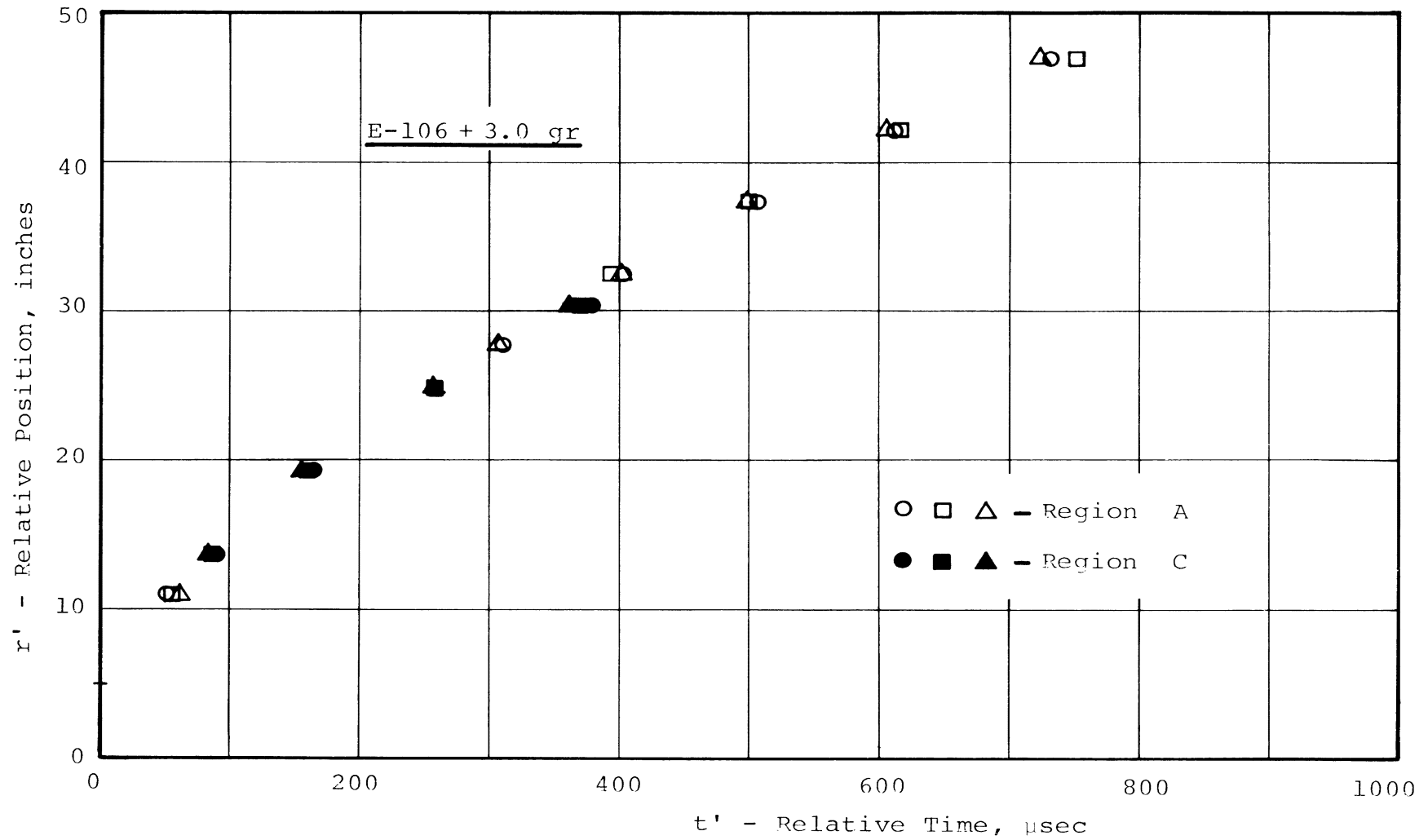


Figure 7a. Experimental Blast Wave Data, r' Versus t' ,
Regions A and C

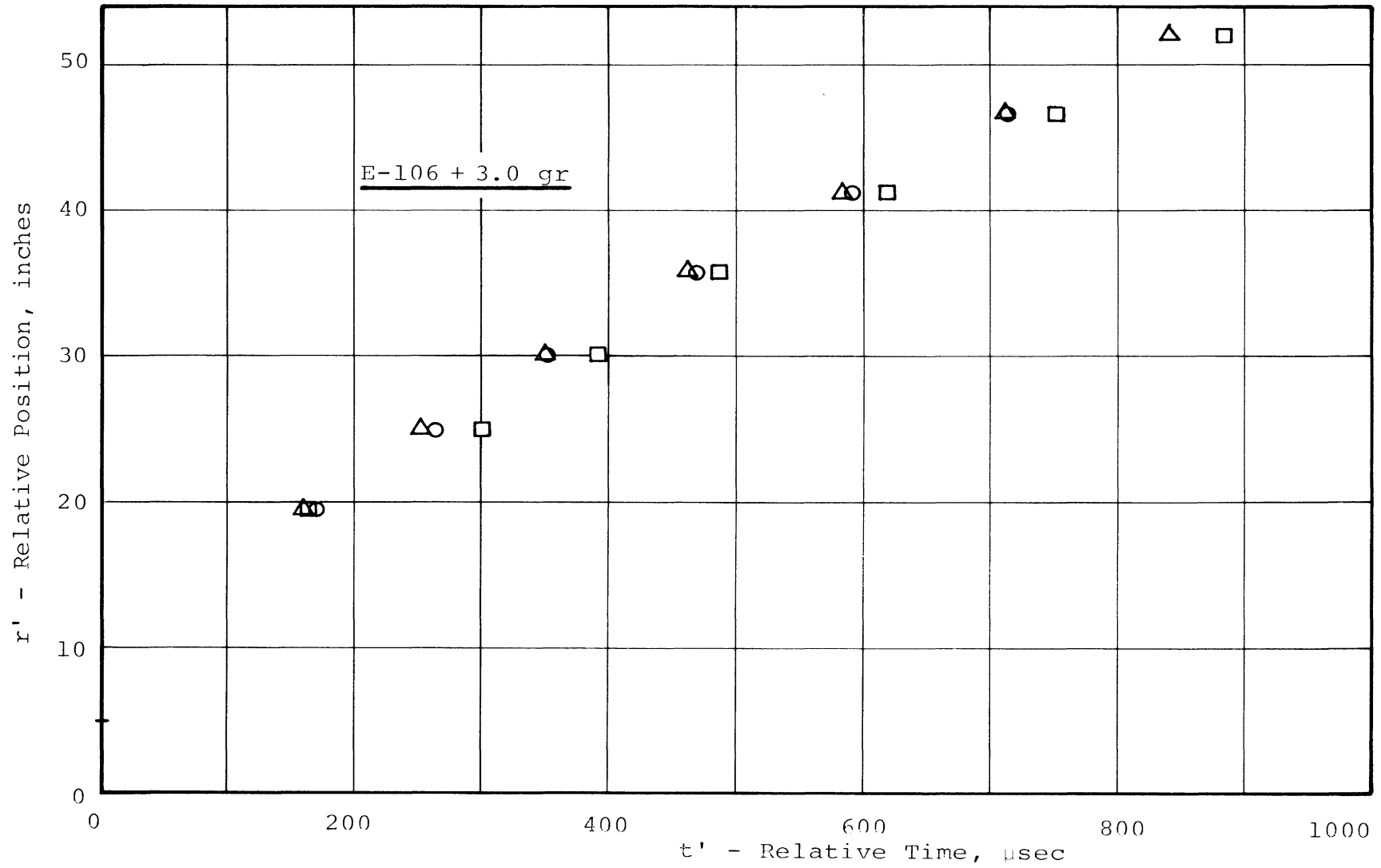
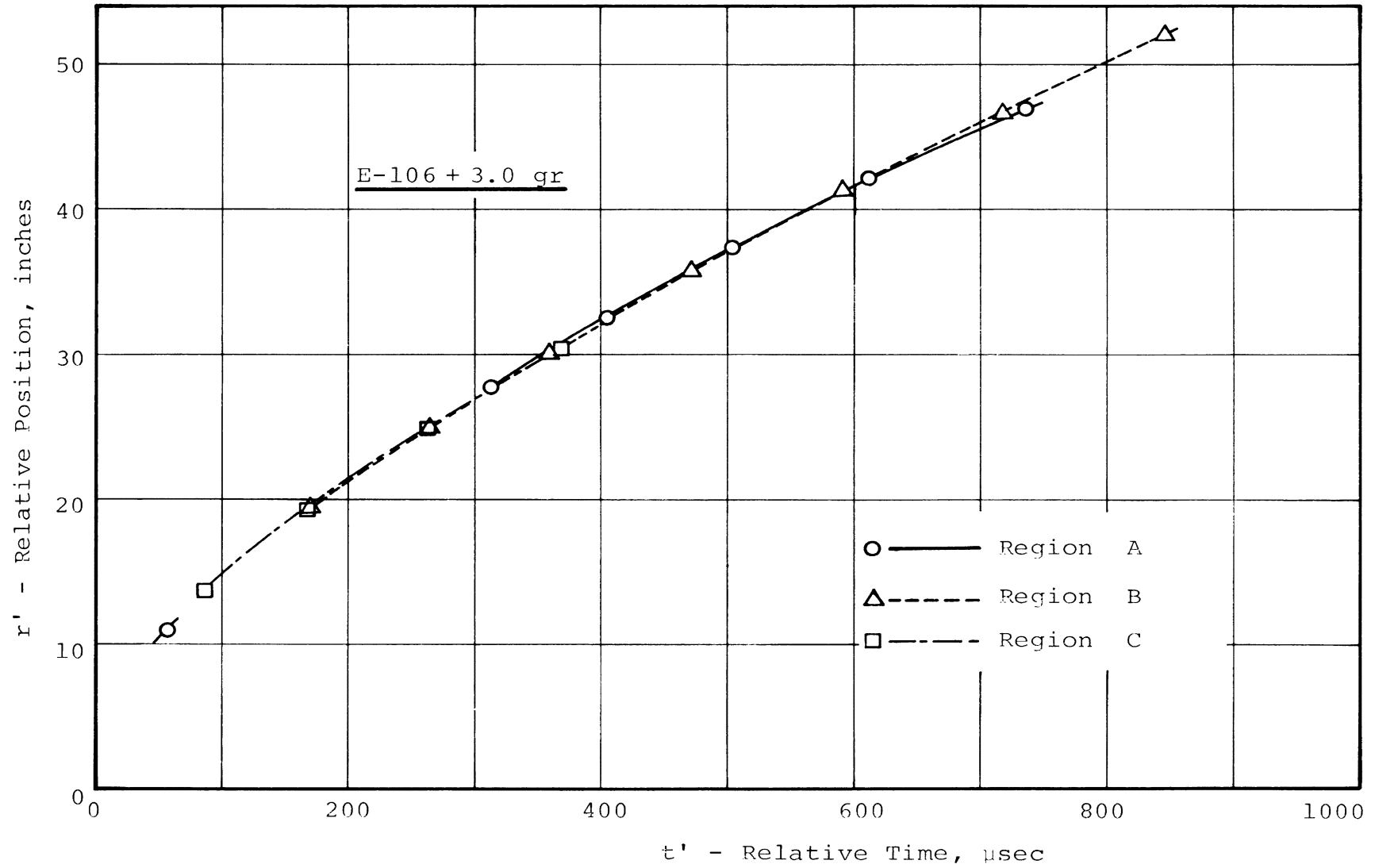


Figure 7b. Experimental Blast Wave Data, r' Versus t' , Region B

Figure 7c. Averaged Blast Wave Data, r' Versus t'

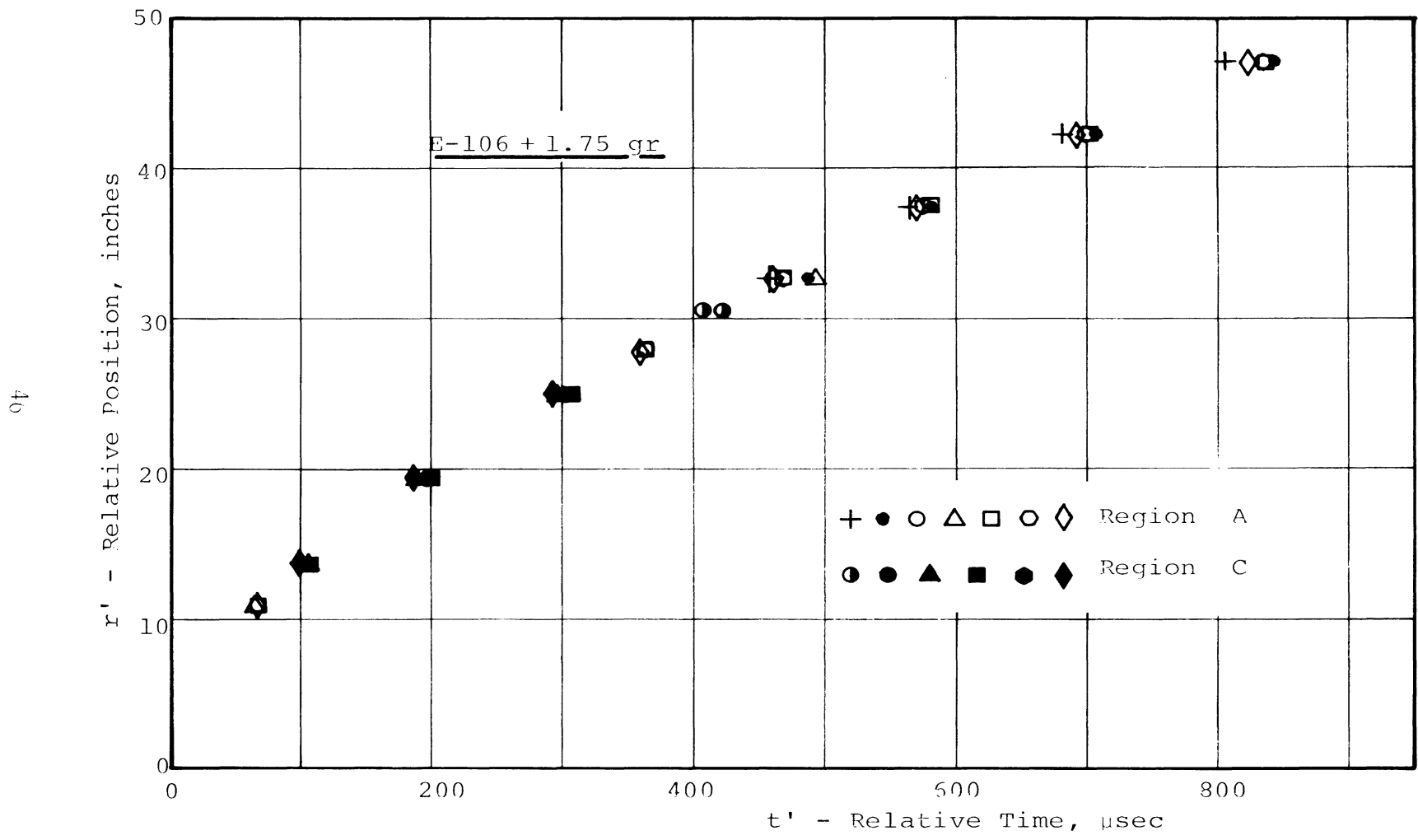


Figure 8a. Experimental Heterogeneous Data, r' Versus t',
Regions A and C

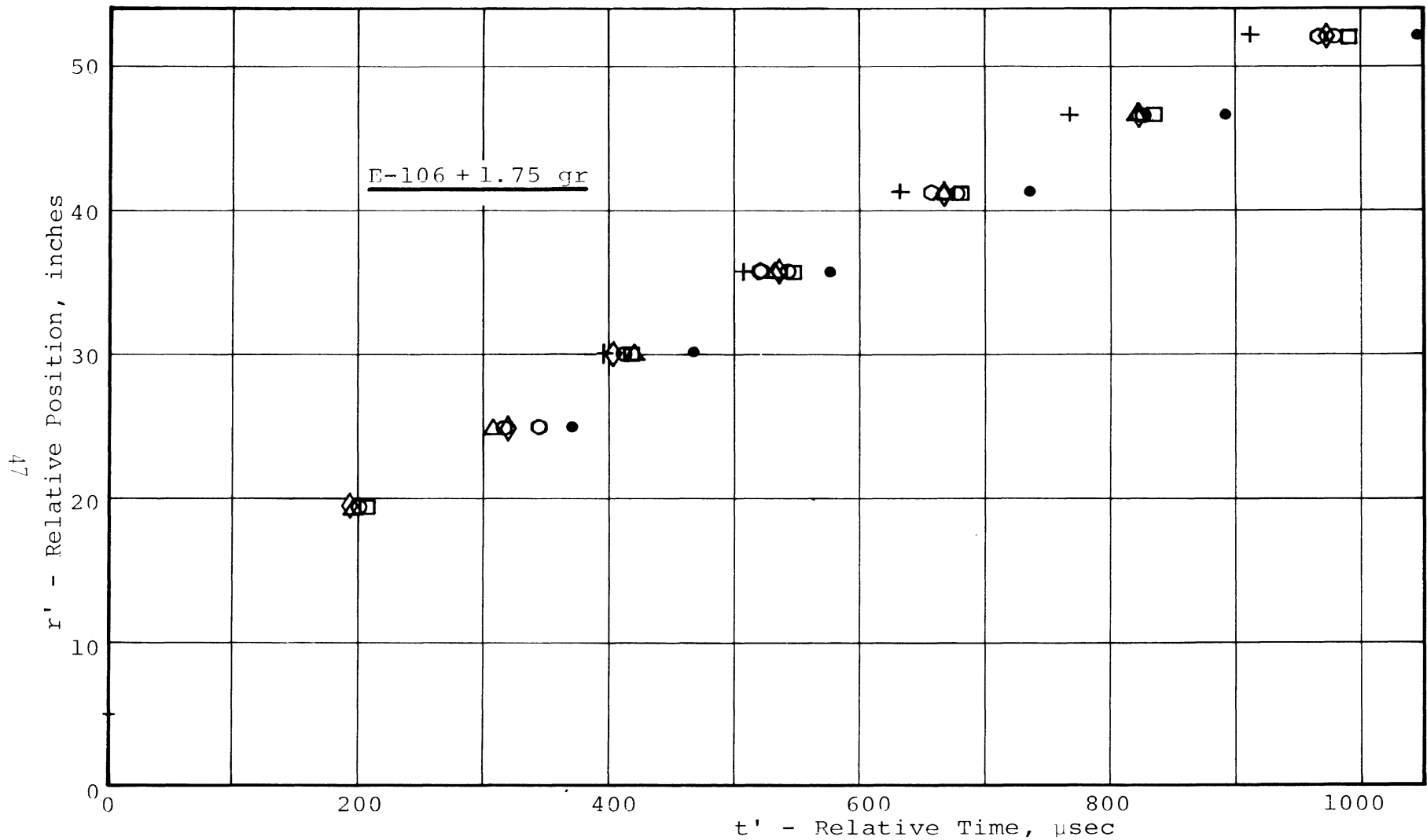
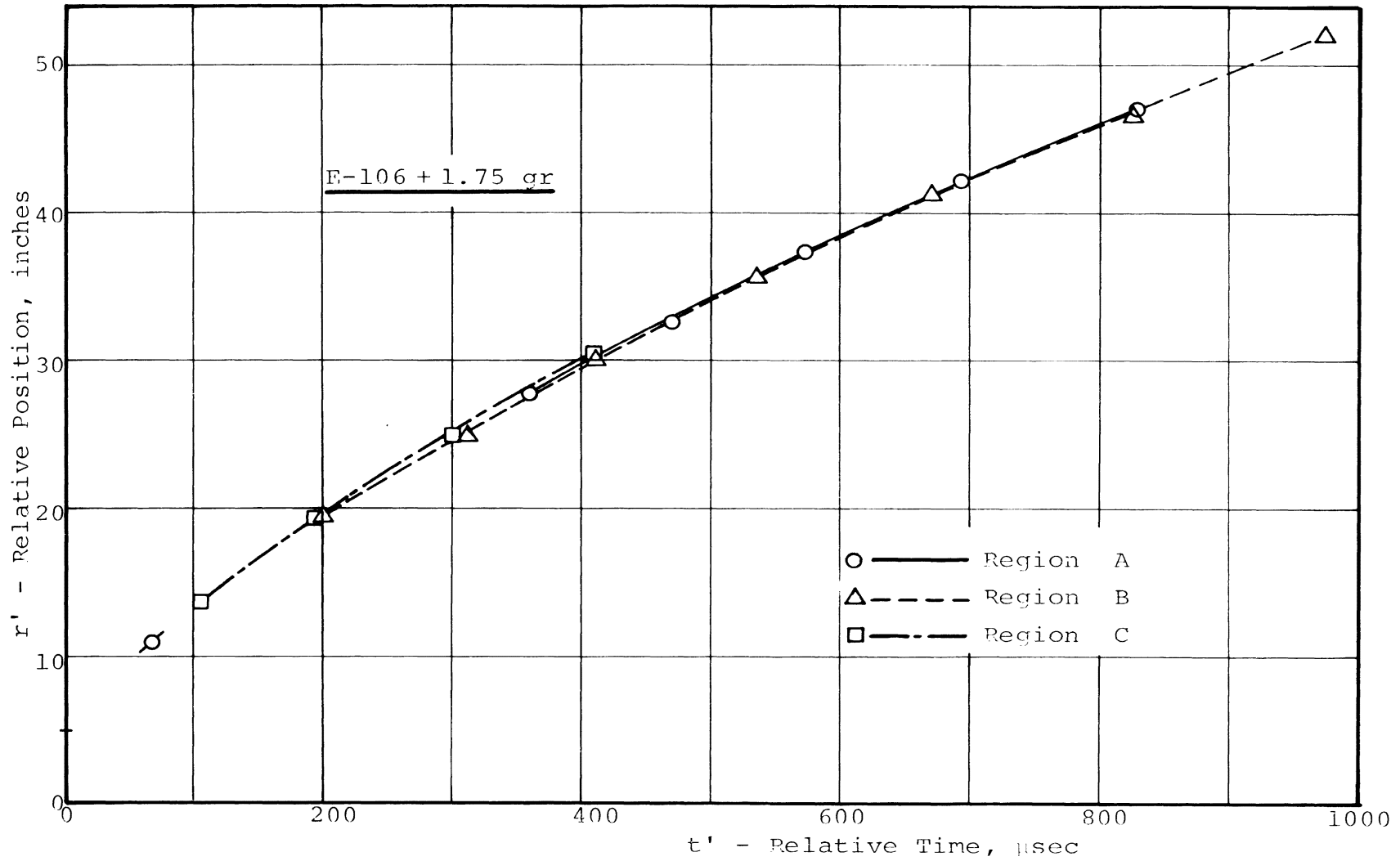


Figure 8b. Experimental Heterogeneous Data, r' versus t' , Region B

Figure 8c. Averaged Heterogeneous Data, r' Versus t'

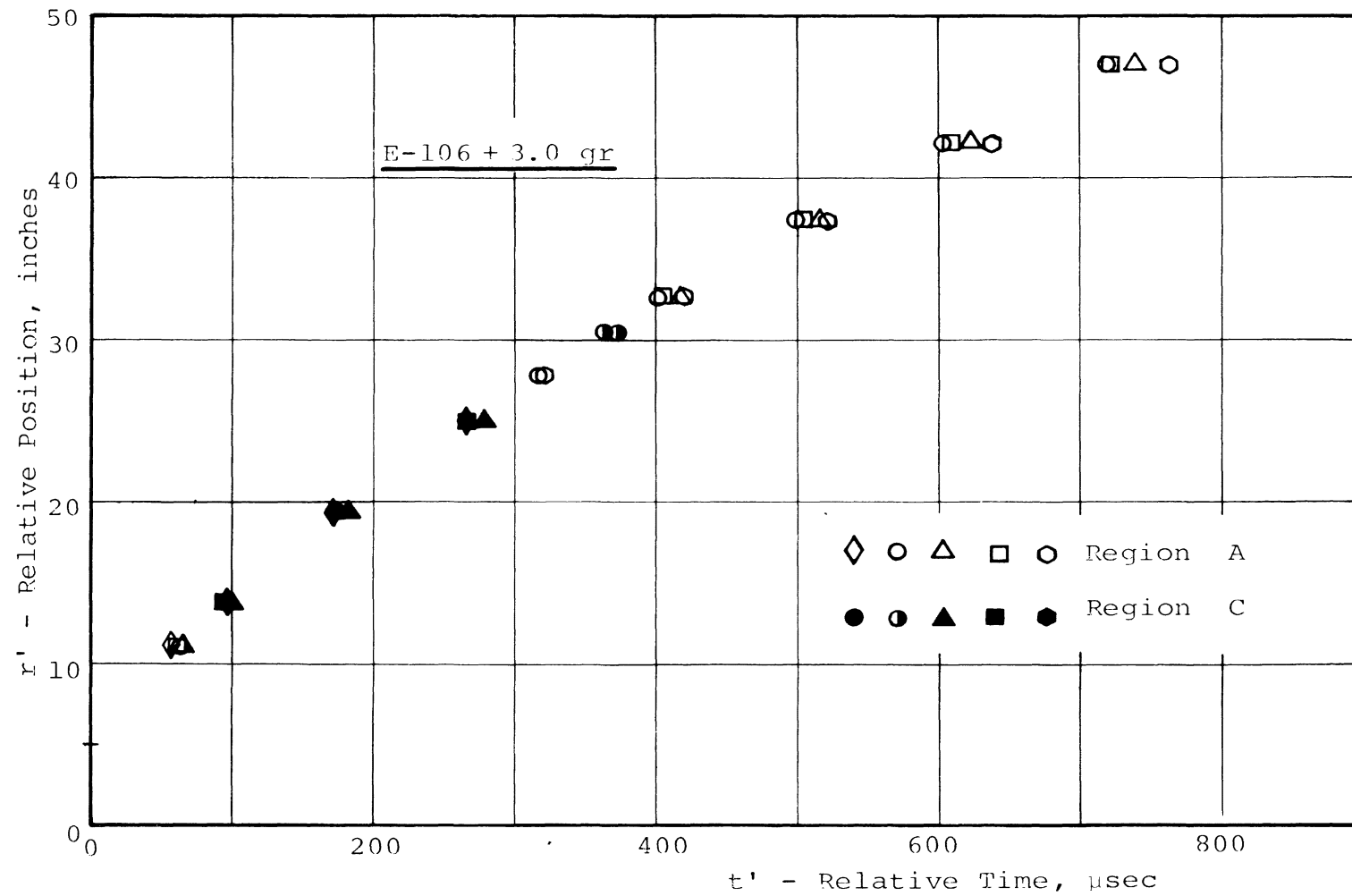


Figure 9a. Experimental Heterogeneous Data, r' Versus t' ,
Regions A and C

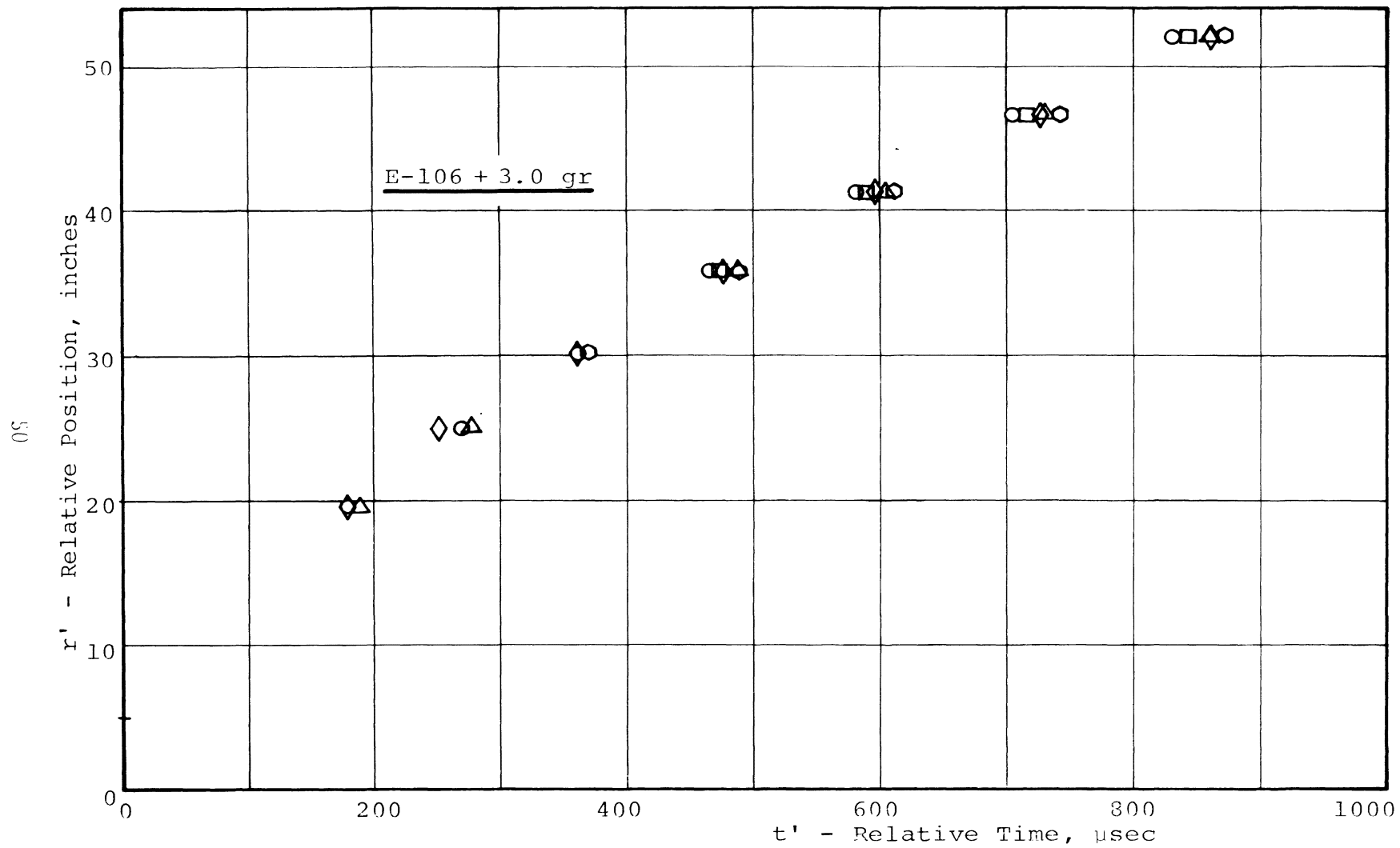


Figure 9b. Experimental Heterogeneous Data, r' Versus t' , Region B

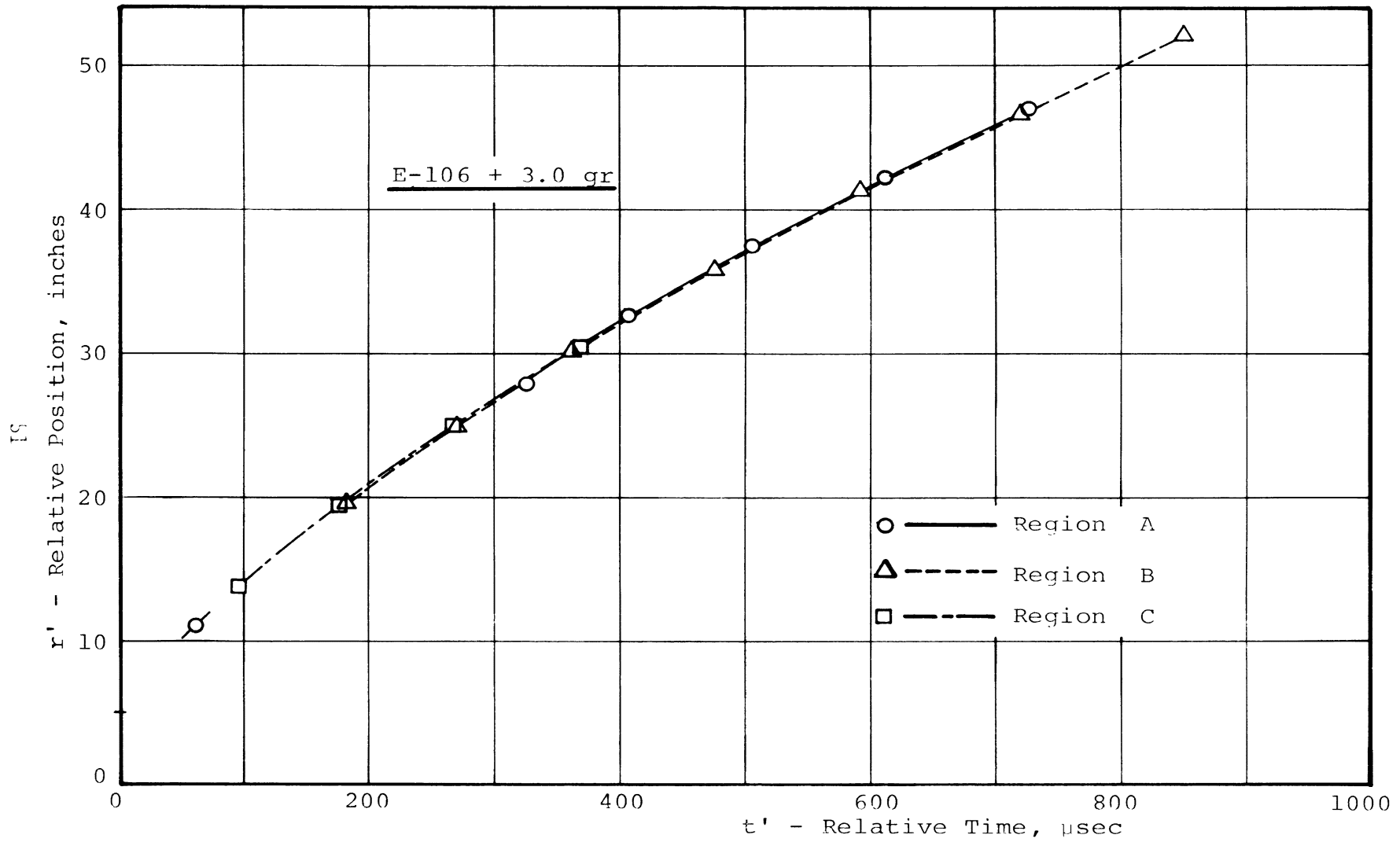


Figure 9c. Averaged Heterogeneous Data, r' versus t'

front in these regions strongly depended on the initial blast energy levels. The scatter of the experimental results was substantially higher (up to 18 percent) than in the case of a blast wave. Therefore, it is necessary to analyze and discuss the above cases separately.

For a low initial energy level (1.75 grams) the experimental results showed that in region B a large scatter in the data (up to 18 percent) existed. The trend of the radius versus time data varied, but for most runs the results showed that a detonation velocity was reached. The detonation velocity was usually achieved at the radial positions of approximately 38 to 42 inches. At the same time, the experimental results in regions A and C showed more consistency. The scatter of the results was much smaller (up to 8 percent) and the trend in radius versus time curves showed monotonic decay along the chamber. A detonation velocity in region A was only rarely reached. The trends of the averaged radius versus time curves were similar for the three regions A, B and C. The velocity in the middle of the chamber was slightly higher than at the bottom. But at the bottom of the chamber a detonation velocity was obtained at a radius of approximately 40 inches. The experimental as well as averaged results showed that the velocity in region C was slightly higher than that reached in the regions A and B. The reason for this phenomena was not investigated and at this moment is unknown.

For most of the high initial energy levels (3.0 grams) the experimental data in regions A and B showed that an initial decay of a blast wave was followed by two distinct heterogeneous detonation velocities. The transition between the decay of a blast wave and the two distinct detonation velocities occurred approximately at the radii of 28 and 40 inches, respectively. The scatter of the experimental results in all of the regions did not exceed 10 percent. The highest scatter was observed in region A. The averaged velocity in region A was slightly higher than that in Region B, but it showed either monotonic decay or two detonation velocity behavior along the chamber. On the other hand, the velocity in region B initially decayed and was later followed by a heterogeneous detonation. The transition in B region usually occurred at the radius of 40 inches. Velocity in region C was approximately equal to that reached in region A.

From the experiments it was found that the shape of the wave front (blast wave as well as detonation) closely approximated the ideal cylindrical shape. The greatest differences between the ideal cylindrical shape and the real wave front existed at the beginning of the chamber. This was probably caused by the non-ideal blast wave development and was also effected by the distorted breech cavity. Also, it was shown that for either the low or high energy levels a heterogeneous detonation at the bottom of the chamber was reached. This was probably caused by the existence of a fuel layer on the bottom wall of the chamber.

Photographic Studies

The results presented in the foregoing section establish the shape of the wave front only in the lower half of the chamber. The shape of the wave front in the upper half of the chamber could not be established in this way. Thus, it was of interest to obtain schlieren or shadowgraph photographs of the wave front at the chamber exit. Hopefully, the photographs would reveal any abnormalities which would then help to better understand wave front propagation. In practice it was difficult to obtain a picture at the exact instant when the wave front emerged from the chamber exit. Even a slight change in the wave front development caused the wave front to appear far out of the chamber exit or still in the chamber itself. Blast and heterogeneous wave fronts were photographically studied and the initial blast energy levels used were the same as that presented in the previous part of this section.

Blast Wave Front Photographs

Photographs of the blast wave (at the high and low energy levels) emerging from the chamber and its further development are shown in Figures 10 and 11. The top and bottom of the wave front at the chamber exit are presented in separate photographs. Each photograph has a label showing the number of the run and the time delay (which was measured from the pressure switch No. 17) as well as an arrow showing the centerline of the chamber. The ideal cylindrical wave drawn on the photographs is shown as a chopped line right at the exit, and its corresponding position to the actual (real) wave front is shown as a dotted line.

Run #179, 125 μ s



Top of the Chamber (TC)

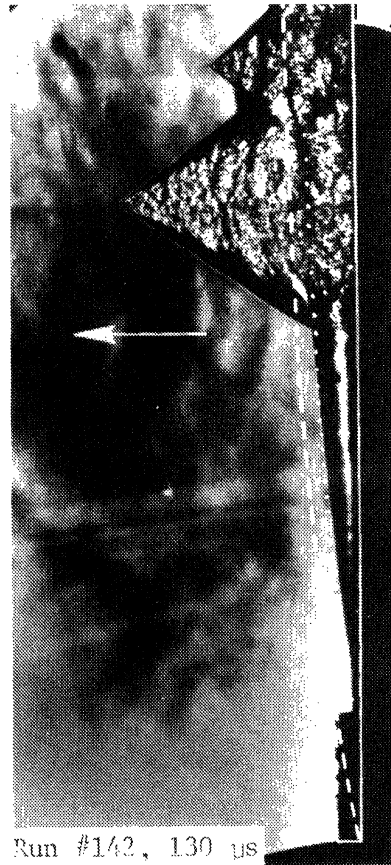
Wave Motion (WM)

Centerline of the Chamber (CLC)

Wave Motion (WM)



Run #130, 160 μ s



Run #142, 130 μ s

Bottom of the Chamber (BC)

Figure 10. Photographs of Blast Wave Front at the Chamber Exit, E-106 + 1.75 grams

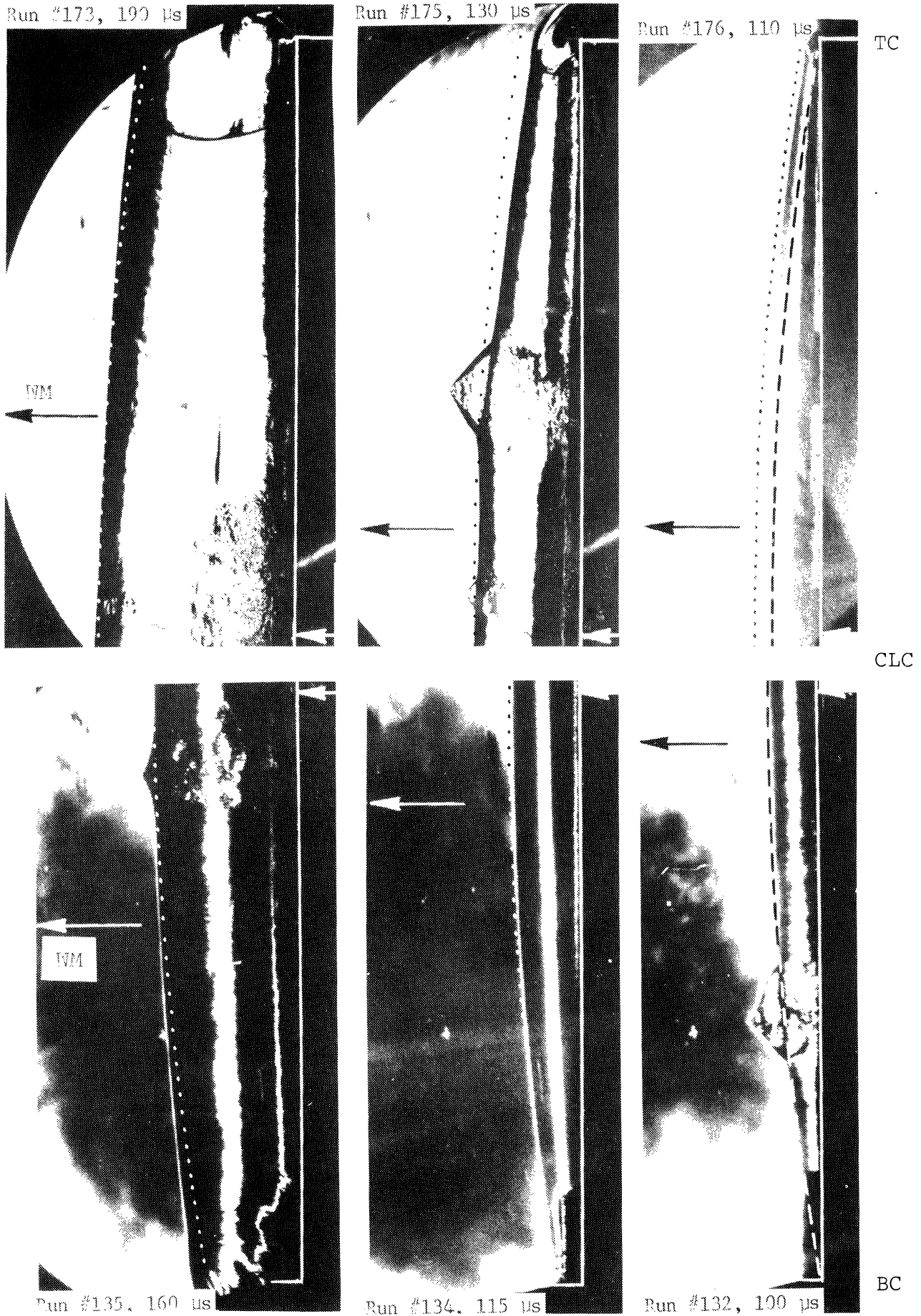
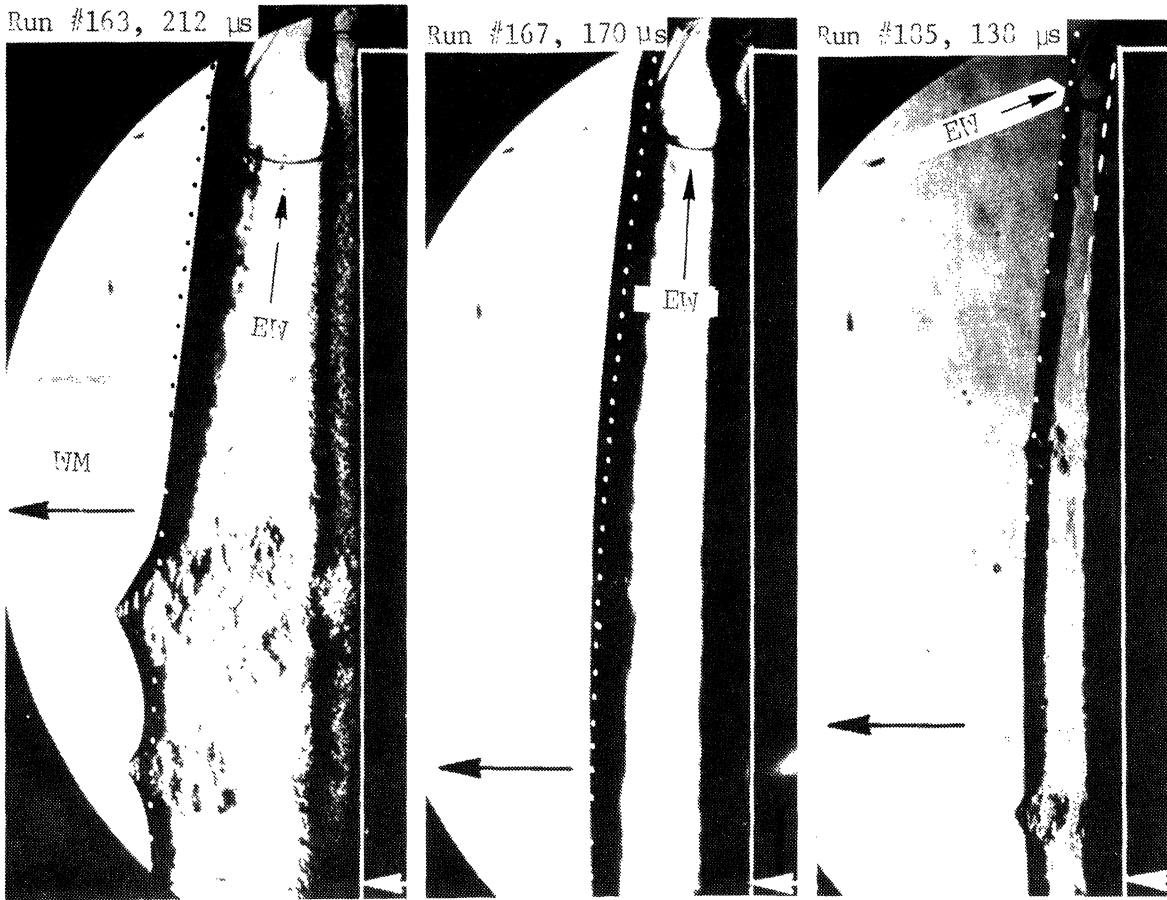


Figure 11. Photographs of Blast Wave Front at the Chamber Exit E-106 + 3.0 grams

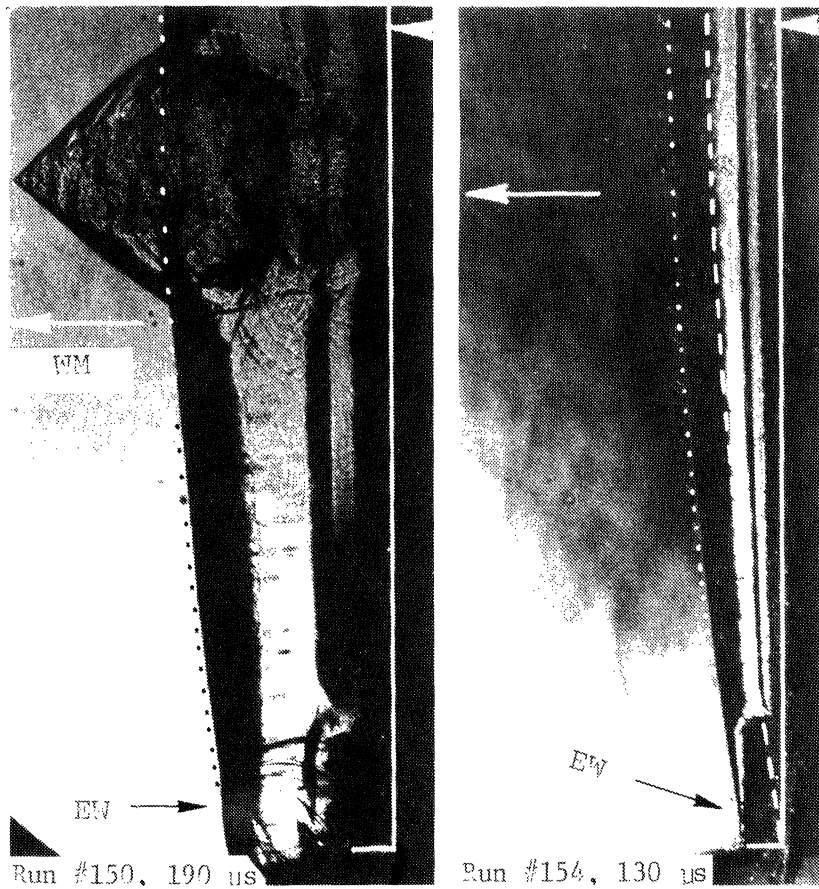
It can be seen that a real wave front differs only slightly from the ideal. This verified the data presented previously in this section. The most prominent distortions of the wave front were due to solid debris which probably came from the blasting cap. This debris was traveling supersonically and, hence, there are conical bow shock waves attached to the debris. With a low initial energy, irregularities of the wave front were observed more often than when a high initial energy was used. These irregularities (caused by the debris overtaking the wave front) might be a partial explanation for the scatter in the radius versus time results. It is now believed that the scatter in the data points may be due primarily to either the premature triggering of the pressure switches by the bow shock attached to the debris, or by the impact of the debris itself.

Heterogeneous Wave Front Photographs

The photographs of a heterogeneous wave front emerging from the chamber exit are shown in Figures 12 and 13. As was mentioned before, it was almost impossible to time the photograph to perfectly coincide with the emergence of the wave front. Only once was a wave front successfully photographed right at the exit (run No. 155). As before, the ideal cylindrical shape is drawn on the photographs and shows that the discrepancies between the actual wave front and the ideal were small. These discrepancies were larger than those observed in the cases of a blast wave front. To photograph a wave front in the upper half of the chamber exit, the necessary time delay was larger than that for the lower half of the chamber exit. This might indicate that a wave front in



CLC



BC

Figure 12. Photographs of Heterogeneous Wave Front at the Chamber Exit, E-106 + 1.75 grams

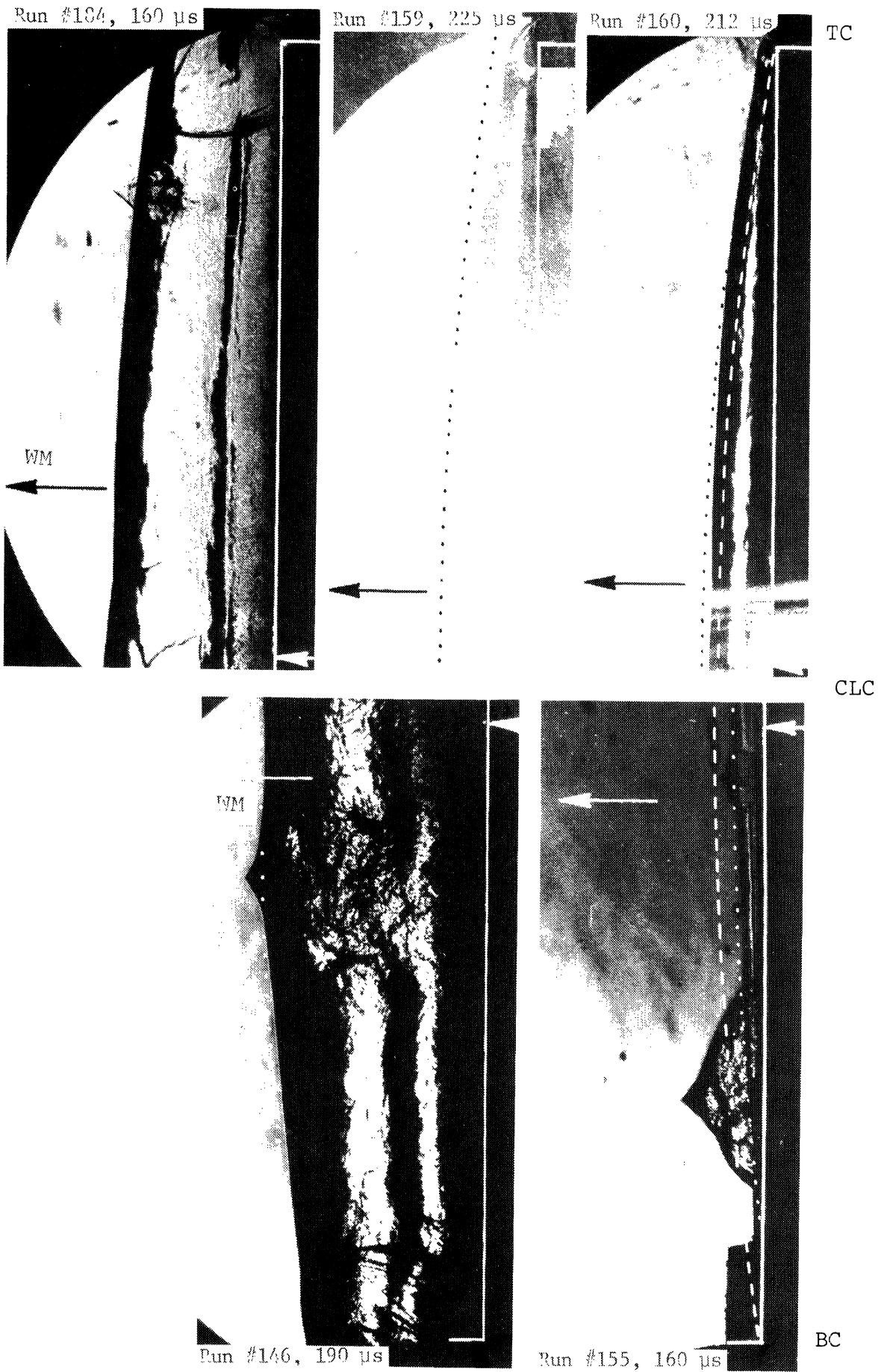


Figure 13. Photographs of Heterogeneous Wave Front at the Chamber Exit, E-106 + 3.0 grams

the upper half was slower than that in the lower half. This slower motion of a wave front was probably due to the presence of the needle cavities in the top wall, the protruding needle tips into the convective flow, and the presence of unbroken fuel jets in the vicinity of the needle tips. As in the cases of a blast wave front, the existence of debris in front of the heterogeneous wave front was observed. The bow shocks attached to the debris also distorted the shape of the wave front. Run-to-run reproducibility of a wave front shape was good except when either a great amount or large debris occurred. The propagation of a wave front outside of the chamber was always followed by two expansion waves. These expansion waves originated at the top and bottom of the exit and are visible in most of the photographs. In Figure 12 only, expansion waves (EW) are indicated by an arrow. The expansion waves promoted distortion of a wave front and also affected the convective flow behind it.

During the course of this photographic study, a number of peculiarities were detected. Among them the most interesting are shown in Figure 14. Because of the debris and the bow shock waves, the distortion of the wave front could be extremely large and could completely change the shape of the wave front, as shown in Figure 14, cases (a), (b), (c), and (d). Ordinarily a greater amount of debris was present when a low initial energy level was used. When these large distortions occurred, it was often found that some of the experimental data points were far from the average radius versus time curve. In Figure 14e

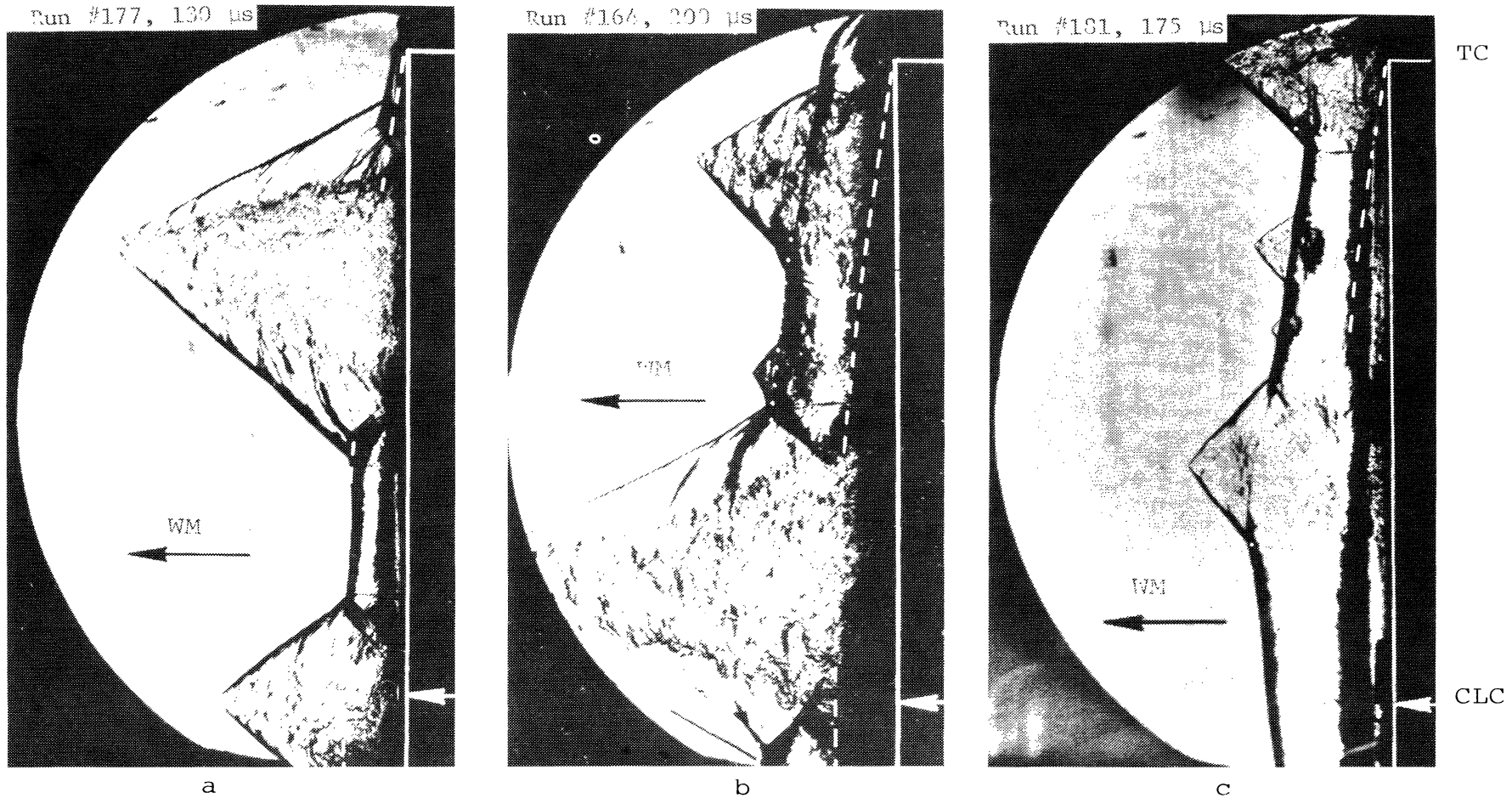
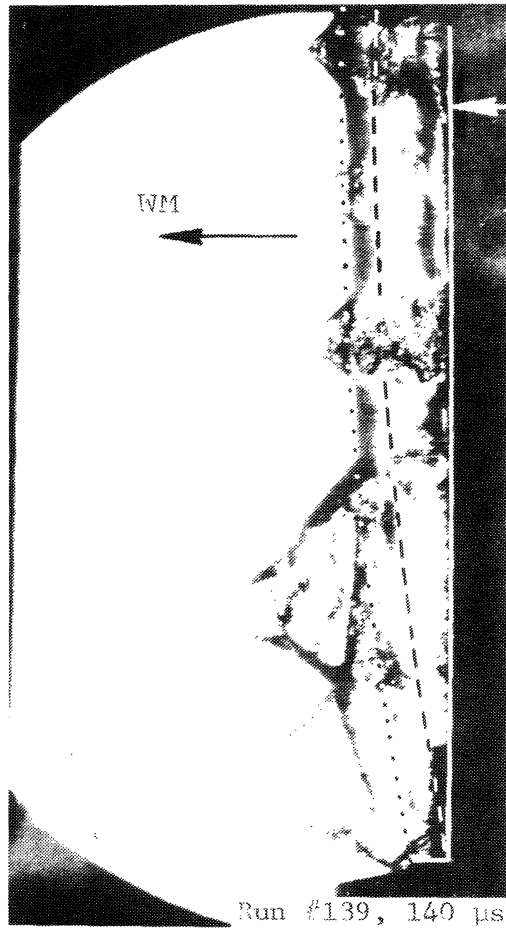
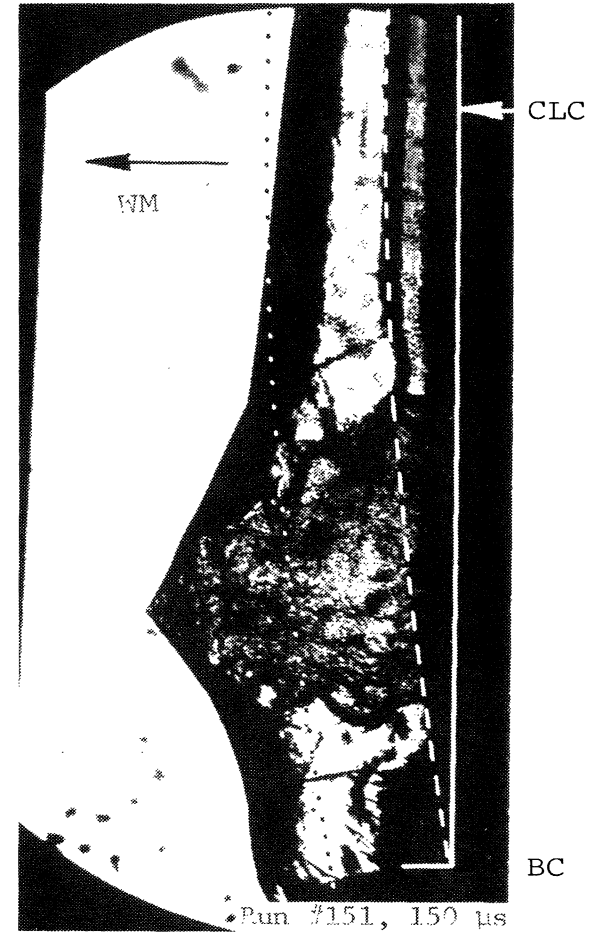


Figure 14. Phenomena Developed at the Wave Front
 a. Blast Wave Front, E-106 + 1.75 grams
 b. Heterogeneous Wave Front, E-106 + 1.75 grams
 c. Heterogeneous Wave Front, E-106 + 3.00 grams



d



e

Figure 14. (concluded)

d. Blast Wave Front, E-106 + 1.75 grams

e. Heterogeneous Wave Front, E-106 + 1.75 grams

a new phenomena is shown. In this photograph, the fuel drops in front of and behind the wave front are visible. Behind the wave front the drops completely occupied the lower half of the exit, but in front of it they were accumulated in the lower portion of the exit. The existence of the drops, either in liquid or evaporating states, was probably caused by the effect of a strong wavy motion of a fuel pad during its retraction. The experimental results (Run 151), shown in Figure 15, reveal that the detonation velocity at the bottom of the chamber was achieved. At the same time velocity in the middle of the chamber was smaller and it showed monotonic decay. The wave front was also, due to the debris, strongly distorted. In this case, it is possible that the appearance of debris close to the bottom of the chamber (somewhere between radii of 31 and 35 inches, see Figure 15) caused an additional acceleration of the wave front in that region. It is also possible that a fuel layer on the bottom of the chamber contributed to acceleration of the wave front.

The general conclusions to be drawn from the studies presented herein show that in both cases (i.e., blast and heterogeneous waves) the wave front shape slightly deviated from the ideal cylindrical shape. The largest distortions of ideal cylindrical shape of a wave front appeared to be due to the debris and also in certain cases due to unpredictable abnormalities. Tentatively, it has been concluded that these distortions could cause substantial scatter of radius versus time data.

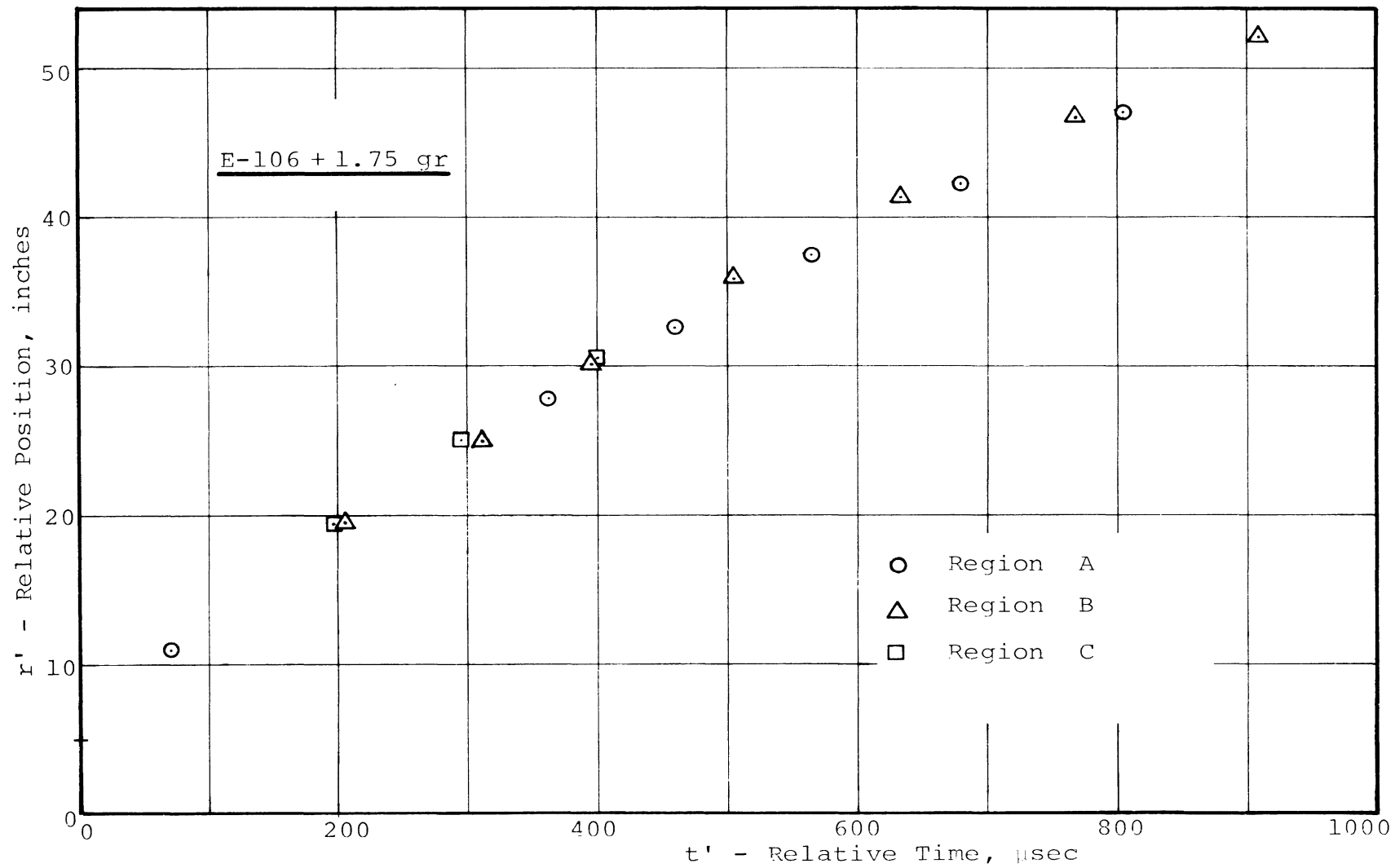


Figure 15. Experimental Heterogeneous Data, r' Versus t' .

D. PROPAGATION OF DETONATION THROUGH A NON-UNIFORM HETEROGENEOUS MIXTURE

Thus far, it has been assumed that a heterogeneous fuel-air mixture was uniformly distributed throughout the chamber. In reality this distribution has not been ideally uniform. The effect of previously mentioned factors (unequal fuel mass flow rate, existence of a fuel spray, appearance of fuel gaps, etc.) has shown that there was some degree of non-uniformity. For the experiments performed so far, it was assumed that the degree of non-uniformity was negligible and that the equivalence ratio, $\phi = 0.753$, was constant along the chamber.

In this section we will investigate cases where a non-uniform heterogeneous mixture was deliberately established. The basic concern of this investigation was to examine the following two problems:

1. To what extent would a localized void in fuel effect propagation of a heterogeneous detonation wave and how great (spacially) a void would be required to terminate propagation?
2. What would be the minimum blast wave strength necessary to initiate a heterogeneous detonation under non-uniform conditions?

In order to create a non-uniform distribution, some of the fuel injecting needles were removed from the chamber. The fuel from these needles was channeled into a separate container. This was necessary to maintain a constant operating point. The

removed needles were replaced by solid rods to prevent pressure relief from the chamber. To establish a meaningful radial position for the void in fuel, the previous results (uniform heterogeneous distribution data) were analyzed. Analysis of the data showed that two regions were of special interest.

In the first case, Case 1, the void in fuel was located near the beginning of the chamber. Thus, the initial blast wave decayed longer than in the uniform distribution case. Results for this case could establish the minimum blast energy level necessary to initiate heterogeneous detonation. For this case, $\phi = 0$ for $0 < r < R_1$, and $\phi = 0.753 = \text{const}$ for $r > R_1$.

For the second case, Case 2, the location of the void in fuel was chosen as a region near the theoretical critical radius. This case was chosen to investigate whether a heterogeneous detonation wave, passing a region in which there was a void in fuel, would continue as a heterogeneous detonation or decay. Thus for this case, $\phi = 0$ for $0 < r < R_1$; $\phi = 0.753 = \text{const}$ for $R_1 < r < R_9$; $\phi = 0$ for $R_9 < r < R_i$, and $\phi = 0.753 = \text{const}$ for $R_i < r < R_{21}$. The radial positions of the needle rows 1, 9, and 21 are indicated as R_1 , R_9 , and R_{21} . A radial position of a removed row was noted as R_i . The row number 9 (R_9), which was the beginning of the fuel void region, was chosen after analyzing the previous experimental results. The above cases are shown in Figure 16. The initial blast energy levels were E-106 plus 1.75, 2.0, 2.5, and 3.0 grams of Detasheet.

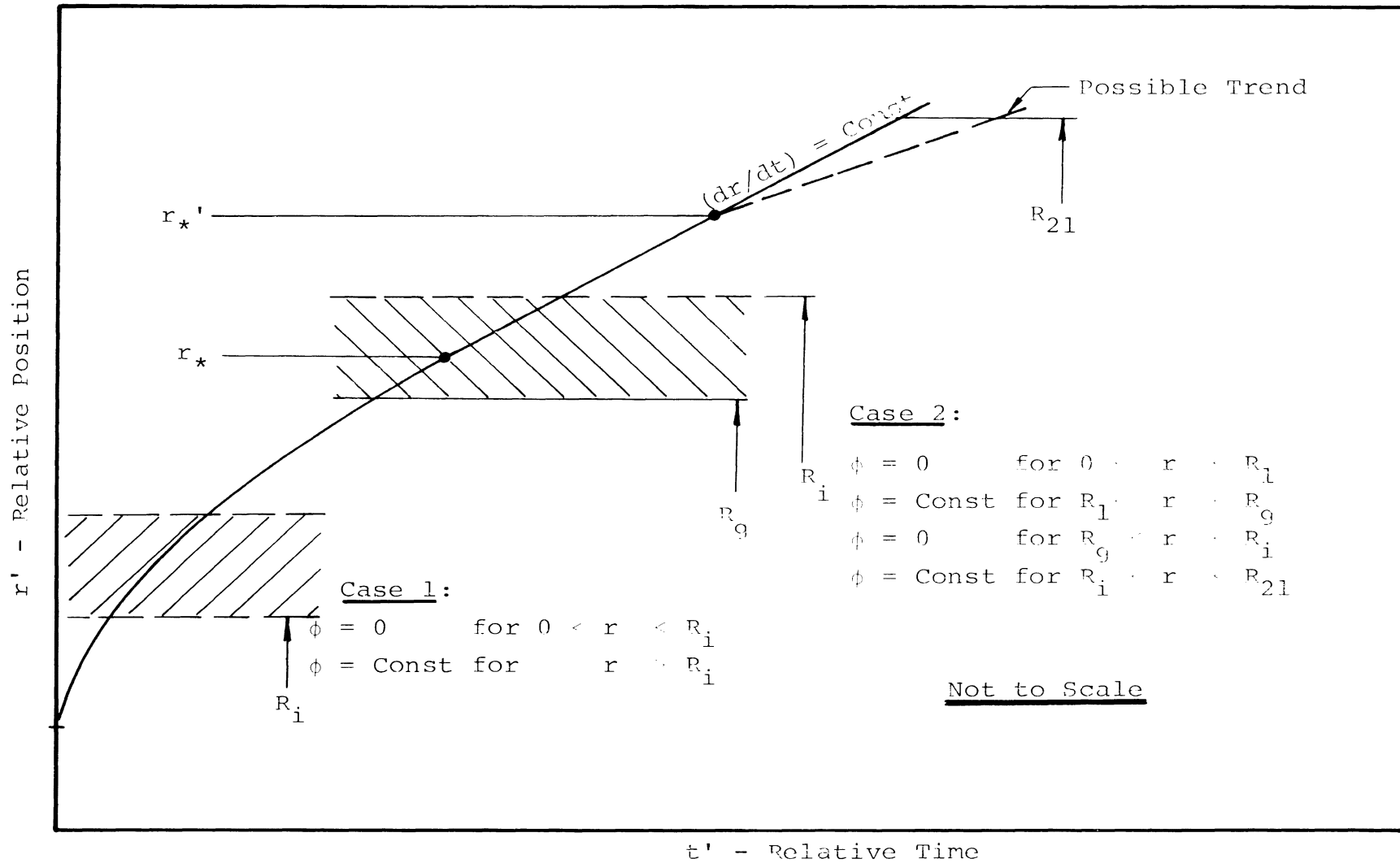


Figure 16. Cases of Non-Uniform Fuel-Air Distribution

Experimental Results and Discussion

Case 1

The experimental results in this case were not completely satisfactory. The experiments with one, two, or three needle rows removed from the chamber showed substantial scatter in radius versus time data. These data were obtained with the rearranged position of the pressure switches (see Part C) as well as with all of them placed on the side centerline of the chamber. The variation in data, particularly that in the regions A and B, was as much as 35 percent. Larger discrepancies were noticed within the extended part of the chamber, and slightly smaller discrepancies were noticed within the original part. Also, it was found that the scatter in data depends on an initial blast energy level and the number of removed needle rows. In general, for a high initial energy level with one or two removed needle rows, a heterogeneous detonation at the bottom and in the middle of the chamber was achieved. Data also showed that two distinctive heterogeneous detonation velocities could exist. With a moderate initial energy level (2.0 grams) and two or three removed needle rows, only one heterogeneous detonation velocity was observed. For a low initial energy level, E-106 plus 1.75 grams, and any number of removed needle rows, the results showed monotonic decay in the radius versus time data.

These results were not consistent, and no two runs produced identical data. Because these results were not conclusive, they will not be presented here in detail.

The only satisfactory results obtained for this case were for an initial blast energy level of E-106 plus 3.0 grams and where the first four needle rows were removed. The results, radius versus time, are shown in Figure 17. The data show a high consistency and a small scatter (up to 3 percent) with the largest variation appearing in the extended part of the chamber. In this case an initial blast wave decay was followed by two distinctive heterogeneous detonation velocities. The first initiation of detonation was detected at a critical radius of about 25.6 inches. At a radial position of approximately 38 to 40 inches, the initial detonation velocity was followed by a lower detonation velocity. It was found that the second detonation velocity varied within a range of Mach numbers from 3.06 to 3.25. The first detonation velocity was achieved at a Mach number of 3.80.

The unusual behavior in radius versus time data in case 1, as shown by the large scatter, could not be explained satisfactorily. However, it is possible that this erratic behavior originated within a strongly deteriorated breech cavity in which there was an unsteady development of a leading blast wave. Also, it was found that an improper mounting of a condensed explosive on the blasting cap would adversely affect the initiation of the explosion and, hence, propagation of the blast wave. The effect of breech cavity deterioration was partially investigated and reported⁽⁸⁾ before. The effect of the other factors on blast and heterogeneous wave development was not investigated here in detail. It should be mentioned that the results presented herein were obtained using the breech with a strongly damaged cavity.

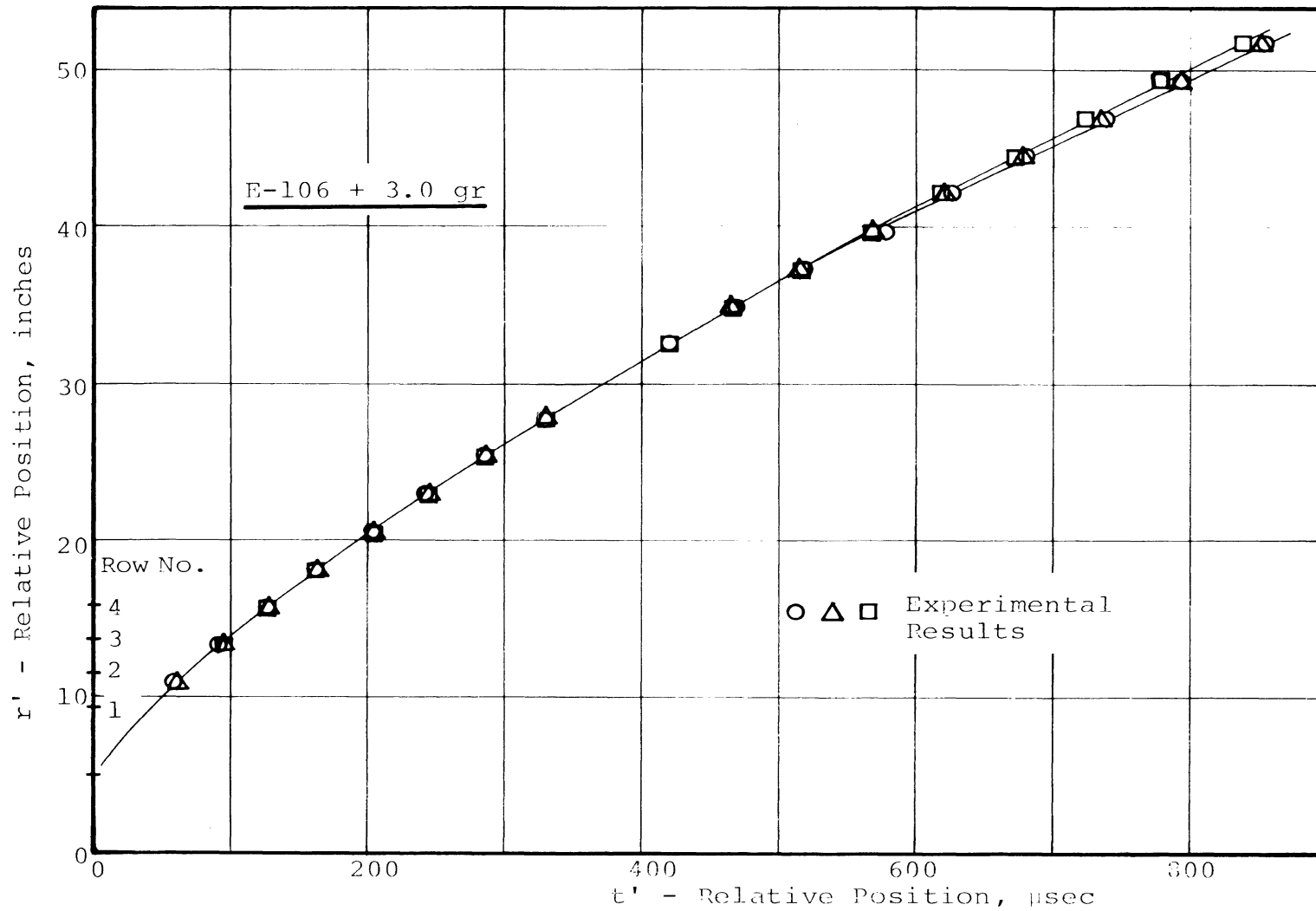


Figure 17. Experimental Heterogeneous Data, r' Versus t' ,
Row Nos. 1, 2, 3, and 4 Removed

Case 2

It was necessary to establish a base to which the non-uniform heterogeneous results of case 2 could be compared. Hence, a number of new experiments with uniform heterogeneous mixtures were conducted. The average radius versus time variations, taken from a large number of experiments, are shown in Figures 18-21. The discrete points for a few of these experiments are also shown. These results show that for a high initial blast energy level (≥ 2.0 gr) a heterogeneous detonation was achieved. Also, it was definitely shown that a second detonation velocity existed. The existence of two heterogeneous detonation velocities could not be explained, although some indications presented in Section C showed that this might be due to the non-ideal experimental conditions. The transition region (which was shorter as higher energy was used) between these two detonation velocities was placed at a radial position of approximately 40 in. In the cases when a low initial energy level (1.75 gr) was used, a heterogeneous detonation was occasionally achieved. This indicates that this energy is approaching the threshold energy. The experimental results showed a high consistency and the scatter of data was small, below $\pm 5\%$.

A non-uniform fuel-air distribution was generated (using the method explained at the beginning) so that a fuel gap of controlled size existed. Removing consecutive needle rows 9, 10, 11, and 12, an air only cloud was of the size (measured in the radial direction) 4.3, 6.5, 8.6, and 10.8 in., respectively.

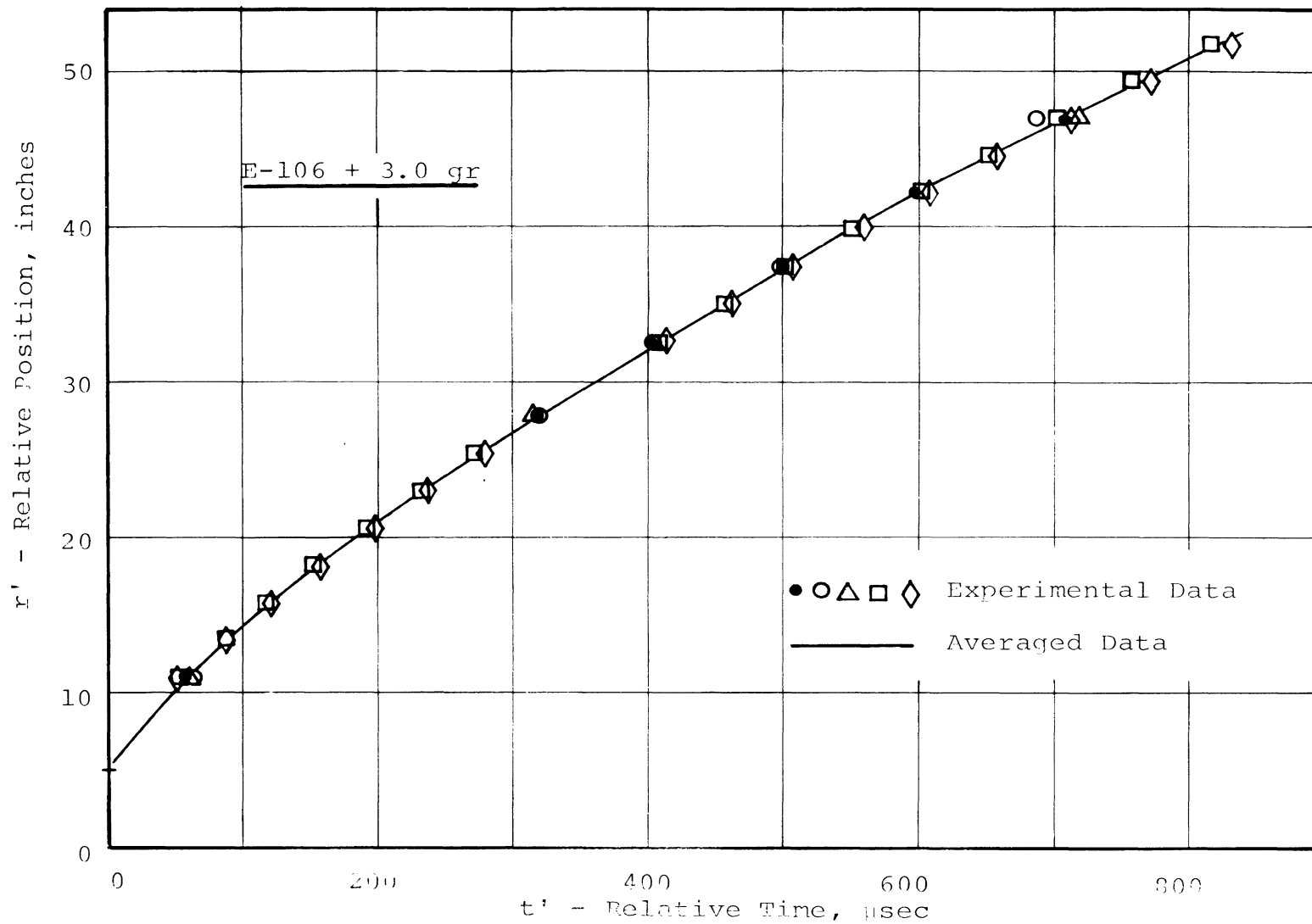


Figure 18. Experimental Heterogeneous Data, r' Versus t'

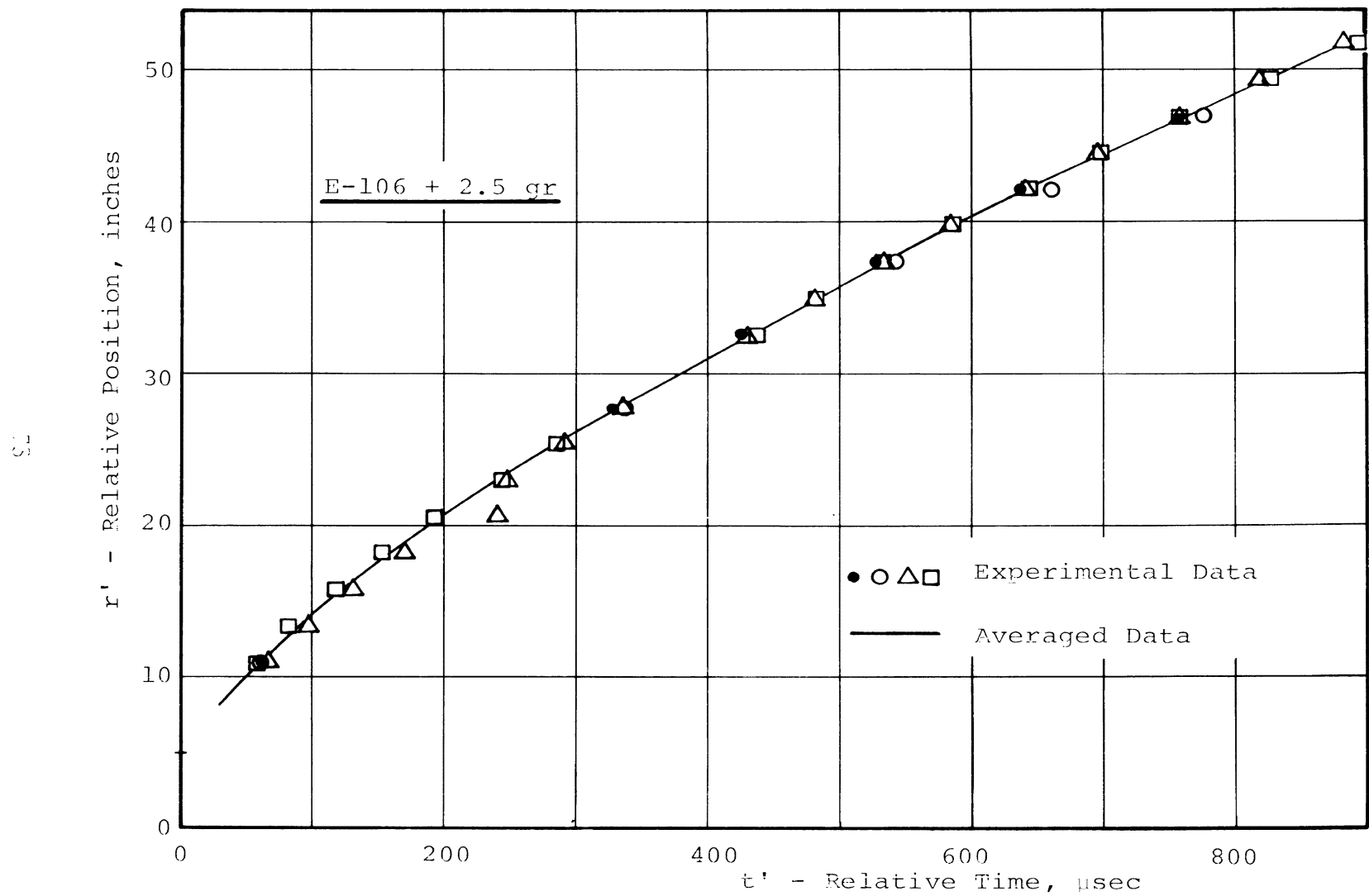


Figure 19. Experimental Heterogeneous Data, r' versus t'

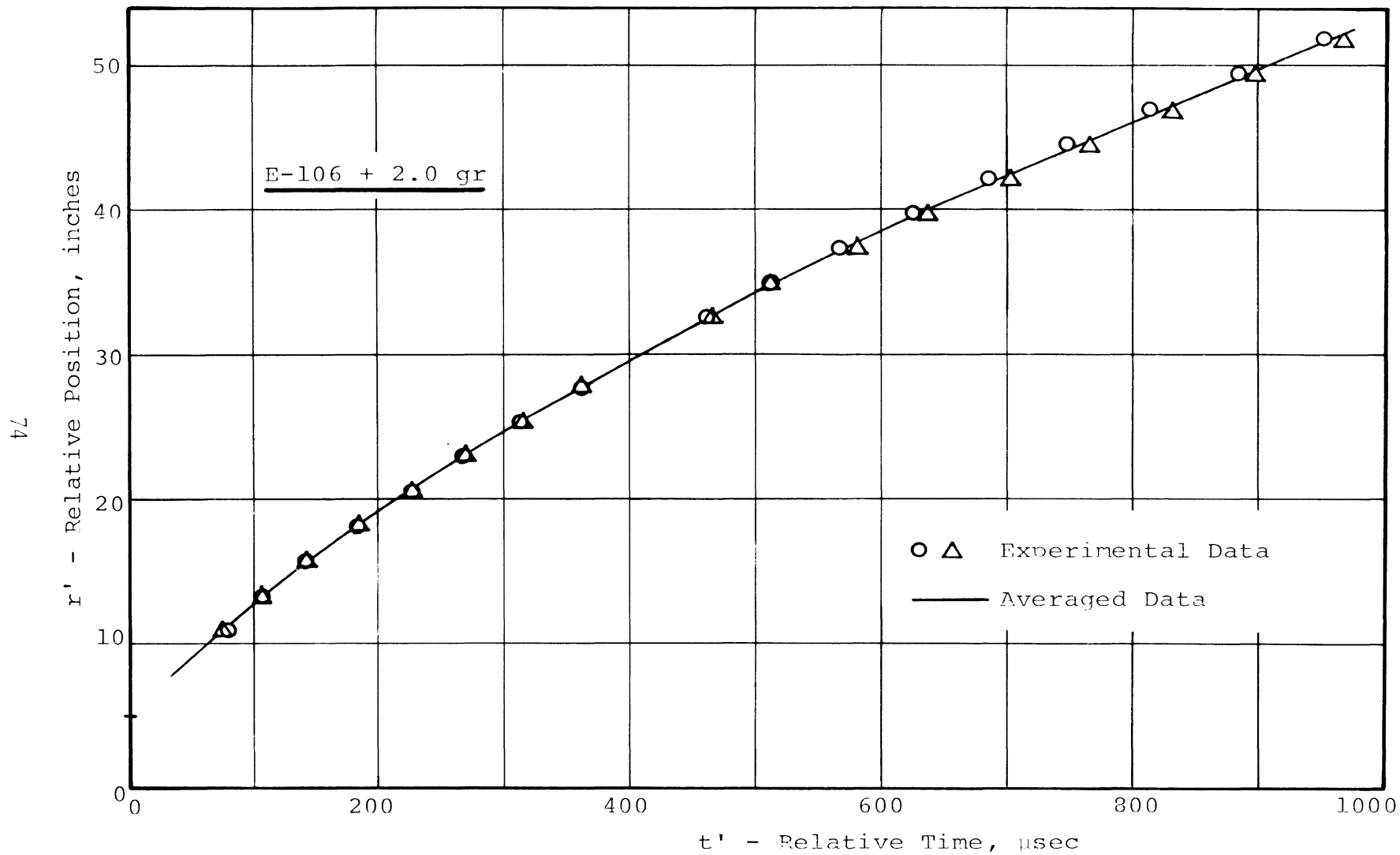


Figure 20. Experimental Heterogeneous Data, r' Versus t'

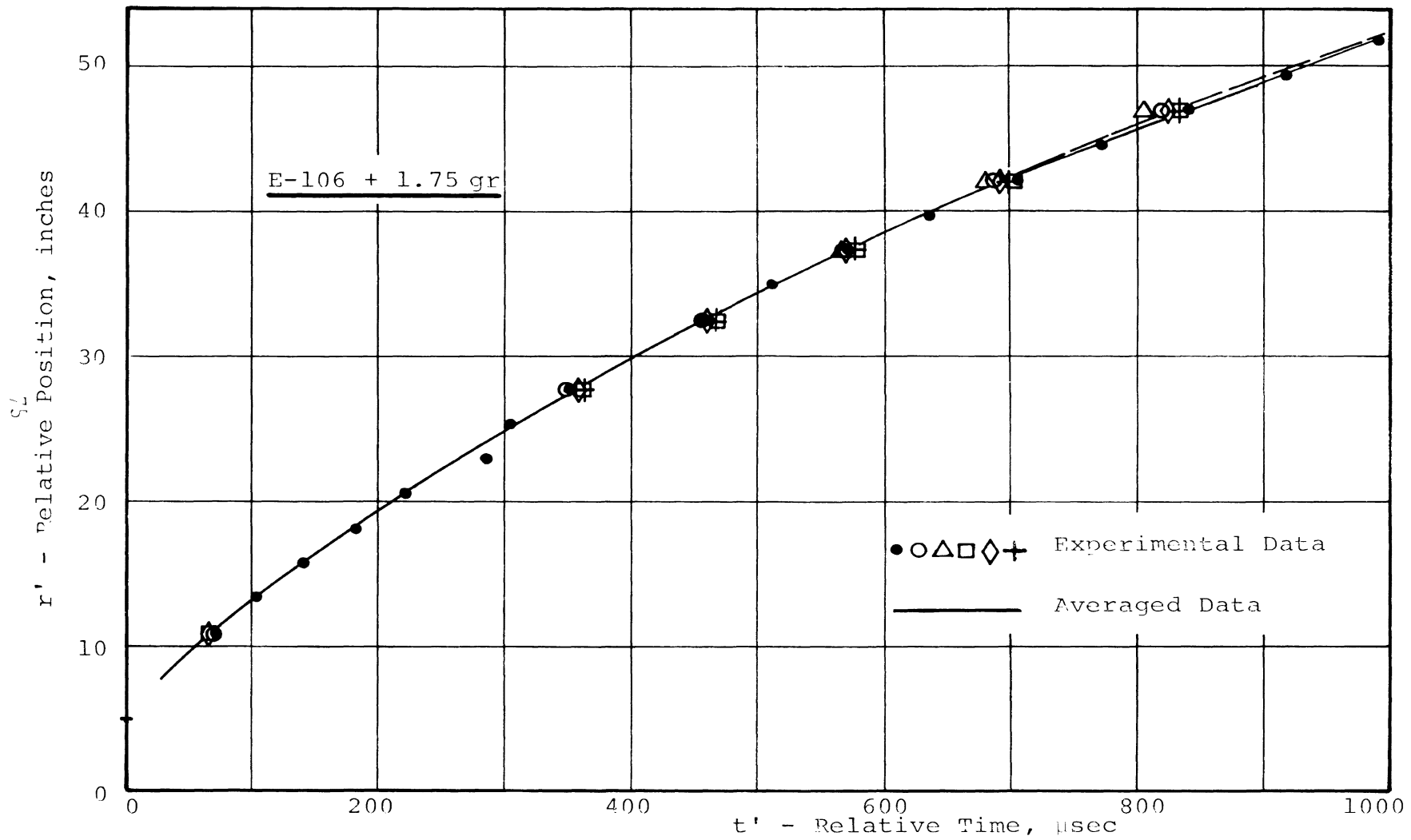


Figure 21. Experimental Heterogeneous Data, r' Versus t'

Initial blast energy levels of 1.75, 2.0, 2.5, and 3.0 gr of Detasheet were used. The experimental results, radius versus time, of the non-uniform heterogeneous mixture are shown in Figures 22 and 23. This is shown only qualitatively to avoid obscuring the data. More detailed behavior of these runs are presented in Table 1.

The effect of non-uniform distribution can be summarized. In the case of a high energy level (≥ 2.0 gr) and one or two removed needle rows, a heterogeneous detonation was achieved. Also, two distinct detonation velocities were observed. With further removal of the needle rows, the radius versus time data changed to indicate only one heterogeneous detonation velocity or no detonation at all. With a low initial energy level and any number of removed needle rows a monotonic decay was detected. In general, with a smaller initial energy level or with the removal of more needle rows, heterogeneous detonation velocities decreased until monotonic decay was reached. There were some abnormalities observed, though. For instance, it was found that the highest heterogeneous detonation velocities were achieved in the case when two needle rows (Nos. 9 and 10) were removed and an initial energy level of 3.0 gr was used. Furthermore, it was observed that the detonation velocities (in some cases) were higher when more needle rows were removed. The reason for such behavior of a wave front propagation was not investigated here and at the present a reasonable explanation is not available. It was also found that it was not possible to establish a general trend of how the critical radius was changing.

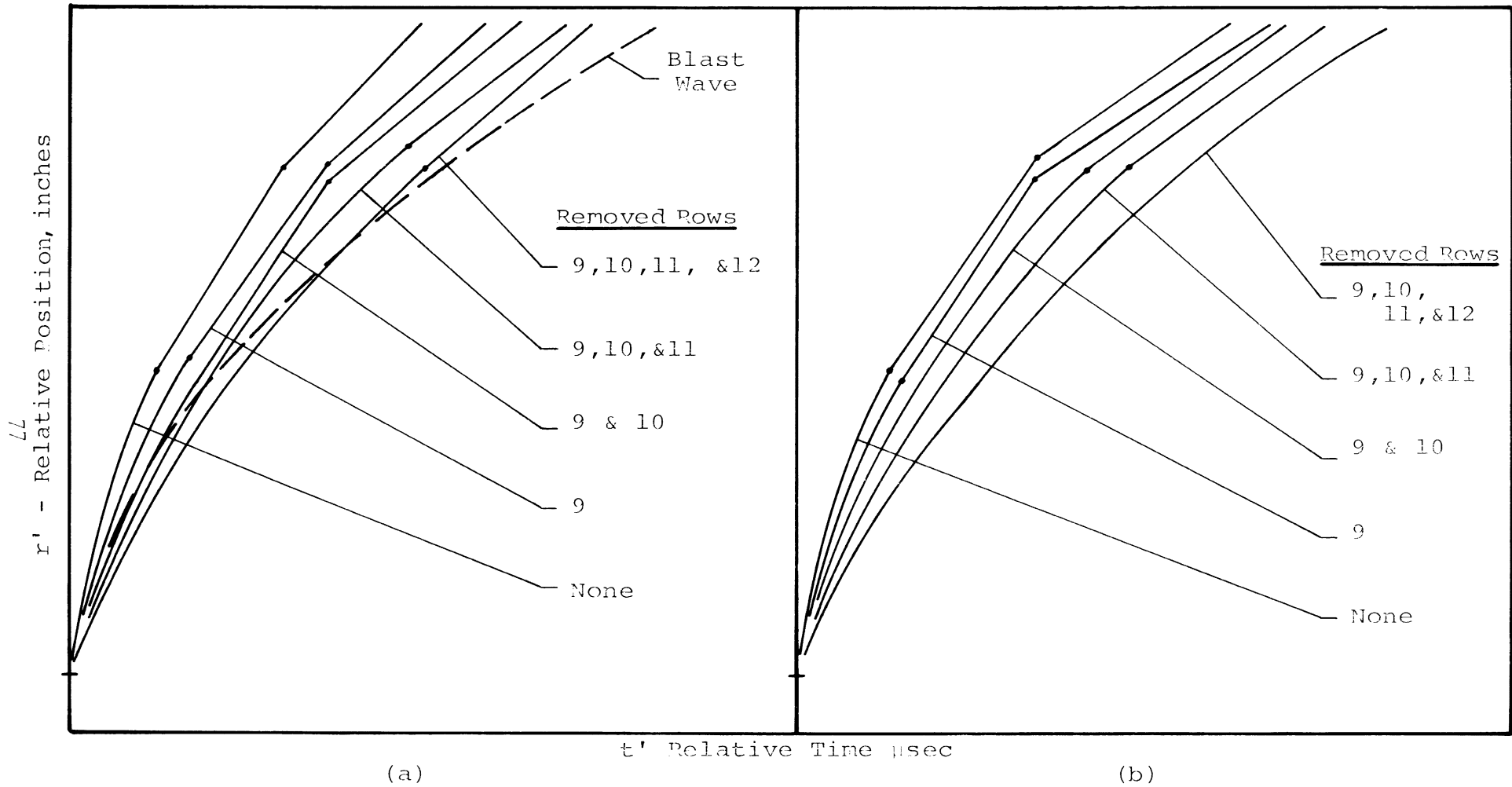


Figure 22. Qualitative Trends of Experimental Non-Uniform Data, r' versus t'
 (a) E-106 + 3.0 gr; (b) E-106 + 2.5 gr

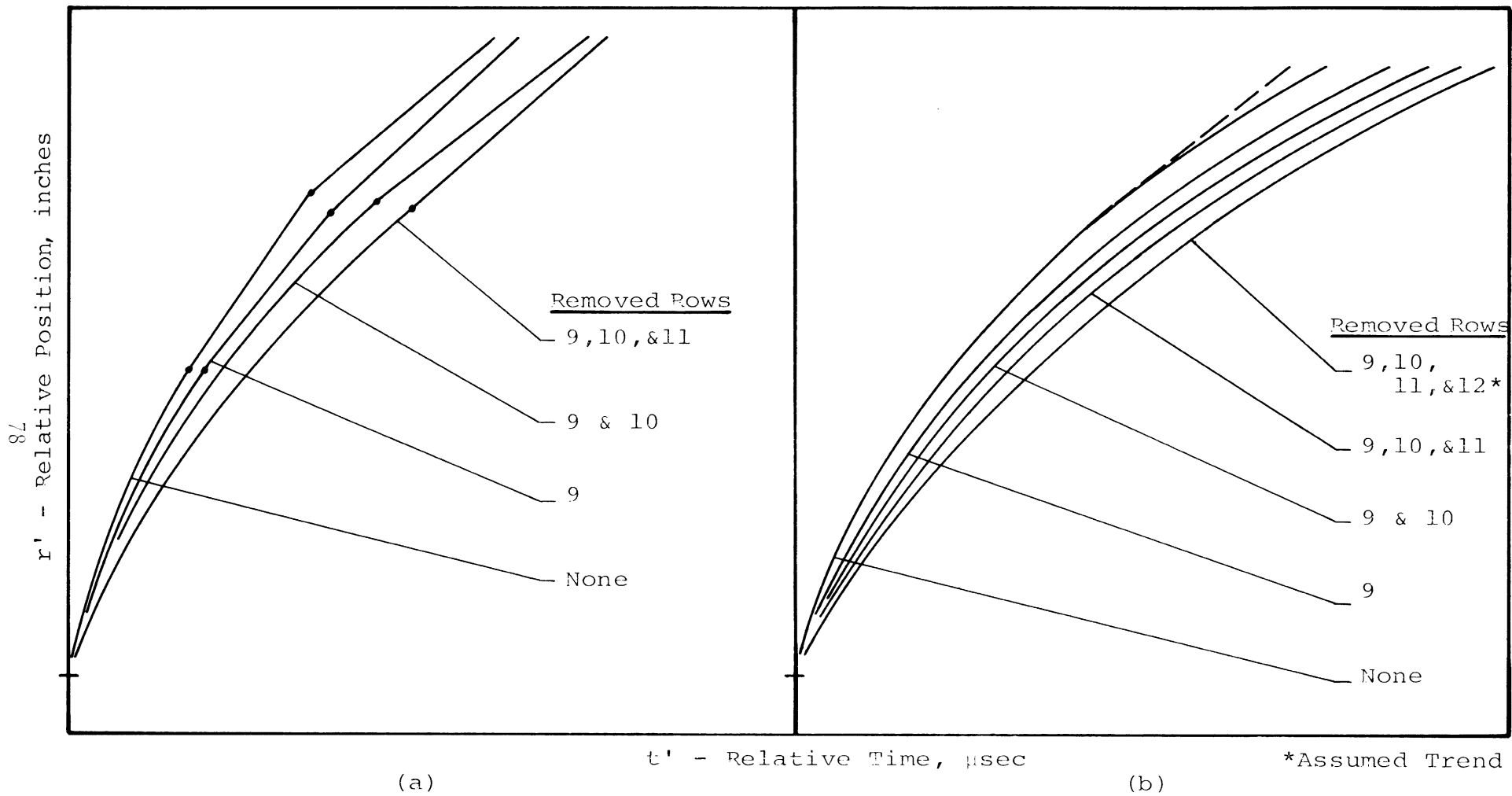


Figure 22. (concluded)

(c) E-106 + 2.0 gr; (d) E-106 + 1.75 gr

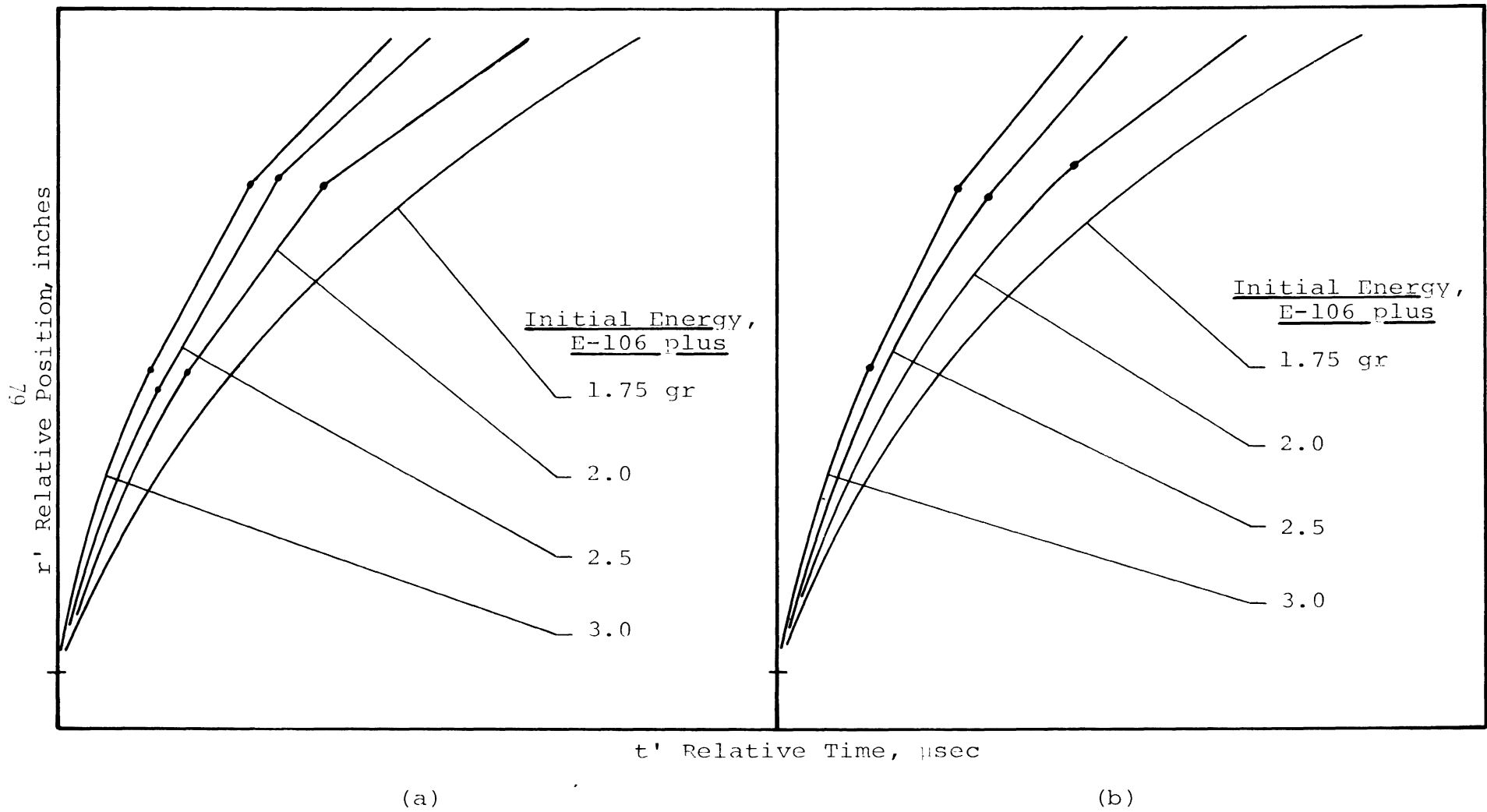


Figure 23. Qualitative Trends of Experimental Non-Uniform Data, r' Versus t'
 (a) Row 9 Removed; (b) Rows 9 and 10 Removed

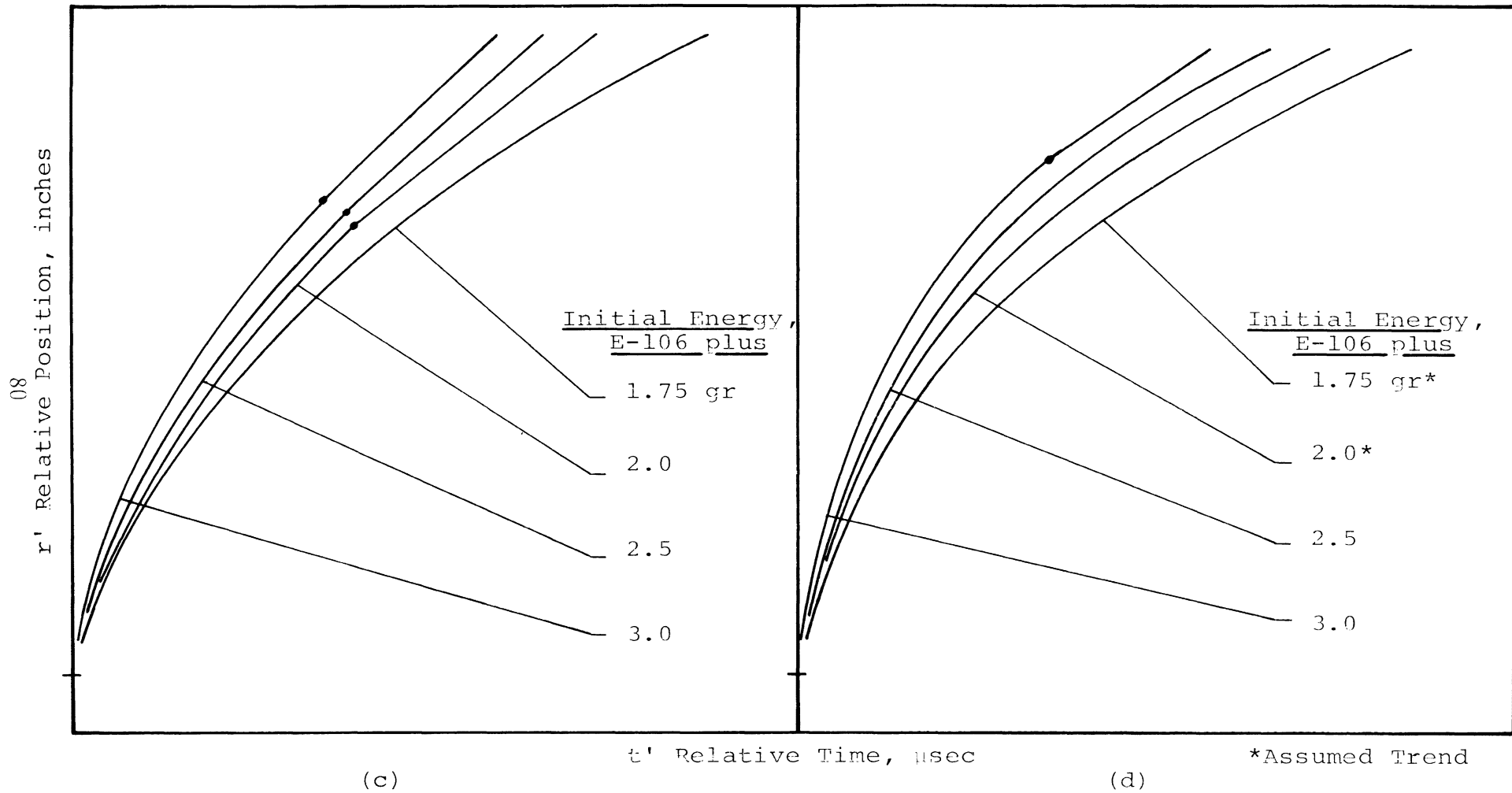


Figure 23. (concluded)

(c) Rows 9, 10, and 11 Removed

(d) Rows 9, 10, 11, and 12 Removed

TABLE 1. NON-HOMOGENEOUS RESULTS

Removed Row(s)	Initial En Level E-106 +	r* inches	r*' inches	M	M'	M _N /M _U	M _N '/M _U '	Scatter of Experimental Data	Overall Behavior of a Wave Front
None	3.00	27.0	41.0	3.84	3.42			Small	2 Deton Velocities
	2.50	27.0	40.8	3.47	3.01			Small	2 Deton Velocities
		36.0		3.02					1 Deton Velocity
	2.00	33.2	41.6	3.11	2.66			Small, higher in extent	2 Deton Velocities
		36.0	44.0	3.07				High in original	1 Deton Velocity
	38.9		3.01						1 Deton Velocity
1.75	39.6		2.88						Monotonic Decay
	41.2		2.41						
No. 9	3.00	33.2	41.0	3.44	3.01	.89	.88	Small	2 Deton Velocities
		33.5	41.5	3.58	2.90	.93	.85		
	2.50	25.8	37.4	3.72	2.97	1.07, 1.23	.98	Small	2 Deton Velocities
	2.00	25.6	38.8	2.78		.80, .92			1 Deton Velocity
		33.4	40.0	3.01	2.78	.96, .98	1.043	Small	2 Deton Velocities
1.75							Small	Monotonic Decay	
Nos. 9 & 10	3.00	26.4	39.8	4.11	2.97	1.07	.87	High in Central Part	2 Deton Velocities
		25.4	37.4	3.94	3.23	1.02	.94		
	2.50	37.8		3.01		.86, .99		High in Extended	1 Deton Velocity
	2.00	40.0		2.92		.84, .96			
		44.6		2.59		.83, .84		Small	1 Deton Velocity
1.75	40.4		2.73		.87, .88			Monotonic Decay	
Nos. 9, 10, & 11	3.00	44.6		2.90		.75		High in original	1 Deton Velocity
		42.6		2.94		.76			
	2.50	40.4		3.00		.86, .99		High in Extended	1 Deton Velocity
	2.00	42.2		2.88		.83, .95			
		38.0		2.93		.94, .95			1 Deton Velocity
1.75	38.4		2.84		.91, .92			Monotonic Decay	
Nos. 9, 10, 11, & 12	3.00	38.0		3.18		.82		Small	1 Deton Velocity
		40.2		3.10		.80			
	2.50	40.3		3.10		.80		Small	Monotonic Decay

Note: r* - Critical radius of first detonation
 r*' - Critical radius of second detonation
 M - Mach number of first detonation
 M' - Mach number of second detonation

The effect of different sizes of void in fuel on non-uniform heterogeneous detonation was quantitatively compared by a ratio of, M_N/M_U and M'_N/M'_U , where M and M' represent Mach numbers of the first and second detonation velocity and subscripts N and U were related to a non-uniform and uniform heterogeneous mixture. The calculated ratios are presented in Table I. In general, these ratios were smaller than one. This indicates that an adverse effect of non-uniformity on heterogeneous detonation existed. These ratios were slightly larger or smaller than one when only one needle row was removed. A similar effect occurred when two needle rows were removed and an initial energy of 3.0 gr was used.

The general conclusion to be drawn from the presented studies (case 2) suggest that the non-uniform heterogeneous detonation velocities in the cases of high and moderate initial energy levels (≥ 2.0 gr) will re-adjust to new detonation velocities when exposed to the air cloud sizes studied here. In the case of low initial energy level (1.75 gr) an overall monotonic decay was observed. The new re-adjusted non-uniform heterogeneous detonation velocities were lower than those achieved in uniform heterogeneous mixture. Their ratios, i.e. ratios of corresponding Mach numbers, were for most cases smaller than one. The experiments performed when a void in fuel was located near the beginning of the chamber (case 1) gave inconclusive data.

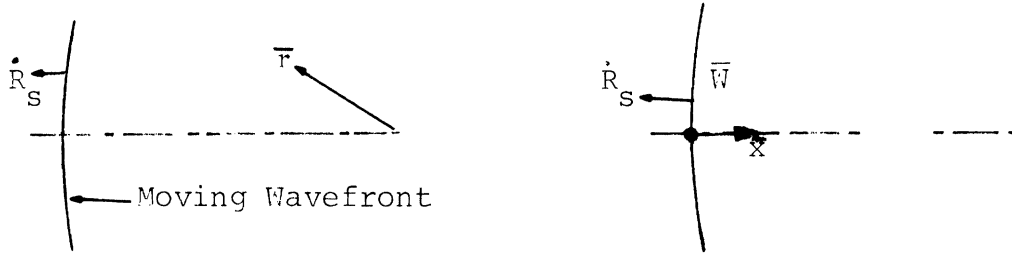
REFERENCES

1. Nicholls, J.A., Fry, R.S., Glass, D.R., Sichel, M., Vander Schaff, J., and Sternstein, A.J., "Fundamental Aspects of Unconfined Explosions," Technical Report, AFATL-TR-72-49, March 1972.
2. Nicholls, J.A., Sichel, M., Fry, R.S., Hu, C., Glass, D.R., DeSaro, K., and Kearney, K., "Fundamental Aspects of Unconfined Explosions," Technical Report, AFATL-TR-73-125, March 1973.
3. Nicholls, J.A., Sichel, M., Fry, R.S., Hu, C., DeSaro, R., and Kearney, K., "Fundamental Aspects of Unconfined Explosions," Technical Report, AFATL-TR-74-123, August 1974.
4. Nicholls, J.A., Sichel, M., Fry, R., and Glass, D.R., "Theoretical and Experimental Study of Cylindrical Shock and Heterogeneous Detonation Waves," *Acta Astronautica*, Vol. 1, 1974, pp. 385-404.
5. Fry, R.S. and Nicholls, J.A., "Blast Initiation and Propagation of Cylindrical Detonations in MAPP-Air Mixtures," *AIAA Journal*, Vol. 12, No. 12, December 1974.
6. Fry, R.S. and Nicholls, J.A., "Blast Wave Initiation of Gaseous and Heterogeneous Cylindrical Detonation Waves," Fifteenth Symposium (International) on Combustion, The Combustion Institute, Pittsburgh, Pa., 1974.
7. Sichel, M. and Hu, C., "The Impulse Generated by Blast Waves Propagating through Combustible Mixtures," Proceedings of the Conference on Mechanisms of Explosion and Blast Waves, Naval Weapons Sta., Yorktown, Va., 13-15 November 1973.
8. Nicholls, J.A., Sichel, M., Fry, R.S., Oza, R., Gabrijel, Z., "Fundamental Aspects of Unconfined Explosions: Phase I," Technical Report, AFATL-TR-76-77, 1976.
9. Fry, R.S., "Blast Initiation and Propagation in Detonable Homogeneous and Heterogeneous Mixtures," Aerospace Engineer Thesis, The University of Michigan, 1975.
10. Bach, G.G., Knystautas, R., and Lee, J.H., "Initiation Criteria for Diverging Gaseous Detonations," Thirteenth Symposium (International) on Combustion, The Combustion Institute, Pittsburgh, Pa., 1970.

11. Edelman, R.B., Fortune, O., and Weilerstein, G., "Some Observations on Flows Described by Coupled Mixing and Kinetics," Emissions from Continuous Combustion Systems, Plenum Press, New York, 1972.
12. Strehlow, R.A., Cohen, A., "Initiation of Detonation," Physics of Fluids, Vol. 5, 1962, pp. 97-110.
13. White, D.R., Eleventh Symposium (International) on Combustion, The Combustion Institute, Pittsburgh, Pa., 1967, p. 147.
14. Clarke, E.H., "Ignition Analysis of Adiabatic, Homogeneous Systems Including Reactant Consumption," AIAA J., Vol. 11, No. 12, December 1973.
15. Kassoy, D.R., "Perturbation Methods for Mathematical Models of Explosion Phenomena," Q. Jl. Mech. Appl. Math., Vol. XXVIII, Pt. 1, 1975.
16. Sichel, M., "A Simple Analysis of the Blast Initiation of Detonations," accepted for publication in Acta Astronautica.

APPENDIX A

COORDINATE TRANSFORMATION



Wave moving at velocity \dot{R}_s with respect to a stationary observer.

Wave stationary with respect to an observer.

Where \bar{r} is measured from the center of symmetry and \bar{x} is measured from the wave front.

$$\bar{W} = \dot{R}_s - \bar{u} \quad (A-1)$$

$$x = R_s - \bar{r} \quad (A-2)$$

Inner Regime

Define the inner coordinates as $\eta = x/l_c$ and $\tau = \bar{t}/\tau_B$

where

$$l_c = \beta \dot{R}_s e^{\bar{T}/\bar{T}_s} / (\beta Y_{i_0}^{a-1} Y_{i_0}^b)$$

and

$$\tau_B = R_s / \dot{R}_s$$

Therefore,

$$\frac{\partial}{\partial \bar{t}} = \frac{\partial}{\partial \eta} \frac{\partial \eta}{\partial \bar{t}} + \frac{\partial}{\partial \tau} \frac{\partial \tau}{\partial \bar{t}}$$

$$\frac{\partial \eta}{\partial \bar{t}} = \frac{\partial}{\partial \bar{t}} \left\{ \frac{R_s - \bar{r}}{l_c} \right\} = \frac{\dot{R}_s}{l_c} - \frac{R_s - \bar{r}}{l_c^2} \dot{l}_c = \frac{\dot{R}_s}{l_c} - \frac{\dot{l}_c}{l_c} \eta \quad (A-3)$$

and

$$\frac{\partial \tau}{\partial \bar{t}} = \frac{\partial}{\partial \bar{t}} \left(\frac{\bar{t}}{\tau_B} \right) = \frac{1}{\tau_B} - \frac{\bar{t}}{\tau_B^2} \frac{\partial \tau_B}{\partial \bar{t}}$$

where

$$\frac{\partial \tau_B}{\partial \bar{t}} = \frac{\partial}{\partial \bar{t}} \left(\frac{R_S}{\dot{R}_S} \right) = 1 - \frac{R_S}{\dot{R}_S^2} \ddot{R}_S = 1 - \theta$$

where

$$\theta = \frac{R_S \ddot{R}_S}{\dot{R}_S^2} \quad (\text{A-4})$$

Thus

$$\frac{\partial \tau}{\partial \bar{t}} = \frac{1}{\tau_B} - \frac{\bar{t}}{\tau_B^2} \frac{\partial \tau_B}{\partial \bar{t}} = \frac{1}{\tau_B} [1 - \tau(1 - \theta)] \quad (\text{A-5})$$

and

$$\frac{\partial}{\partial \bar{t}} = \frac{\dot{R}_S}{\ell_C} \left(1 - \frac{\dot{\ell}_C}{\dot{R}_S} \eta \right) \frac{\partial}{\partial \eta} + \frac{1}{\tau_B} [1 - \tau(1 - \theta)] \frac{\partial}{\partial \tau} \quad (\text{A-6})$$

and

$$\frac{\partial}{\partial \bar{r}} = \frac{\partial}{\partial \eta} \frac{\partial \eta}{\partial \bar{r}} = - \frac{1}{\ell_C} \frac{\partial}{\partial \eta} \quad (\text{A-7})$$

$$\frac{D}{D\bar{t}} = \frac{\partial}{\partial \bar{t}} + \bar{u} \frac{\partial}{\partial \bar{r}} = \frac{\dot{R}_S}{\ell_C} \left(1 - \frac{\dot{\ell}_C}{\dot{R}_S} \eta \right) \frac{\partial}{\partial \eta} + \frac{1}{\tau_B} [1 - \tau(1 - \theta)] \frac{\partial}{\partial \tau} - \frac{\dot{R}_S (1 - W)}{\ell_C} \frac{\partial}{\partial \eta}$$

or

$$\frac{D}{D\bar{t}} = \frac{\dot{R}_S}{\ell_C} \left(W - \frac{\dot{\ell}_C}{\dot{R}_S} \eta \right) \frac{\partial}{\partial \eta} + \frac{1}{\tau_B} [1 - \tau(1 - \theta)] \frac{\partial}{\partial \tau} \quad (A-8)$$

APPENDIX B

CALCULATION OF \dot{l}_c / \dot{R}_s

$$l_c = \frac{\beta \dot{R}_s \exp(1/\beta)}{B y_{a_0}^{a-1} y_{b_0}^b}$$

where $\beta = T_s / T_A$, let

$$B_1 = B y_{a_0}^{a-1} y_{b_0}^b$$

therefore

$$\begin{aligned} \dot{l}_c &= \frac{\partial l_c}{\partial \bar{t}} = \frac{1}{B_1} [\dot{\beta} \dot{R}_s \exp(1/\beta) + \beta \ddot{R}_s \exp(1/\beta) \\ &\quad - \beta \dot{R}_s \frac{1}{\beta^2} \dot{\beta} \exp(1/\beta)] \\ &= l_c \left\{ \frac{\dot{\beta}}{\beta} + \frac{\ddot{R}_s}{R_s} - \frac{\dot{\beta}}{\beta^2} \right\} \end{aligned}$$

Now $\dot{\beta} = \frac{\partial \beta}{\partial \bar{t}} = \frac{\partial \beta}{\partial \dot{R}_s} \ddot{R}_s$, where $\ddot{R}_s = \frac{\theta \dot{R}_s^2}{R_s}$

$$\dot{l}_c = l_c \frac{\theta \dot{R}_s^2}{R_s} \left\{ \frac{1}{\beta} \frac{\partial \beta}{\partial \dot{R}_s} - \frac{1}{\beta^2} \frac{\partial \beta}{\partial \dot{R}_s} + \frac{1}{\dot{R}_s} \right\}$$

or
$$\frac{\dot{l}_c}{\dot{R}_s} = \theta \frac{l_c}{R_s} \left\{ 1 + \dot{R}_s \frac{\partial \beta}{\partial \dot{R}_s} \left(\beta - \frac{1}{\beta} \right) \right\} \quad (B-1)$$

Now $\beta = \frac{T_s}{T_A}$ therefore $\frac{dT_s}{dM_s}$ can be calculated as follows

$$\frac{\partial \beta}{\partial R_S} = \frac{1}{C_O T_A} \frac{dT_S}{dM_S} = \frac{\beta}{C_O T_S} \frac{dT_S}{dM_S} \quad (B-2)$$

dT_S/dM_S is calculated as follows.

Across the shock,

$$\frac{T_S}{T_O} = 1 + D \left\{ \frac{(\Gamma_O M_S^2 + 1)}{M_S^2} \right\} (M_S^2 - 1)$$

Therefore

$$\frac{1}{T_O} \frac{dT_S}{dM_S} = D \left\{ 2\Gamma_O M_S - \frac{2\Gamma_O}{M_S} + \frac{2\Gamma_O}{M_S} + \frac{2}{M_S^3} \right\} = D \left\{ 2\Gamma_O M_S + \frac{2}{M_S^3} \right\} \quad (B-3)$$

Substituting into (B-2)

$$\frac{\partial \beta}{\partial R_S} = \frac{\beta}{C_O T_S} D \left\{ 2\Gamma_O M_S + \frac{2}{M_S^3} \right\}$$

Thus Eq. (B-1) becomes

$$\frac{\dot{\ell}}{R_S} = \theta \frac{\ell}{R_S} \left(1 + 2D \left\{ \frac{T_O}{T_S} \right\}^2 \frac{T_A}{T_O} \Gamma_O M_S^2 + \frac{1}{M_S^2} (1 - \beta) \right)$$

or

$$\frac{\dot{\ell}}{R_S} = \theta \frac{\ell}{R_S} F, \quad (B-4)$$

where

$$F = 1 + 2D \left\{ \frac{T_O}{T_S} \right\}^2 \frac{T_A}{T_O} (1 - \beta) \Gamma_O M_S^2 + \frac{1}{M_S^2} \quad (B-5)$$

APPENDIX C

CALCULATION OF $\partial\varepsilon/\partial\tau$ AND $\partial\varepsilon/\partial\eta$

$$\varepsilon = l_c/R_s$$

$$d\varepsilon = \frac{\partial\varepsilon}{\partial\bar{t}} d\bar{t} + \frac{\partial\varepsilon}{\partial\bar{r}} d\bar{r} \quad (C-1)$$

$$d\varepsilon = \frac{\partial\varepsilon}{\partial\tau} d\tau + \frac{\partial\varepsilon}{\partial\eta} d\eta \quad (C-2)$$

$$d\eta = \frac{\partial\eta}{\partial\bar{t}} d\bar{t} + \frac{\partial\eta}{\partial\bar{r}} d\bar{r}$$

$$d\tau = \frac{\partial\tau}{\partial\bar{t}} d\bar{t} + \frac{\partial\tau}{\partial\bar{r}} d\bar{r}$$

Substitute for $d\tau$ and $d\eta$ in Equation (C-2)

$$d\varepsilon = \frac{\partial\varepsilon}{\partial\tau} \frac{\partial\tau}{\partial\bar{t}} + \frac{\partial\varepsilon}{\partial\eta} \frac{\partial\eta}{\partial\bar{t}} d\bar{t} + \frac{\partial\varepsilon}{\partial\tau} \frac{\partial\tau}{\partial\bar{r}} + \frac{\partial\varepsilon}{\partial\eta} \frac{\partial\eta}{\partial\bar{r}} d\bar{r} \quad (C-3)$$

Comparing (C-1) and (C-3)

$$\frac{\partial\varepsilon}{\partial\bar{t}} = \frac{\partial\varepsilon}{\partial\tau} \frac{\partial\tau}{\partial\bar{t}} + \frac{\partial\varepsilon}{\partial\eta} \frac{\partial\eta}{\partial\bar{t}} \quad (C-4)$$

$$\frac{\partial\varepsilon}{\partial\bar{r}} = \frac{\partial\varepsilon}{\partial\tau} \frac{\partial\tau}{\partial\bar{r}} + \frac{\partial\varepsilon}{\partial\eta} \frac{\partial\eta}{\partial\bar{r}} \quad (C-5)$$

Since l_c and R_s are functions of \bar{t} only, so that ε is also a function of \bar{t} only. i.e. $\partial\varepsilon/\partial\bar{r} = 0$. Similarly $\tau = \bar{t}/\tau_B$ is also a function of \bar{t} only, $\tau = \tau(\bar{t})$, so that $\partial\tau/\partial\bar{r} = 0$.

Equation (5) becomes,

$$\frac{\partial \varepsilon}{\partial \bar{r}} = \frac{\partial \varepsilon}{\partial \eta} \frac{\partial \eta}{\partial \bar{r}}$$

Since $\partial \varepsilon / \partial \bar{r} = 0$, we get (if $\partial \eta / \partial \bar{r} \neq 0$),

$$\frac{\partial \varepsilon}{\partial \eta} = 0 \quad (\text{C-6})$$

Substituting $\partial \varepsilon / \partial \eta = 0$ in Equation (C-4), we get

$$\frac{\partial \varepsilon}{\partial \tau} = \frac{\partial \varepsilon}{\partial \bar{\tau}} / \frac{\partial \tau}{\partial \bar{\tau}} \quad (\text{C-7})$$

which requires calculation of $\partial \varepsilon / \partial \bar{\tau}$ and $\partial \tau / \partial \bar{\tau}$

$$\begin{aligned} \frac{\partial \varepsilon}{\partial \bar{\tau}} &= \frac{\partial}{\partial \bar{\tau}} \left\{ \frac{l_c}{R_s} \right\} = \frac{\dot{l}_c}{R_s} - \frac{l_c}{R_s^2} \dot{R}_s \\ &= \frac{\dot{R}_s}{R_s} \left\{ \frac{\dot{l}_c}{\dot{R}_s} - \frac{l_c}{R_s} \right\} \end{aligned}$$

using (B-4) we get,

$$\frac{\partial \varepsilon}{\partial \bar{\tau}} = \frac{1}{\tau_B} (\theta F \varepsilon - \varepsilon) = \frac{\varepsilon}{\tau_B} (F\theta - 1) \quad (\text{C-8})$$

Similarly $\partial \tau / \partial \bar{\tau}$ is calculated as follows

$$\frac{\partial \tau}{\partial \bar{\tau}} = \frac{\partial}{\partial \bar{\tau}} \frac{\bar{\tau}}{\tau_B} = \frac{1}{\tau_B} - \frac{\bar{\tau}}{\tau_B^2} \frac{\partial \tau_B}{\partial \bar{\tau}}$$

where

$$\frac{\partial \tau_B}{\partial \bar{t}} = \frac{\partial}{\partial \bar{t}} \frac{R_S}{\dot{R}_S} = 1 - \frac{R_S}{\dot{R}_S} \ddot{R}_S = 1 - \theta$$

Therefore

$$\frac{\partial \tau}{\partial \bar{t}} = \frac{1}{\tau_B} [1 - \tau(1 - \theta)] \quad (C-9)$$

Substituting (C-3) and (C-9) in (C-7) ,

$$\frac{\partial \varepsilon}{\partial \bar{t}} = \left\{ \frac{\varepsilon}{\tau_B} (F\theta - 1) \right\} / \left\{ \frac{1}{\tau_B} [1 - \tau(1 - \theta)] \right\}$$

or

$$\frac{\partial \varepsilon}{\partial \bar{t}} = \frac{\varepsilon (F\theta - 1)}{[1 - \tau(1 - \theta)]} \quad (C-10)$$

INITIAL DISTRIBUTION

Hq USAF/RDQRM	1	Air Force Office of Scientific	
Hq USAF/SAMI	1	Research/NA	1
AFIS/INTA	1	IIT Research Inst	1
AFSC/DLCA	1	ASD/ENESS	1
AFSC/IGFG	1		
AFWAL/Tech Lib/FL2802	1		
ASD/ENFEA	1		
FTD/PDXA-2	1		
AFWL/NSC	1		
AFWL/NSE	1		
AFWL/SUL	1		
AUL/AUL/LSE-70-239	2		
DDC	2		
Ogden ALC/MMWM	2		
TAC/DRA	1		
6510 ABG/SSD	1		
Hq USAFE/DOQ	1		
Hq PACAF/DOO	1		
Rock Island Ars/SARRI-LW	1		
Picatinny Ars/SARPA-TS-S#59	1		
Redstone Sci Info Ctr/Doc Sec	2		
USAE Waterways Experiment Stn			
WESFE	1		
Naval Rsch Lab/Code 2627	1		
NAVAIR SYS COMD/Code 530C	1		
NAVAIR SYS COMD/Tech Lib	1		
Naval Surface Wpn Ctr/Tech Lib	2		
Naval Ord Stn/Tech Lib	1		
Naval Air Test Ctr/Tech Pubs	2		
USNWC (Code 533)/Tech Lib	1		
Sandia Lab/Tech Lib Div 3141	1		
The Rand Corp	1		
TACTEC	1		
TAWC/TRADOCLO	1		
AFATL/DL	1		
AFATL/DLOSL	9		
AFATL/DLJ	1		
AFATL/DLJW	5		
USNWC/Code 326	1		
Naval Wpns Eval Fac/Wpns Dept	1		
Univ of Mich/Dept of Aerospace			
Engineering	10		
Univ of Ill/Dept of Aeronautical			
Engineering	1		
Ohio State Univ/Dept of Aero-			
nautical Sciences	1		

UNCLASSIFIED

SECURITY CLASSIFICATION OF THIS PAGE (When Data Entered)

REPORT DOCUMENTATION PAGE		READ INSTRUCTIONS BEFORE COMPLETING FORM
1. REPORT NUMBER AFATL-TR-76-78	2. GOVT ACCESSION NO.	3. RECIPIENT'S CATALOG NUMBER
4. TITLE (and Subtitle) FUNDAMENTAL ASPECTS OF UNCONFINED EXPLOSIONS: PHASE II		5. TYPE OF REPORT & PERIOD COVERED Final Report: January 1976- May 1976
7. AUTHOR(s) J.A. Nicholls Z. Gabrijel M. Sichel R. Oza		6. PERFORMING ORG. REPORT NUMBER
9. PERFORMING ORGANIZATION NAME AND ADDRESS Department of Aerospace Engineering The University of Michigan Ann Arbor, Michigan 48109		8. CONTRACT OR GRANT NUMBER(s) Contract F08635-74-C-0123
11. CONTROLLING OFFICE NAME AND ADDRESS Air Force Armament Laboratory Armament Development and Test Center Eglin Air Force Base, Florida 32542		10. PROGRAM ELEMENT, PROJECT, TASK AREA & WORK UNIT NUMBERS Project No. 2513 Task No. 07 Work Unit No. 001
14. MONITORING AGENCY NAME & ADDRESS (if different from Controlling Office)		12. REPORT DATE July 1976
		13. NUMBER OF PAGES 102
		15. SECURITY CLASS. (of this report) UNCLASSIFIED
		15a. DECLASSIFICATION/DOWNGRADING SCHEDULE
16. DISTRIBUTION STATEMENT (of this Report) Distribution limited to U.S. Government agencies only; this report documents test and evaluation; distribution limitation applied July 1976. Other requests for this document must be referred to the Air Force Armament Laboratory (DLJW), Eglin Air Force Base, Florida 32542.		
17. DISTRIBUTION STATEMENT (of the abstract entered in Block 20, if different from Report)		
18. SUPPLEMENTARY NOTES Available in DDC.		
19. KEY WORDS (Continue on reverse side if necessary and identify by block number) Unconfined explosions Heterogeneous cylindrical detonations Blast wave initiation Kerosene-air detonation Cylindrical blast waves		
20. ABSTRACT (Continue on reverse side if necessary and identify by block number) This report presents the research conducted in the last phase of this contract (Air Force Contract F08635-74-C-0123). A brief summary of the work conducted under this contract as well as the preceding one (F08635-71-C-0083) is presented in Section I. Appropriate references to project progress reports and external publications are included. In this report, further analytical work on the problem of the blast wave initiation of detonation is described. The problem is attacked in two parts: one is concerned with the chemical kinetic processes behind the blast wave and the		

DD FORM 1473

1 JAN 73

EDITION OF 1 NOV 65 IS OBSOLETE

UNCLASSIFIED

SECURITY CLASSIFICATION OF THIS PAGE (When Data Entered)

UNCLASSIFIED

SECURITY CLASSIFICATION OF THIS PAGE(When Data Entered)

second is the flow field in the expansion zone behind the blast wave. The aim is to patch these solutions together.

On the experimental side, further experimental results on cylindrical blast waves and heterogeneous cylindrical detonations of kerosene drops and air in the sectored shock tube are presented and discussed. These results include a discussion of some operational aspects of the sectored chamber that have some influence on the experimental results. A photographic study of cylindrical blast waves and heterogeneous detonation waves at the immediate exit of the chamber reveal that the waves closely approximate ideal cylindrical waves but that there are an appreciable number of particles ahead of the waves. These particles originated from the blast wave initiating source (blasting cap plus a condensed explosive). Finally, experimental results on the propagation of heterogeneous cylindrical detonation waves through a non-uniform mixture are presented. Varying radial extents of the fuel-air cloud, at two radial positions, were rendered free of fuel by removing the fuel needles from the chamber. The resultant effect on wave propagation is discussed.

UNCLASSIFIED

SECURITY CLASSIFICATION OF THIS PAGE(When Data Entered)